Classical and Extended Crystal-Plasticity and Its Application to Fatigue of FCC Single Crystals

Vladislav Levkovitch

This research project was sponsored and carried out in cooperation with Rolls-Royce Deutschland (RRD). The sponsoring and cooperation is gratefully acknowledged.

The commission:

Prof. K. Thermann, chairman
Prof. B. Svendsen, supervisor
Dr. R. Sievert, supervisor
Prof. S. Forest (Ecole Nationale Superieure des Mines de Paris)
Prof. M.G.D. Geers (University of Eindhofen)

ISBN 3-00-018130-X

Classical and Extended Crystal-Plasticity and Its Application to Fatigue of FCC Single Crystals

Von der Fakultät Maschinenbau
der Universität Dortmund
zur Erlangung des Grades eines
Doktor-Ingenieurs
(Dr.-Ing.)
genehmigte Dissertation

von

Vladislav Levkovitch

Tag der mündlichen Prüfung:
30. September 2005

Dortmund 2005

Summary

The first part of this work deals with the formulation of a three-dimensional crystallographic lifetime rule for face-centered cubic (fcc) single crystals. The damage contribution rate of each slip system to the total damage is governed by the current values of the resolved shear stress and the slip rate on the corresponding slip system. The damage rule is combined with a modified version of the crystallographic viscoplastic deformation model of Cailletaud (Meric *et al.*, 1991). For the nickel-base single crystal superalloy CMSX4 at 950 °C, various strain- and stress-controlled uniaxial cyclic tests with and without hold-times can be described for different crystal orientations by one set of material parameters. For verification, simulation results for a single crystal specimen with a notch have been compared with corresponding experimental results. The predicted lifetime is within the factor of two of the measured one.

Non-homogeneous slip deformation in the direction of slip is accommodated in the material by the development of excess dislocations of the same sign, the so-called geometrically-necessary dislocations (GNDs) (Ashby, 1970). The purpose of the second part is the formulation of a non-local extension of standard crystal plasticity accounting for the effects of GNDs on the material behaviour. To this end, following Nye and many others, local deformation incompatibility in the material is adopted as a measure of the density of GNDs. Their development is assumed to contribute to the energy being stored in the material, resulting in additional kinematic-like hardening effects. A thermodynamic formulation of the model in the context of the dissipation principle facilitates the derivation of the corresponding hardening relation.

In the third part, the effect of such additional hardening on the formation of glide and kink bands at a crack tip in face-centered cubic (fcc) single crystals as well as on the crack tip opening is examined. The results show that this additional hardening retards kink-band formation, but has no influence on glide-band development. It also influences the crack tip opening displacement (CTOD). It turns out that the simulated CTOD correlates well with experimentally determined crack propagation rates for different crack growth directions in the crystal.

In the last part, the resolution of the deformation at the crack tip is refined compared to the mesoscopic analysis of the preceding section. The spatial crack propagation in a polycrystal as well as in a fcc single crystal under cyclic loading is simulated by progressive large deformations at the crack tip due to plastic blunting and re-sharpening after load reversal. Using repeated remeshing for severely distorted elements at the advancing crack tip, deformation patterns in the sense of Laird's mechanism (Laird and Smith, 1962) for fatigue crack propagation with striation formation were obtained in the case of the polycrystal simulation as well as in the case of the single crystal simulation for [110] crack growth direction. The simulation for [100] crack growth direction with the same stress level as for [110] direction also yielded crack extension by progressive large deformations but without striation formation. The dependence of the fatigue striation formation on the crack growth direction as predicted by the simulation of crack propagation in single crystals is verified by the experimental results of Neumann (1974) on pure copper single crystals.

Überblick

Der erste Teil dieser Arbeit beschäftigt sich mit der Formulierung einer dreidimensionalen kristallographischen Lebensdauerregel für flächenkubischzentrierte Einkristalle. Die Rate des Schädigungsbeitrages jedes Gleitsystems zur Gesamtschädigung wird kontrolliert durch die momentanen Werte der Schmidt Spannung und der Gleitrate auf dem entsprechenden Gleitsystem. Die Lebensdauergleichung ist kombiniert mit einer modifizierten Version des kristallographischen viskoplastischen Deformationsmodels von Cailletaud. (Meric *et al.* , 1991). Für die Nickelbasissuperlegierung CMSX4 ist es gelungen mit einem einzigen Parametersatz diverse verschiebungs- und kraftkontrollierte eindimensionale unterschiedlich orientierte zyklische Versuche ohne und mit Haltezeiten zu beschreiben. Zwecks der Verifizierung des Modells wurde die Lebensdauer einer einkristallinen gelochten Probe simuliert. Der Vergleich mit dem Experiment zeigt, dass die vorhergesagte Lebensdauer innerhalb des Faktors von Zwei liegt.

Nichthomogene plastische Deformation mit dem Gradienten in die Gleitrichtung werden im Material durch Überschussversetzungen gleichen Vorzeichens, sogenannte geometrisch notwendige Versetzungen (GNV) realisiert (Ashby, 1970). Das Ziel des zweiten Teils dieser Arbeit ist eine nichtlokale Erweiterung der Standardkristallplastizität, die den Einfluss der GNV auf das Materialverhalten berücksichtigt. In Anlehnung an Nye und viele andere Autoren wird die lokale Deformationsinkompatibilität als Maßfür die Dichte der GNV eingeführt. Es wird angenommen, dass die Entwicklung der GNV zur Energiespeicherung beiträgt. Das Ergebnis der Auswertung des Dissipationsprinzips unter Berücksichtigung der zusätzlichen Energiespeicherung ist dann eine zusätzliche Verfestigung kinematischer Natur.

Im dritten Teil untersuchen wir den Einfluss dieser zusätzlichen kinematischen Verfestigung auf die Entwicklung von Gleit- und Knickbändern an der Rissspitze in einem flächenkubischzentrierten Einkristall. Die Simulationsergebnisse zeigen, dass die zusätzliche Verfestigung infolge nichthomogener plastischer Deformationen zur Abschwächung der Intensität der Knickbänder führt, aber die Gleitbänder nicht beeinflusst. Sie hat ebenfalls Einfluss auf die Rissöffnungsverschiebung. Es stellt sich heraus, dass im Gegensatz zur klassischen Kristallplastizität die simulierten Rissöffnungsverschiebungen ganz gut mit den experimentellen Rissausbreitungsgeschwindigkeiten für verschiede Kristallrichtungen korrelieren.

Im letzten Teil der Arbeit wird die Auflösung an der Rissspitze im Vergleich zur mesoskopischen Betrachtung des vorherigen Kapitels noch mehr verfeinert. Die räumliche Rissausbreitung unter zyklischer Belastung in einem Polykristall sowie in einem KFZ Einkristall wird mit Hilfe progressiver großer Deformationen begleitet von der plastischen Abstumpfung und Wiederzuspitzung nach der Belastungsumkehr simuliert. Unter Benutzung der Neuvernetzung für stark verzerrte Elemente an der Rissspitze ist es möglich, die Lairdschen Deformationsmuster (Laird and Smith, 1962) der Ermüdungsrissausbreitung mit Schwinglinien im Falle der polykristallinen und einkristallinen Simulation für [110] Rissausbreitungsrichtung zu erhalten. Die Simulation für [100] Rissausbreitungsrichtung bei gleicher Belastung ergab ebenfalls Risswachstum durch fortschreitende große Deformationen aber ohne Schwinglinien. Die Abhängigkeit der Schwinglinienentwicklung von der Rissorientierung im Falle der einkristallinen Simulation wurde durch den Vergleich mit den Experimenten von Neumann (1974) an Kupfereinkristallen verifiziert.

Contents

1 **Macroscopic fatigue modeling of single crystals** **3**
- 1.1 Introduction . . . 3
- 1.2 Deformation model for single crystals . . . 6
  - 1.2.1 The crystallographic model of Cailletaud . . . 6
  - 1.2.2 Modification of the Cailletaud model . . . 7
  - 1.2.3 Parameter identification for CMSX4 . . . 9
- 1.3 Lifetime assessment . . . 13
  - 1.3.1 Multiaxial fatigue . . . 13
  - 1.3.2 Time-incremental approaches based on the critical plane concept . . . 13
- 1.4 A three-dimensional lifetime rule for single crystals . . . 14
  - 1.4.1 Model formulation . . . 14
  - 1.4.2 Application to CMSX4 . . . 16
- 1.5 Conclusion . . . 18
- 1.6 Acknowledgment . . . 19

2 **Extended deformation modeling of single crystals: effect of geometrically necessary dislocations** **22**
- 2.1 Introduction . . . 22
- 2.2 Large-deformation continuum constitutive setting . . . 26
- 2.3 Finite dislocation density and lattice curvature measures . . . 29
- 2.4 Standard-continuum-based extensions of crystal plasticity . . . 32
- 2.5 Continuum thermodynamic extension of crystal plasticity . . . 34
- 2.6 Comparison with some other extended continuum approaches . . . 40
- 2.7 Discussion . . . 44

3 **Application to crack tip** **49**
- 3.1 Introduction . . . 49
- 3.2 Model formulation . . . 50
- 3.3 Glide- and kink-banding at a crack tip . . . 53
- 3.4 Ductile crack propagation . . . 57
- 3.5 Acknowledgment . . . 60

4 **Microscopic modeling of fatigue crack propagation** **62**
- 4.1 Introduction . . . 62
- 4.2 Models for crack propagation via striation formation . . . 64

4.3 Material modeling and finite element implementation 67
4.4 Simulation results 70
4.5 Conclusion 73

Chapter 1

Macroscopic fatigue modeling of single crystals*

Abstract– This work deals with the formulation of a three-dimensional crystallographic time-incremental lifetime rule for face-centered cubic (fcc) single crystals used for gas turbine blade applications. The damage contribution rate of each slip system to the total damage is governed by the current values of the resolved shear stress and the slip rate on the corresponding slip system. The damage rule is combined with a crystallographic viscoplastic deformation model. For the nickel-base single crystal superalloy CMSX4 at 950 °C, various strain- and stress-controlled uniaxial cyclic tests with and without hold-times can be described for different crystal orientations by one set of material parameters. For verification, simulation results for a single crystal specimen with a notch have been compared with corresponding experimental results. The predicted lifetime is within the factor of two of the measured one.

1.1 Introduction

In the report entitled *General Principles for Fatigue Testing of Metals*, which was published in 1964 in Geneva, fatigue of materials is defined as a term which ”applies to changes in properties which can occur in a metallic material due to the repeated application of stresses or strains, although usually this term applies specially to those changes which lead to cracking or failure”. This description is also generally valid for the fatigue of nonmetallic materials. The fatigue failure is generally caused by cyclic loads whose peak values are considerably smaller then the corresponding static failure loads.

There are also different stages of fatigue damage evolution in a structural component where defects may initiate in an initially defect-free region and propagate in a stable manner before catastrophic fracture occurs. This is the most general situation. In such a case, the evolution of fatigue damage can be broadly classified into the following stages (Suresh, 1998): substructural and microstructural changes which cause the initiation of permanent damage; the creation of small cracks; the growth and coalescence of small flaws to form a ”dominant” crack, which may eventually lead to catastrophic failure; stable propagation of the macro-crack; structural instability or complete fracture.

The conditions for the initiation of microdefects and the rate of the dominant fatigue crack propagation are strongly influenced by a wide range of mechanical, microstructural and environmental factors. The principal differences among different design philosophies often rest on how the crack initiation and propagation stages of fatigue are quantitatively treated.

Material scientists concerned with the microscopic mechanisms of fatigue regard the initiation of micrometer-size flaws along slip bands and grain boundaries and the roughening of fatigued surfaces as the crack initiation stage of fatigue failure. A practical engineer, on the

---

[*] accepted 2006 in *International Journal of Fatigue* under the title:
”Simulation of deformation and lifetime behavior of a fcc single crystal superalloy at high temperature under low-cycle fatigue loading”.

other hand, relates the limit of resolution of the (nondestructive) crack detection equipment (typically a fraction of millimeter) with the initiation of a fatigue macro-crack and with the initial crack size used for design. Scattered within the limits of this broad range of choices, there lies a variety of definitions for crack initiation, which are specific to certain classes of fatigue-critical engineering applications. The total fatigue lifetime is defined as a sum of the number of cycles to initiate a fatigue crack and the number of cycles to propagate it subcritically to some final crack size. Thus, it is very important to make a clear demarcation between crack initiation and propagation stages.

In the ”defect-tolerant approach”, it is assumed that all engineering structures are inherently flawed. The size of a pre-existing flaw is generally determined by nondestructive testing methods. In that case, fatigue life is defined as the number of fatigue cycles needed for the crack to reach its critical size. On the other hand, in the ”total-lifetime approach”, it is assumed that a specimen is initially uncracked and that the major part of the fatigue process is spent in the initiation of a macrocrack. Classical ”total-lifetime approach” methods (also called algebraic lifetime rules) describe the fatigue time to failure in terms of a single cyclic parameter such as the cyclic stress (Basquin, 1910) or strain range (Coffin, 1954; Manson, 1954). The stress based life analysis is appropriate in the case of elastic and unconstrained deformation. At highly stressed regions near a notch, plastic deformation is controlled by the surrounding elastic neighborhood. Thus, a strain-controlled test is a good approximation of the conditions experienced by the material at locations of stress concentrations and a strain-based life approach seems to be more appropriate in such situations.

The stress- (Basquin, 1910) or strain-based criteria (Coffin, 1954; Manson, 1954) do not account for a possible interaction between the stress and strain in a deformation process. Therefore they cannot reflect the path dependence of the material response. An appropriate measure which considers both, the stress and the strain, would be the plastic work performed per cycle (Ellyn and Kujawski, 1986).

Various techniques are available to account for the effects of mean stress, stress concentration, environment, multiaxial stress states and variable amplitude stress fluctuations on the fatigue process using these classical approaches (see *e.g.*, Li and Smith, 1995; MacLachlan and Knowles, 2001; Chaboche and Gallerneau, 2001). Since such approaches rely on the cycle concept they can be applied only under loading conditions, where the stress or the strain range are given. However, due to complex shapes of real structural components, thermomechanical processes taking place inside such a component can lead to very complex multiaxial local loading (Cailletaud *et al.*, 2003). In order to apply a lifetime rule a local deformation analysis has to be conducted first. For viscoplastic materials this entails the usage of a history-dependent constitutive model. Under such circumstances, a much better choice is offered by an incremental lifetime rule, in which the total damage is evaluated in each time increment and thus, being governed by an evolution relation (Majumdar and Maiya, 1980; Satoh and Krempl, 1982). Due to their time-incremental nature, such lifetime rules can be applied also to complex multiaxial loading paths, for which the definition of a single loading parameter describing the entire cycle could be difficult. Instead, time-incremental lifetime rules can simply be integrated along with the other evolution relations. In the case of periodic loading, one saturated cycle needs to be considered, as in the case of algebraic laws. Since an incremental lifetime rule is coupled with a constitutive model for the cyclic deformation behavior, it can be represented in terms of the current stress-strain behavior of the material, in contrast to classical models, and thus, be used to investigate the connection between stress state and fatigue (Yeh and Krempl, 1993; Sermage *et al.*, 2000).

The generalization from uniaxial to multiaxial fatigue implies the use of suitably-defined equivalent measures of the three-dimensional stress and strain states instead of their uniaxial counterparts. Such quantities, which influence the fatigue process, include the maximum shear strain range and the strain range in the direction perpendicular to the plane of the maximum shear strain range. These were introduced by Brown and Miller (1973) due to the fact that fatigue crack initiation and early growth take place along activated crystallographic slip planes and are as such shear-controlled processes.

The goal of the present work is to describe the low-cycle fatigue failure of the single-crystal superalloy CMSX4 under complex loading at elevated temperatures. CMSX4 is used, for example, in the manufacturing of turbine blades (Bullough *et al.*, 1998; Arakere and Orozco, 2001). Due to the complex geometry and operating conditions for such blades, the material undergoes a complex loading history during the lifetime of a blade. A reliable lifetime analysis should account for the complex deformation processes taking place in the material. Thus, both the material model and the lifetime rule should be formulated in a time incremental fashion. The additional difficulty arising in the context of using single crystals is the strong orientation dependency of the deformation and fatigue damage behavior.

As a basis for the material modeling, we use the crystallographic model of Cailletaud (*e.g.*, Meric *et al.*, 1991) which applies the one-dimensional form of the standard viscoplastic Chaboche model for isotropic and kinematic hardening to each slip system. Here, this model is slightly modified to account for the ”fast” softening effect observed in tensile tests for different directions.

In this context, next we develop a three-dimensional anisotropic time-incremental lifetime rule on the basis of the approach of Satoh and Krempl (1982), adapted in the same way as the Cailletaud model to the current case. To this end, instead of working with the concept of the maximum plastic shear as done by Yeh and Krempl (1993), we use the crystallographic slips. These are much more natural in the case of single crystals and represent in any given case the quantities controlling fatigue crack initiation and early growth. Consequently, the damage evolution in our model is driven by the resolved shear stress in combination with the inelastic strain-rate on each slip system. At the same time, the use of the crystallographic slips allows us to capture the orientation-dependence of the fatigue failure, just as a crystallographic deformation model enables us to describe an anisotropic stress-strain response of a single crystal.

As originally introduced by Majumdar and Maiya (1980), the proposed lifetime rule corresponds directly to a crack propagation law. It is assumed here, that crack initiation occurs early in life at an already initially present defect, as, *e.g.*, a casting pore (Miller *et al.*, 2004). The influence of the position of the crack relative to the crystal (secondary orientation) on the crack growth behavior was considered by Henderson and Martin (1996), Miller *et al.* (2004) and Levkovitch *et al.* (2005).

At high temperature also oxidation is important. The influence of oxidation on the lifetime can be taken into account indirectly by the accumulation of damage with time (see the comparison of the time-incremental lifetime rule of Danzer (1987) with the oxidation rule of Reuchet and Remy (1983)). The time needed to oxidize and finally break a volume element ahead of a crack tip represents a strongly time-dependent damage process (Rezai-Aria and Remy, 1989; Remy, 2001).

1.2 Deformation model for single crystals

1.2.1 *The crystallographic model of Cailletaud*

Crystallographic models use the fact that in single crystals the inelastic deformation results from slip processes due to the dislocation motion on a given set of crystallographic planes. In this case, the inelastic strain rate $\dot{\boldsymbol{\varepsilon}}_{\mathrm{p}}$ is expressed as the sum

$$\dot{\boldsymbol{\varepsilon}}_{\mathrm{p}} = \frac{1}{2} \sum \dot{\gamma}_\alpha \left(\boldsymbol{n}_\alpha \otimes \boldsymbol{s}_\alpha + \boldsymbol{s}_\alpha \otimes \boldsymbol{n}_\alpha \right) \tag{1.1}$$

over the inelastic shear strain rates $\dot{\gamma}_\alpha$ on all slip systems. Here, $\boldsymbol{s}_\alpha$ denotes the slip direction and $\boldsymbol{n}_\alpha$ the slip-plane normal. With the decomposition

$$\boldsymbol{\varepsilon} = \boldsymbol{\varepsilon}_{\mathrm{e}} + \boldsymbol{\varepsilon}_{\mathrm{p}} \tag{1.2}$$

of the total strain into elastic and inelastic parts, the stress tensor $\boldsymbol{\sigma}$ is determined by the linear relation

$$\boldsymbol{\sigma} = \boldsymbol{\mathcal{C}}\, \boldsymbol{\varepsilon}_{\mathrm{e}} \tag{1.3}$$

where $\boldsymbol{\mathcal{C}}$ represents the fourth-order elasticity tensor. In the case of cubic symmetry, $\boldsymbol{\mathcal{C}}$ is given by three independent constants $\mathcal{C}_{1111}$, $\mathcal{C}_{1122}$ and $\mathcal{C}_{1212}$.

Now, we consider the crystal plasticity model of Cailletaud (*e.g.*, Meric *et al.*, 1991). The model assumes a face-centered cubic (fcc) symmetry and accounts for 12 octahedral slip systems of type $\{111\}(110)$ and 6 cubic slip systems of type $\{100\}(011)$. The 12 octahedral slip systems define the octahedral slip family and the 6 cubic slip systems the cubic slip family. The constitutive relations of each family are of the same form with the material parameters taking distinct values. The Cailletaud model is actually the one-dimensional form of the isotropic Chaboche model (Chaboche, 1977) on each slip system. So, the viscoplastic flow rule

$$\dot{\gamma}_\alpha = \left\langle \frac{|\tau_\alpha - x_\alpha| - (r_\alpha + r_0)}{k} \right\rangle^n \operatorname{sign}\left(\tau_\alpha - x_\alpha\right) \tag{1.4}$$

determines the inelastic shear strain-rate $\dot{\gamma}_\alpha$ on the slip system α as a function of the resolved shear stress $\tau_\alpha = \boldsymbol{\sigma} \cdot (\boldsymbol{s}_\alpha \otimes \boldsymbol{n}_\alpha)$, the back stress x_α, and the isotropic self-hardening contribution r_α to the yield stress, all on the same slip-system. In particular, the power-law form involves the strain-rate exponent n representing an additional dynamic contribution to hardening here. The evolution of kinematic hardening x_α accounts for growth as well as dynamic and static recovery in the standard form

$$\dot{x}_\alpha = c\left\{a\Phi(\nu_\alpha)\dot{\gamma}_\alpha - x_\alpha|\dot{\gamma}_\alpha|\right\} - d\left|\frac{x_\alpha}{a}\right|^m \operatorname{sign}\left(x_\alpha\right) \quad , \tag{1.5}$$

where

$$\Phi(\nu_\alpha) = \Phi_{\mathrm{s}} + (1 - \Phi_{\mathrm{s}})e^{-\omega\nu_\alpha} \tag{1.6}$$

is a function of the accumulated plastic slip ν_α with $\dot{\nu}_\alpha = |\dot{\gamma}_\alpha|$. While static recovery allows the simulation of stationary creep, the function $\Phi(\nu_\alpha)$ takes the change of the saturation value a regarding the kinematic hardening with advancing inelastic deformation into account. Lastly, the evolution of r_α is given by the equation

$$\dot{r}_\alpha = b(Q - r_\alpha)\dot{\nu}_\alpha \quad . \tag{1.7}$$

Isotropic self-hardening allows the modeling of phenomena such as the increase of the stress amplitude during a displacement controlled cyclic test with a constant strain amplitude (cyclic hardening).

1.2.2 Modification of the Cailletaud model

Studying the deformation behavior of the fcc single crystal superalloy CMSX4 at 950 °C on the basis of uniaxial tensile tests with different strain rates for three orientations $\langle 100\rangle$, $\langle 111\rangle$ and $\langle 110\rangle$ (Figure 1.1)[1], a rarely observed effect of rapid softening behavior is revealed (compare, *e.g.*, Busso *et al.*, 2000). The tensile curves for all three orientations show a drop in the flow stress shortly after the beginning of yielding. Furthermore, this softening behavior is rate-dependent, since the magnitude of the stress drop decreases for the tests with lower strain rates.

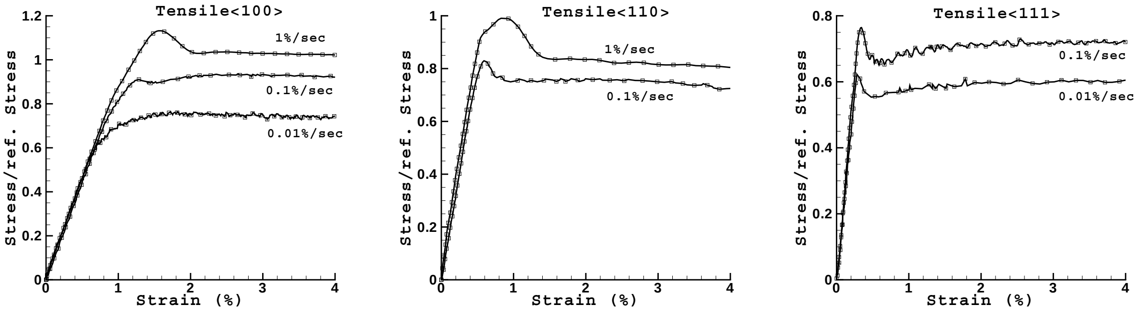

Figure 1.1: Tensile tests in different orientations

Using the Cailletaud model a rapid softening behavior can be described only by the variable r_α which is responsible for the change of the initial flow stress r_0 on the slip system α. However, if we solve the flow rule (1.4) with respect to the resolved shear stress

$$\tau_\alpha = x_\alpha + \operatorname{sign}(\dot\gamma_\alpha)\left(r_0 + r_\alpha + k\,|\dot\gamma_\alpha|^{1/n}\right) \tag{1.8}$$

it becomes obvious that a negative r_α leads to a softening which is independent of the strain rate. Since the Cailletaud model is deduced from the Chaboche model, we can use the version in which the isotropic hardening doesn't act on the yield stress but on the viscosity constant k

$$\dot\gamma_\alpha = \left\langle \frac{|\tau_\alpha - x_\alpha| - r_0}{k + r_\alpha} \right\rangle^n \operatorname{sign}(\tau_\alpha - x_\alpha) \quad , \tag{1.9}$$

whereby the Schmid stress is expressed now as

$$\tau_\alpha = x_\alpha + \operatorname{sign}(\dot\gamma_\alpha)\left[r_0 + (k + r_\alpha)\,|\dot\gamma_\alpha|^{1/n}\right] \quad . \tag{1.10}$$

In this case, the yield stress and the inelastic shear strain rate appear as the product $r_\alpha\,|\dot\gamma_\alpha|^{1/n}$ and allow the simulation of rate-dependent softening for negative values of r_α. Integrating the equation (1.7) the variable r_α can be expressed as a function of the accumulated plastic strain ν_α

$$r_\alpha(\nu_\alpha) = Q\left(1 - e^{-b\nu_\alpha}\right) \quad . \tag{1.11}$$

Using this equation and by denoting the expression $(|\tau_\alpha - x_\alpha| - r_0)$ as effective stress τ_{eff}, the modified flow rule (1.9) for monotonic processes can be written as

$$\dot\gamma_\alpha = \tau_{\text{eff}}^n\,[k + r_\alpha(\nu_\alpha)]^{-n} \quad . \tag{1.12}$$

---

[1] This work was a direct cooperation with Rolls-Royce Germany. Because of this industrial dependence, the loading values of the test and the determined material parameter values are unfortunately not allowed to be given.

In this form the flow rule represents a particular form of the more general Orowan equation

$$\dot{\gamma} = v(\tau_{\text{eff}})\rho(\nu)b \quad . \tag{1.13}$$

In this case, b represents the burger's vector, v the velocity of the dislocation motion as a function of the effective stress and ρ the density of mobile dislocation as a function of the cumulated plastic slip. On the one hand, we have seen that negative values of r_α can describe the rapid rate dependent softening effect observed in the experiments. On the other hand, comparing the equations (1.12) and (1.13), we identify negative changes of r_α as an increase in the number of mobile dislocations on the slip system α. Thus, within this theory such rapid, rate dependent softening behavior can be explained by dislocation multiplication on the slip systems, where the plastic deformation takes place. This statement leads to a direct consequence for the interaction between the octahedral and cubic slip families if one takes into account the fact that the cubic slip used in the Cailletaud model is actually macroscopic. That means that from the microscopical point of view the cubic slip does not originate from dislocation movement on cubic planes but from zigzag cross slip of screw dislocations on octahedral planes in the matrix channels which then leads to a macroscopic cubic slip, the so-called cube slip (Bettge and Österle, 1999). Therefore now we use the word ”cube” instead of ”cubic” throughout the work. Thus, for example, the slip process on the cube system $(100)[011]$ is actually a zigzag slip of screw dislocations with the Burger's vector $[011]$ on the octahedral systems $(1\bar{1}1)[011]$ and $(11\bar{1})[011]$. Now we recall that the rapid softening behavior observed in tensile tests was interpreted as a formation of new mobile dislocations. But the creation of new mobile dislocations due to the octahedral slip leads to a higher number of mobile screw dislocations capable to cross slip. That facilitates the cube slip on the corresponding systems and, thus, results in a softening of those cube slip systems. On the same account a softening on a cube slip system leads to a softening on both corresponding octahedral systems and we obtain the effect of cross softening between a cube slip system and two octahedral slip systems, whereby all three systems have the same slip direction. In the case of fcc single crystals there are six of such triple sets with the same slip direction.

Now we try to develop the constitutive equations for the above mentioned effect of cross softening. In the Cailletaud model the interaction between slip system is introduced at the level of isotropic hardening. To understand how it works we investigate two slip systems interacting with each other, denoted here by 1 and 2. First, we consider the influence of the system 1 on the system 2. The additive contribution $q_{1\to2}$ of the slip system 1 to the total hardening on the system 2 is given by the self hardening r_1 on the system 1 multiplied by the interaction parameter h_{12}

$$q_{1\to2} = h_{12} r_1 \tag{1.14}$$

with

$$\dot{r}_1 = b_1(Q_1 - r_1)\dot{\nu}_1 \quad . \tag{1.15}$$

In the case of the rapid softening behavior, however, like for CMSX4, such description of the interaction leads to the problem that for orientations, where the slip system 1 compared to 2 is much less active, the self hardening on the system 2 rapidly reaches its saturation value Q_2, while the system 1 provides a softening contribution long after that and results in further stress decrease, which contradicts the test results. This can be avoided by the assumption that after the saturation of the self hardening q_2 no softening contribution comes from the system 1. It can be achieved by using a new internal variable $r_{1\to2}$ instead of the self hardening r_1 with the evolution equation

$$\dot{r}_{1\to2} = b_2(Q_2 - r_{1\to2})\dot{\nu}_1[(Q_2 - r_2)/Q_2] \quad . \tag{1.16}$$

This variable has the desired property to vanish when the self hardening on the system 2 reaches the saturation value $(Q_2 = r_2)$. At this point the contribution $q_{1\to2}$ of the slip system 1 to the total hardening on the system 2 is given by the product of the variable $r_{1\to2}$ with the interaction parameter h_{12}

$$q_{1\to2} = h_{12} r_{1\to2} \tag{1.17}$$

As mentioned above we postulate the interaction between one cube and two octahedral slip systems so that all three have the same slip direction but different slip planes. In this case the model has two additional parameters. One controls the influence of the octahedral slip system on the corresponding cube one and the other the influence of the cube on the both corresponding octahedrals. To verify these assumptions we have to consider tests in directions, for which both slip families show an approximately equally strong slip activity. Due to comparable Schmid factors $\langle 011 \rangle$ is such a direction.

1.2.3 Parameter identification for CMSX4

The identification of the material parameters is usually performed on $\langle 001 \rangle$ and $\langle 111 \rangle$ oriented tests. Since these orientations produce a pure octahedral and predominantly cube slip, respectively, the determination of the parameters can be carried out for each slip family separately.

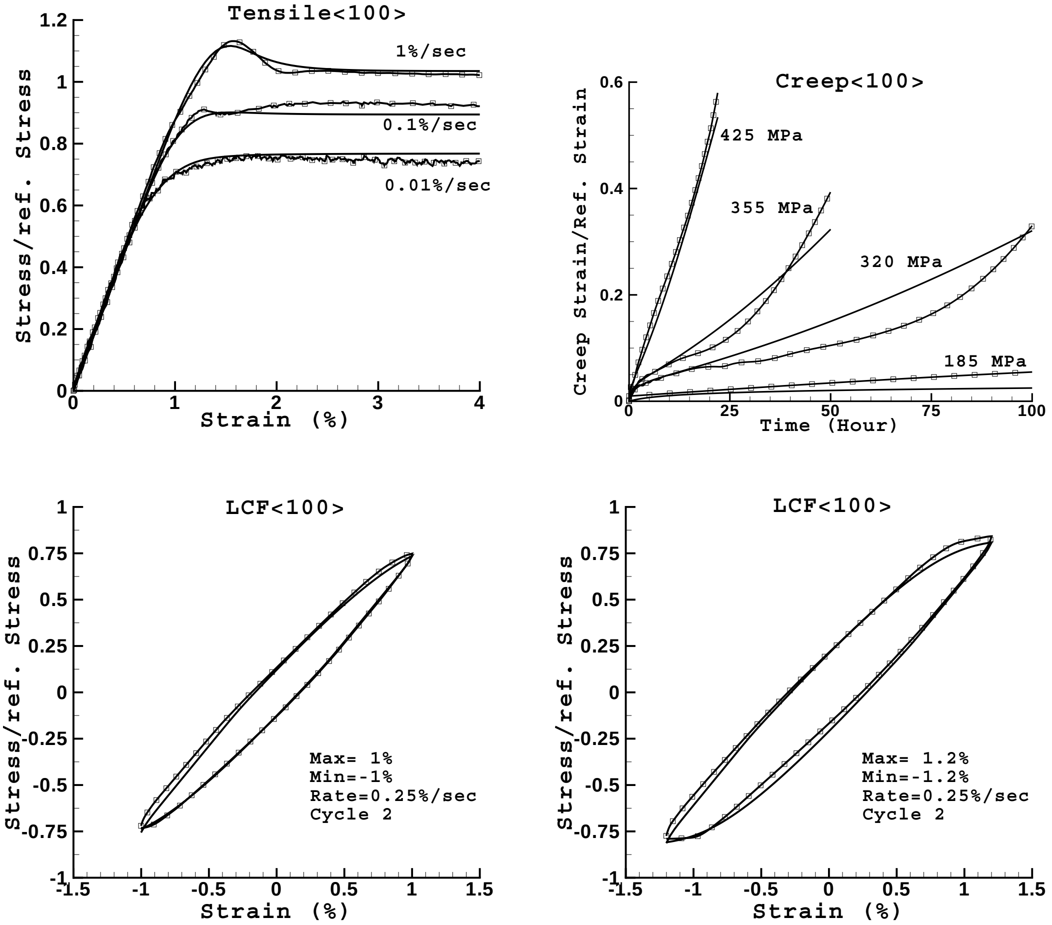

Figure 1.2: Simulation of $\langle 001 \rangle$ oriented tests

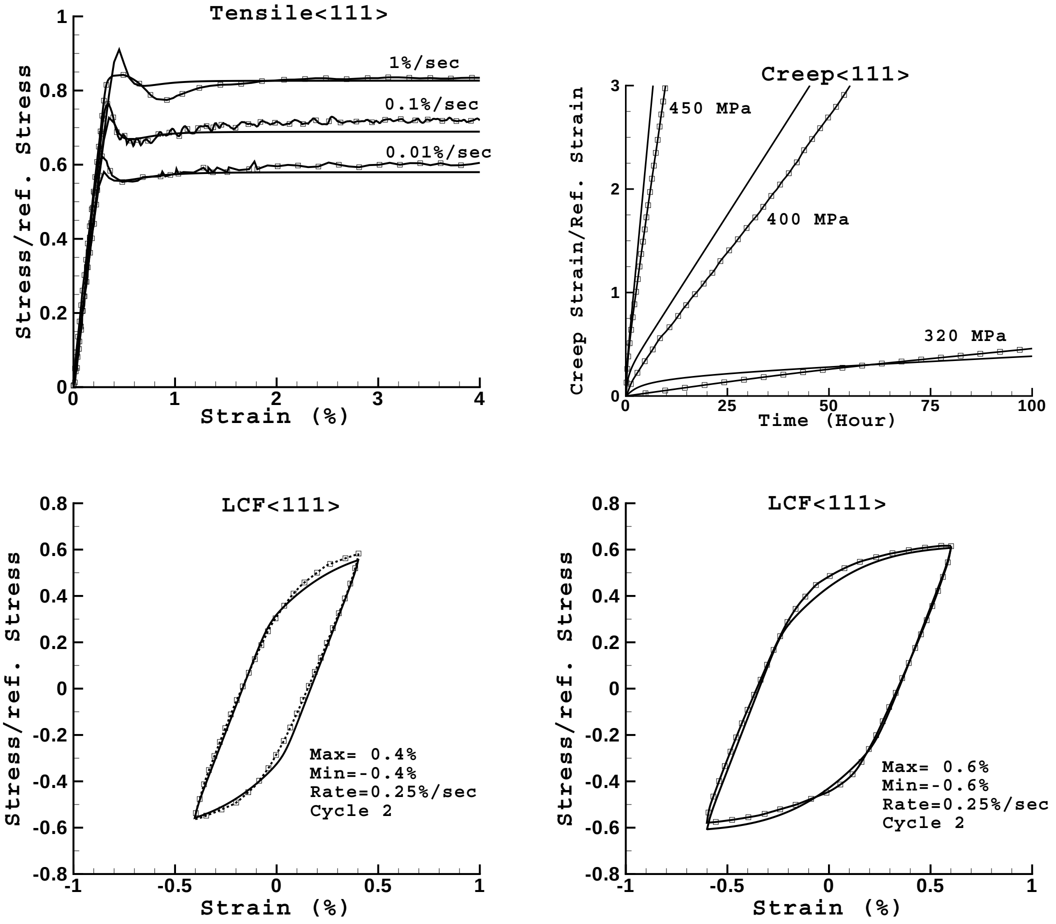

Figure 1.3: Simulation of $\langle 111 \rangle$ oriented tests

The viscosity parameters $(k,\, n)$, the hardening parameters $(a,\, c,\, \Phi_\infty,\, \omega,\, r_0,\, Q,\, b)$, and static

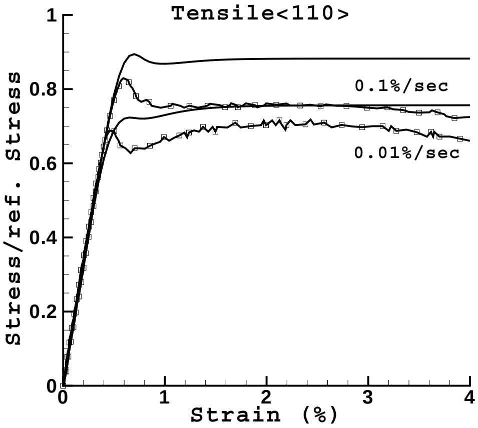

Figure 1.4: Simulation of $\langle 011 \rangle$ oriented tensile tests without slip system interaction

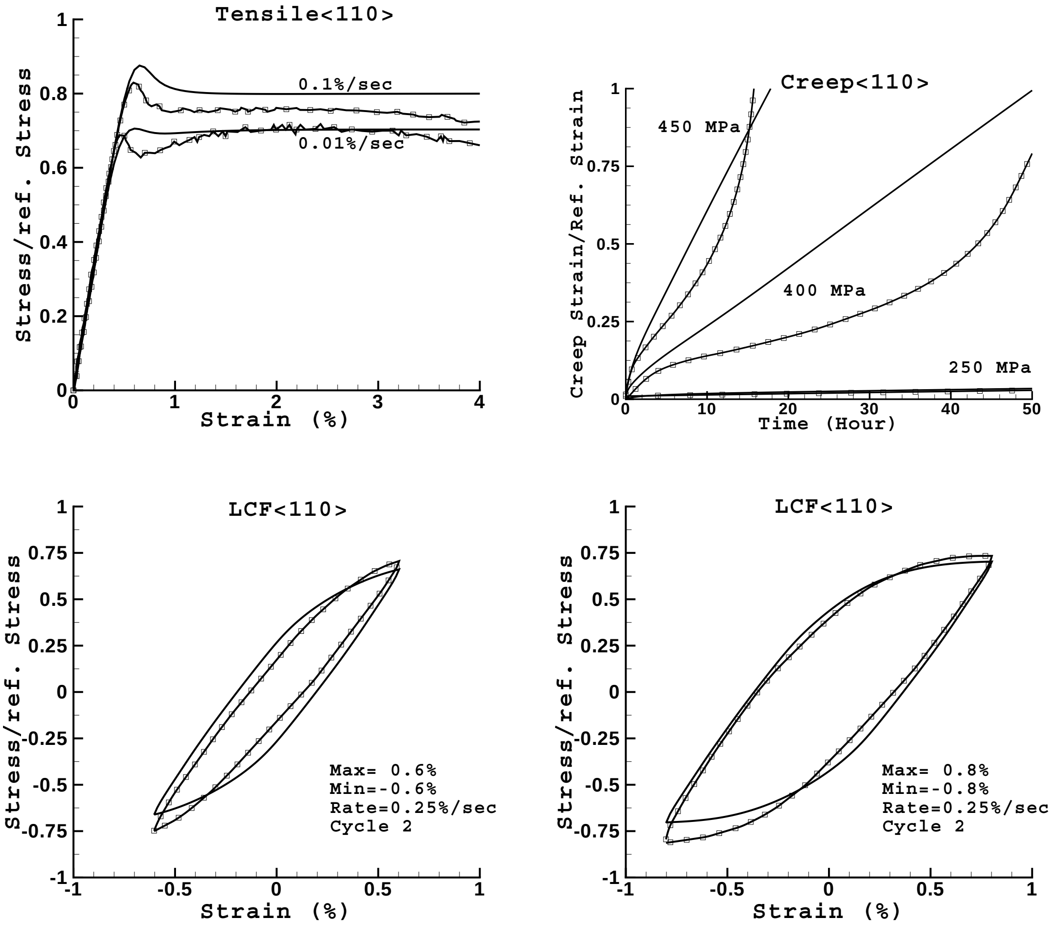

Figure 1.5: Simulation of $\langle 011 \rangle$ oriented tests

recovery parameters $(d,\, m)$ are obtained by the classical optimization technique using uniaxial tensile, cyclic and creep tests in the $\langle 001 \rangle$ and $\langle 111 \rangle$ directions. Once separated, the parameters of both slip families can be identified in the same manner as in the case of the isotropic Chaboche model (Nouailhas, 1989). The results of the fitting procedure are shown in Figures 1.2 and 1.3. Particularly in the case of the $\langle 001 \rangle$ tensile tests, the rapid rate dependent softening behavior could be simulated very well by assuming that the hardening variable q_α acts on the viscosity instead of on the flow stress (1.9). Furthermore, it is worth noting that with only one kinematic hardening variable per slip system both the tensile tests and the hysteresis shape in the cyclic tests could be described. And the usage of the static recovery concept allowed an acceptable fitting of the creep tests over a wide stress range.

However, to study the interaction between the octahedral and cube slip families we need to consider an orientation other then $\langle 001 \rangle$ and $\langle 111 \rangle$, since for these directions only one slip family is active in each case. Due to the equally strong slip activity on slip systems of both families, the orientation most frequently used for this purpose is $\langle 011 \rangle$. Now we try to simulate tensile tests in this direction, first by assuming no interaction and using the material constants fitted to the $\langle 001 \rangle$ and $\langle 111 \rangle$ oriented experiments. While for both these orientations the tensile tests could be described very well (Figures 1.2 and 1.3), the stresses for the tensile tests in the $\langle 011 \rangle$ direction are overestimated significantly if no interaction is used (Figure 1.4).

In contrast, using the constitutive equations (1.16) and (1.17) and fitting both interaction parameters to the tensile and LCF tests in the $\langle 011 \rangle$ direction the simulation can be improved significantly (Figure 1.5).

While for the parameter fitting the most simple tests are used in order to separate different deformation mechanisms and, thus, to facilitate the optimization procedure (Nouailhas, 1989; Sievert *et al.* , 1997), tests with complex loading history are used to verify the capabilities of the chosen model and the quality of the fitted parameter values. So called creep-fatigue interaction tests (cyclic tests with hold-times at the load reversals) belong to the standard tests used in the case of viscoplastic material behavior. In our case we used a strain-controlled nonsymmetric ($R = 0$) cyclic test with 120 sec hold-time at the point of the maximum strain and a stress-controlled nonsymmetric ($R = 0$) cyclic test with 100 sec hold-time at the point of maximum stress, both in the $\langle 100 \rangle$ direction. As one can see in Figure 1.6 a good agreement with the experiment could be achieved in both the strain- and stress-controlled tests.

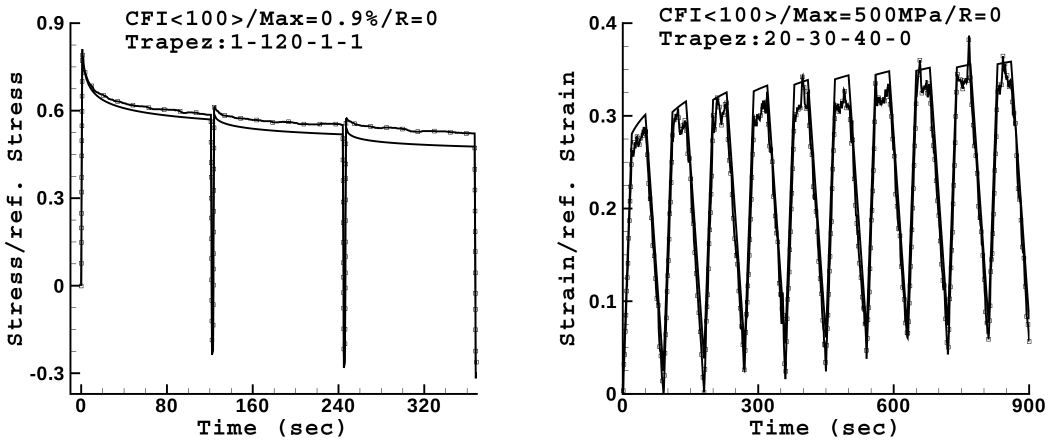

Figure 1.6: Simulation of creep-fatigue-interaction tests; left: strain controlled, right: load controlled

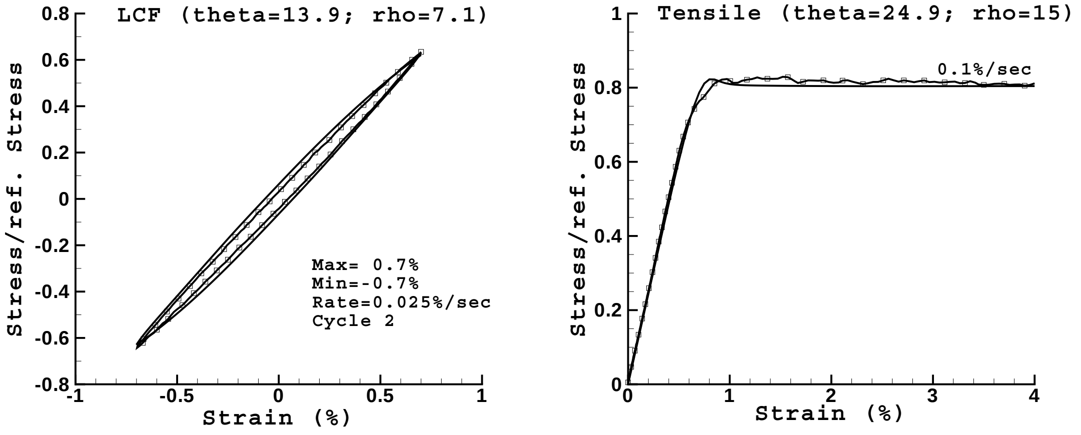

Figure 1.7: Simulation of randomly oriented tests

Furthermore, in the case of an anisotropic model, it is essential to verify how the model can predict other directions than those used for the parameter optimization. Simulation results of a randomly oriented tensile test and a randomly oriented LCF test (Figure 1.7) demonstrate in an impressive way the capability of the Cailletaud model to describe the orientation dependency of the material behavior.

1.3 Lifetime assessment

1.3.1 Multiaxial fatigue

Multiaxial stress states are encountered in the majority of structural components. The motivation for multiaxial fatigue investigations has been to produce design guidelines. To generalize from uniaxial to multiaxial fatigue where multiaxial data do not exist, most designers use the octahedral shear strain

$$\gamma_{\text{oct}} = \frac{2}{3}\sqrt{(\varepsilon_1 - \varepsilon_2)^2 + (\varepsilon_2 - \varepsilon_3)^2 + (\varepsilon_3 - \varepsilon_2)^2} \quad , \tag{1.18}$$

where ε_1, ε_2 and ε_3 are the principal strain components as the effective quantity controlling the life in low cycle fatigue. However, with the increasing amount of biaxial fatigue data it becomes apparent that a single load parameter, such as the octahedral shear strain, cannot correlate uniaxial with multiaxial fatigue under complex multiaxial loading. So, Blas and Zamrik (1976) and Kanazawa *et al.* (1977) plotted the octahedral shear strain range against fatigue lives of Type 304 stainless steel and 1Cr-Mo-V steel, respectively, under a variety of axial-torsional loadings to show that on such a plot the fatigue data do not collapse onto a single curve, thus proving that the octahedral shear strain alone cannot correlate fatigue data generated under various biaxial loadings for these two materials. It thus appears that at a minimum two loading parameters will be necessary to uniquely correlate biaxial fatigue data.

Since fatigue crack initiation and early growth take place along activated crystallographic slip planes, these two processes are shear-controlled. Based on this, Brown and Miller (1973) have suggested the use of the maximum shear strain range and the strain range in the direction perpendicular to the plane of the maximum shear strain range as the two parameters controlling the fatigue life. Accordingly in this approach, the crack is assumed to initiate and then to propagate along the plane of the maximum plastic shear strain range intersecting the surface specimen.

1.3.2 Time-incremental approaches based on the critical plane concept

Since the algebraic approaches use mean values over a cycle, such as strain or stress ranges, they can only be applied in conjunction with the concept of a cycle. In contrast, time-incremental approaches use a damage variable which is described by an evolution equation that prescribes the damage evolution rate as a function of current values of stress, strain, and strain rate. These approaches can be applied to any complex loading history. Failure is said to occur when the damage variable reaches a predefined critical value. The damage variable D is considered as a lifetime consumption variable that does not influence the deformation behavior of the material.

Majumdar and Maiya (1980) have proposed an uniaxial incremental lifetime rule in which fatigue damage is measured by the current crack length a. It is assumed that a crack of an initial length a_0 is initiated early in the life. The rate of crack growth is controlled by the current values of plastic strain and plastic strain rate. Using the idea of Brown and Miller, Majumdar (1981) has extended the uniaxial rule of Majumdar and Maiya (1980) to the case of multiaxial fatigue.

In the absence of cavities, the uniaxial version of the fatigue life rule can be generalized for the multiaxial case to provide the crack damage on the plane of maximum plastic shear strain range as

$$\dot{D} = C_0 |\varepsilon_{\mathrm{p}}^s|^m |\dot{\varepsilon}_{\mathrm{p}}^s|^k \quad , \tag{1.19}$$

with $\varepsilon_{\mathrm{p}}^s$ and $\dot{\varepsilon}_{\mathrm{p}}^s$ being the current plastic shear strain and strain rate, respectively, on the plane of the maximum plastic shear strain range. As in the uniaxial approach, the plastic shear strain is measured from the previous point of reversal of the plastic shear strain. The coefficients C_0 as well as the exponents m and k are assumed to be functions of two dimensionless loading parameters defined as $\Delta\varepsilon_{\mathrm{p}}^n/\Delta\varepsilon_{\mathrm{p}}^s$ and p/σ_{eff}, where $\Delta\varepsilon_{\mathrm{p}}^s$ is the maximum plastic shear strain range, $\Delta\varepsilon_{\mathrm{p}}^n$ the maximum plastic strain range perpendicular to the plane on which $\Delta\varepsilon_{\mathrm{p}}^s$ acts, p the hydrostatic pressure and σ_{eff} the von Mises effective stress.

Satoh and Krempl (1982) have modified Majumdar and Maiya's law. Essentially, the plastic strain was replaced by the stress. Thus, the time-incremental approach of Satoh and Krempl can account for possible interaction between stress and plastic strain. To extend this uniaxial rule, Yeh and Krempl (1993) have also exploited the idea of Brown and Miller (1973) for multiaxial loading. However, their approach is not based on the maximum shear strain range but on the maximum shear strain rate and, thus, can be applied to any complex loading path without using a single parameter, such as the maximum shear strain range, in order to characterize the damage effect of a whole cycle. The fatigue damage rate is described by the following evolution equation

$$\dot{D}_{\mathrm{f}} = L_{\mathrm{f}}(\omega) \left| \frac{\dot{\varepsilon}_{\mathrm{p}}^s}{\dot{\varepsilon}_{\mathrm{f}}} \right|^{n_{\mathrm{f}}} \left| \frac{\sigma_{\mathrm{eff}}}{\sigma_{\mathrm{f}}} \right|^{m_{\mathrm{f}}} \left[1 + a \left(1 - \frac{\mathrm{tr}\,(\boldsymbol{\sigma})}{\sigma_{\mathrm{eff}}} \right) \right] \quad , \tag{1.20}$$

where σ_{eff} is the von Mises effective stress, $\mathrm{tr}\,(\boldsymbol{\sigma}) = \sigma_1 + \sigma_2 + \sigma_3$ is the first invariant (trace) of the stress tensor, $\dot{\varepsilon}_{\mathrm{p}}^s = 2/3 \left| \dot{\varepsilon}_{\mathrm{p}}^1 - \dot{\varepsilon}_{\mathrm{p}}^3 \right|$ and $\dot{\varepsilon}_{\mathrm{p}}^n = 2 \left| \dot{\varepsilon}_{\mathrm{p}}^1 + \dot{\varepsilon}_{\mathrm{p}}^3 \right|$ are the normalized maximum shear strain rate and the normalized inelastic strain rate perpendicular to the plane on which $\dot{\varepsilon}_{\mathrm{p}}^s$ acts, respectively. The word "normalized" denotes that their values in the multiaxial case reduce to the uniaxial values for uniaxial loading. L_{f} is a non-negative function of the quantity $\omega = \dot{\varepsilon}_{\mathrm{p}}^n/\dot{\varepsilon}_{\mathrm{p}}^s$. In the case of pure torsion, ω is equal to zero and equal to unity for uniaxial loading. $\dot{\varepsilon}_{\mathrm{f}}$, σ_{f}, n_{f}, m_{f} and a are material constants, whereby $\dot{\varepsilon}_{\mathrm{f}}$ is introduced only for dimensional consideration.

It should be emphasized that the quantity $\dot{\varepsilon}_{\mathrm{p}}^s$, used in Yeh and Krempl's approach, is different from the one in Majumdar's approach. So, $\dot{\varepsilon}_{\mathrm{p}}^s$ from equation (1.19) is not the maximum plastic shear strain rate as it is the case in equation (1.20) but the plastic shear strain rate on the plane of the maximum plastic strain range. Thus, in contrast to Majumdar's approach, Yeh and Krempl's life rule does not require the determination of any "ranges" and, consequently, is independent of the cycle concept. The other advantage of the Yeh and Krempl's life rule is the fact that it can account, via dependence on both the stress and the plastic strain, for their possible interaction.

In the next section we will derive an anisotropic lifetime rule for single-crystal superalloys. In doing so we will try to adopt these both advantages.

1.4 A three-dimensional lifetime rule for single crystals

1.4.1 Model formulation

Just like the deformation behavior, the fatigue failure of single crystals is orientation dependent. Since the low cycle fatigue is mainly controlled by the plastic deformation, one would expect that, *e.g.*, in a strain controlled cyclic test the specimen with the orientation exhibiting a lower yield strength will fail earlier due to a higher plastic deformation portion if both orientations are tested at the same strain range. So, $\langle 111 \rangle$ oriented specimens of the CMSX4 superalloy exhibit lower life then $\langle 100 \rangle$ oriented tests due to the lower yield stress in the $\langle 111 \rangle$ direction. Thus, to capture the orientation dependent multiaxial fatigue behavior of a single crystal such as the superalloy CMSX4 an anisotropic multiaxial failure criterion is needed.

As originally proposed by Majumdar and Maiya (1980) we base the lifetime rule on a time-incremental propagation law for a dominant small crack

$$\dot{a} = a\,\mathrm{f}\left(\tau_\alpha, \dot{\gamma}_\alpha\right), \qquad \alpha = 1, ..., N \quad . \tag{1.21}$$

However, we do not use the concept of the maximum plastic shear strain rate but work with the crystallographic slips that are much more natural in the case of single crystals and represent the actual quantities controlling fatigue crack initiation and growth in the early stage. We assume that the nonlinear function $\mathrm{f}\left(\tau_\alpha, \dot{\gamma}_\alpha\right)$, controlling the crack growth rate, depends on macroscopic resolved shear stresses τ_α and crystallographic slip rates $\dot{\gamma}_\alpha$. At the same time, the use of the crystallographic quantities allows us to capture the orientation dependency of the fatigue failure, just as an crystallographic deformation model enables us to describe the anisotropic stress-strain response of a single crystal.

a is the length of a dominant small crack. No crack growth on a certain slip plane is meant. It is assumed that the crack is created early in the life at an already initially presented defect, *e.g.*, a casting pore (Miller *et al.*, 2004) with size a_0. With such an initial crack length a_0 (1.21) can be rewritten as

$$\frac{d\,\ln(a/a_0)}{d\,t} = \mathrm{f}\left(\tau_\alpha, \dot{\gamma}_\alpha\right) \tag{1.22}$$

and normalized by the relation of the failure crack length a_f to the initial crack length a_0

$$\frac{d}{d\,t}\,\frac{\ln(a/a_0)}{\ln(a_\mathrm{f}/a_0)} = \frac{\mathrm{f}\left(\tau_\alpha, \dot{\gamma}_\alpha\right)}{\ln(a_\mathrm{f}/a_0)} \quad . \tag{1.23}$$

With the lifetime consumption variable

$$D := \frac{\ln(a/a_0)}{\ln(a_\mathrm{f}/a_0)}, \qquad 0 \leqslant D \leqslant 1 \tag{1.24}$$

(1.23) represents a time incremental lifetime rule

$$\dot{D} = \frac{f(\tau_\alpha, \dot{\gamma}_\alpha)}{\ln(a_\mathrm{f}/a_0)} \quad . \tag{1.25}$$

The lifetime consumption corresponding to the increase of the crack length from a_1 to a_2 is according to (1.24) evaluated as

$$D_2 - D_1 = \frac{\ln(a_2/a_0) - \ln(a_1/a_0)}{\ln(a_\mathrm{f}/a_0)} = \frac{\ln(a_2/a_1)}{\ln(a_\mathrm{f}/a_0)} \quad . \tag{1.26}$$

In the section on the deformation behavior of single crystals, we mentioned that the anisotropic deformation model of Cailletaud is the transformation of the one-dimensional form of the proved isotropic Chaboche model to each slip system. We will use the same procedure to obtain a concrete expression for the function $\mathrm{f}\left(\tau_\alpha, \dot{\gamma}_\alpha\right)$ in order to take the advantages of the Yeh and Krempl's approach, consisting in accounting for a possible interaction between the stress and plastic strain. Keeping the functional structure of equation (1.20) and using the crystallographic quantities instead of the invariant effective stresses and strains we arrive at the following crystallographic counterpart to the Yeh and Krempl's lifetime rule (Levkovitch *et al.* , 2004)

$$\dot{D} = \sum_{\alpha=1}^{12} \left(\frac{|\tau_\alpha|}{s_{\text{oct}}} \right)^{m_{\text{oct}}} \left(\frac{|\dot{\gamma}_\alpha|}{\dot{\gamma}_{0\,\text{oct}}} \right)^{n_{\text{oct}}} \dot{\gamma}_{0\,\text{oct}} + \sum_{\alpha=1}^{6} \left(\frac{|\tau_\alpha|}{s_{\text{cub}}} \right)^{m_{\text{cub}}} \left(\frac{|\dot{\gamma}_\alpha|}{\dot{\gamma}_{0\,\text{cub}}} \right)^{n_{\text{cub}}} \dot{\gamma}_{0\,\text{cub}} \tag{1.27}$$

with τ_α and $\dot{\gamma}_\alpha$ being the resolved shear stress and the inelastic shear strain rate on the slip system α, respectively. Similar to the material model of Cailletaud, we use the octahedral and cube slip families for single crystal superalloys. Thus, the resolved shear stresses and the inelastic shear strain rates are obtained from the deformation analysis. In view of the definition (1.24) of the damage variable D, leading via (1.25) to crack propagation law (1.21), each summand on the right hand side of (1.27) represents just the loading contribution of each slip system. Using the Cailletaud model the damage evolution equation (1.27) is integrated alongside with the constitutive equation of the material model. As in the deformation model, each slip family has its own damage constant set, consisting of three independent parameters s, m and n ($\dot{\gamma}_0$ is just a normalization constant), which enables us to model the dependence of the lifetime on the crystal orientation.

The material parameters s and m describe the stress-dependence of the lifetime behavior. They are determined essentially by LCF tests with different strain or stress ranges but without hold-times. The parameter n describes the time-dependence of the lifetime due to creep and oxidation: for rate-independent behavior n is equal to 1; n equal to zero means that a fully time-dependent lifetime behavior is present. The parameter n is determined essentially by the influence of the hold-times in the LCF tests on the lifetime. n was found to be positive but significantly lower than 1 for the investigated high temperature loading.

1.4.2 Application to CMSX4

A gas-turbine blade is a cyclically loaded component part. Therefore strain- and stress-controlled cyclic tests with and without hold-times are used to characterize the lifetime behavior. The hold-times approximate the service loading conditions. The damage parameters of the octahedral slip family are calibrated by $\langle 100 \rangle$ oriented specimens and those of the cubic family by $\langle 111 \rangle$ and $\langle 110 \rangle$ oriented specimens using an optimization procedure. The difference between the measured and evaluated number of cycles to failure is used as the objective function of the optimization.

Formally, the evaluation of the number of cycles to failure requires the integration of the damage evolution equation (1.27) along with the constitutive equations of the material model (the damage evolution equation needs as an input stresses and inelastic strains obtained from deformation analysis) until the life consumption variable D reaches the value one. Since the life of many fatigue tests lies in the range between 10000 and 100000 cycles, this formal integration procedure would lead to computational times whose usage in an optimization process, where the objective function must be calculated many times before the optimum solution is found, would be completely unrealistic. Therefore, we used the concept of a steady-state cycle. The integration of the evolution equation (1.27) shows that the accumulated damage value ΔD during one cycle reaches a constant value (cyclic saturation state) after a certain number of cycles. Thus, in fact we need to integrate the damage evolution equation only up to the saturated cycle. Admittedly, the number of cycles to saturation can still be too high to be used in an optimization process. However, the number of cycles up to saturation can usually be neglected in comparison to the number of cycles to failure. That means that the cyclic life N_{f} can be approximated by taking the inverse of the damage value $\Delta D_{\mathrm{Steady}}$ accumulated during a steady-state cycle $N_{\mathrm{f}} = 1/\Delta D_{\mathrm{Steady}}$. To obtain $\Delta D_{\mathrm{Steady}}$ the damage evolution equation (1.27) has, of course, to be integrated over the full saturated cycle. For this damage integration we need to know the stress and strain values from the deformation analysis. Since the Cailletaud model is history dependent, to obtain these values we need to integrate the constitutive equation of the material model up to the saturation. However, this integration of the material model up to the saturation needs to be done only once, since the variations of the damage parameters during the damage optimization process have no influence on the deformation behavior. Thus, once integrated up to the saturation state, the integration of the constitutive equation of the material model can be resumed from this point on in order to deliver the input for the damage evolution equation in the saturated cycle. Proceeding in such a way, the time needed for the optimization process can be reduced significantly and allows to include a very high number of experiments into the optimization.

Using this approach we applied the lifetime rule (1.27) to the nickel-base superalloy CMSX4 subjected to a variety of loading conditions, *i.e.*, stress and strain controlled cyclic tests at different rates, different R values (R value is the ratio of the minimum to the maximum value of the controlled quantity in a cyclic test) as well as without and with hold-times. A good agreement could be achieved with only one set of damage parameters (Figure 1.8).

In order to test the life rule for multiaxial loading conditions, simulation results for a cyclically loaded single crystal flat specimen with a hole have been compared with corresponding experimental results. Such a flat specimen with a hole represents in a coarse approximation a surface segment of a gas turbine blade with a film cooling channel which is required to form

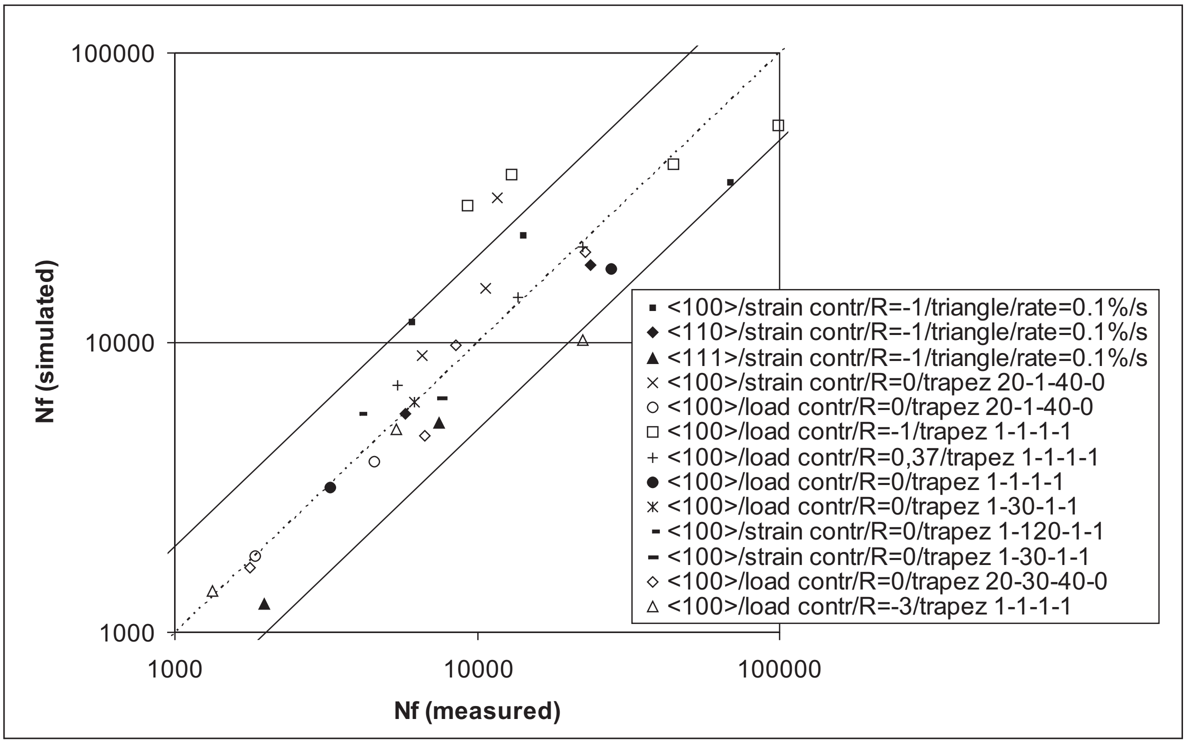

Figure 1.8: Fatigue lifetime assessment for CMSX-4 at 950° C for different crystal orientations and various load profiles (test environment: air)

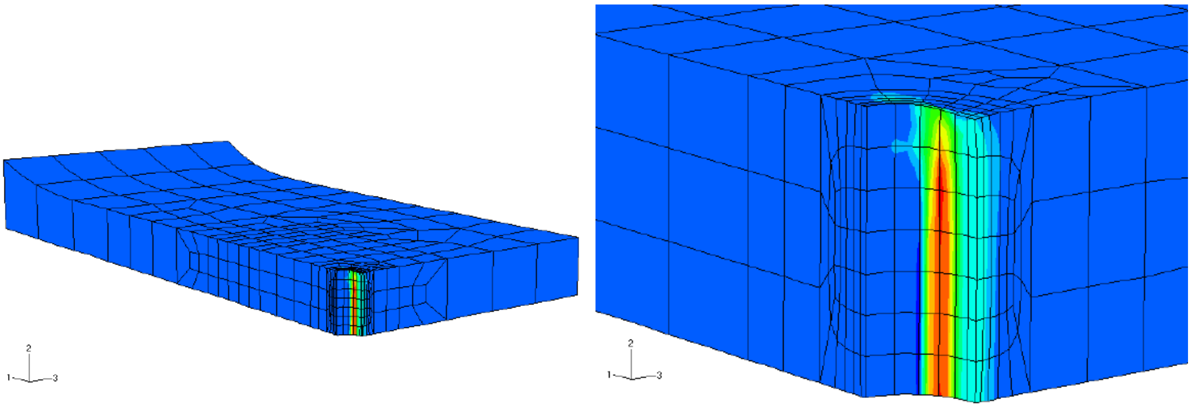

Figure 1.9: Location of maximum lifetime consumption D in a CMSX4 flat specimen with a hole after cyclic loading at $950°$, edges oriented along the crystal axes

a thin film of cooling air on the surface (see, *e.g.*, Pan *et al.*, 1999). The predicted lifetime is within the factor of two compared to the measured one. As shown in Figure 1.9 the maximum of the damage measure D is located not directly in the notch root at external loading in the $\langle 100 \rangle$ direction. Such a shift relative to the notch root is also present for the location of the initiation of a macro-crack at a notch found experimentally for another precipitation-strengthened fcc single crystal (Boubidi and Sievert, 2002).

1.5 Conclusion

We have presented a three-dimensional anisotropic time-incremental lifetime rule that was applied to describe the low-cycle fatigue of the single crystal superalloy CMSX4 at high temperatures. The life time rule was developed on the basis of the Satoh and Krempl (1982) one-dimensional damage accumulation equation in which the damage rate is controlled by the current values of the stress and inelastic strain rate. To convert this approach into a three-dimensional anisotropic damage law suitable for single crystals we assumed that the damage contribution rate of each slip system to the total damage is governed by the current values of the resolved shear stress and the slip rate on this slip system, whereby the functional form is adopted from the Satoh and Krempl equation. The damage law was coupled with the crystallographic Cailletaud model which was modified in order to describe a ”fast” softening effect observed in tensile tests for different orientations. With only one parameter set fairly good results could be achieved in the simulation of the deformation behavior in one-dimensional tensile tests with different strain rates, strain-controlled LCF tests with different strain ranges and creep tests with different stress levels for the three orientations $\langle 100 \rangle$, $\langle 110 \rangle$ and $\langle 111 \rangle$. The capability of the model was also confirmed by the simulation of randomly oriented tests and of LCF tests with hold times.

The same is valid for the fatigue life simulation. Using a broad range of loading conditions, *i.e.*, stress and strain controlled cyclic tests at different rates, different R values and with and without hold-times we could achieve a good agreement with only one set of damage parameters. The damage model was also tested for the case of multiaxial loading conditions. To this end, the life time of a cyclically loaded single crystal flat specimen with a hole was evaluated with the proposed damage model. The predicted lifetime was within a factor of two compared to the measured one.

1.6 Acknowledgment

The authors would like to thank Rolls-Royce Deutschland (RRD) and the Federal Institute for Materials Research and Testing (BAM) for providing funding and RRD for performing the tests for this work. The tests were carried out within the German government sponsored aeronautical research and technology program under contract number 20T9903.

References

Arakere, N.,K., and E. Orozco, E., 2001. Analysis of low cycle fatigue properties of single crystal nickel-base turbine blade superalloys. High Temperature Materials and Processes, 20, 403–419.

Basquin, O.H., 1910. The exponential law of endurance test. Proc. ASTM, 10 (II), 625–630.

Bettge, D., Österle, W., 1999. ”Cube slip” in near-[111] oriented specimens of a single-crystal nickel-base superalloy. Scripta Mater., 40, 389–395.

Blass, J.J., and Zamrik, S.Y., 1976. Multiaxial Low-Cycle Fatigue of Type 304 Stainless Steel. Proc. ASME-MPC Symposium on Creep-Fatigue Interaction, MPC-3, R.M. Curran Ed., New York, December 1976, 129-159

Boubidi, P., Sievert, R., 2002. Experimental and numerical investigations of macro-crack initiation under low-cycle fatigue loading at notches in a single crystal superalloy at high temperature. G. Biallas et al. (eds.), High-Temperature Fatigue, CAMP 2002, University of Paderborn, Germany, 127–141.

Brown, M.W., Miller, K.J., 1973. A theory for fatigue failure under multiaxial stress-strain conditions. Proc. Inst. Mech. Engrs., 187, 745–755.

Bullough, C.K., Toulios, M., Oehl, M., Lukas, P., 1998. The characterisation of the single crystal superalloy CMSX-4 for industrial gas turbine blading applications. Proc. 6th Liege Conf., Liege, 861–878.

Busso, E. F., Meissonnier, F. T., O’Dowd, N. P., 2000. Gradient-dependent deformation of two-phase single crystals. J. Mech. Phys. Solids, 48, 2333–2361.

Cailletaud, G., Chaboche, J.L., Forest. S., Remy, L., 2003. On the design of single crystal turbine blades. La Revue de Métallurgie, Février 2003, 165–172.

Chaboche, J.L., 1977. Viscoplastic constitutive equations for the description of cyclic and anisotropic behavior of materials. 17 Polish Conf. on Mechanics of Solids, Szezyrk, 1975, Bull. de l’Acad. Polonaise des Sciences, Série Sc. et Techniques, Vol. 25, 33–42.

Chaboche, J.L., Gallerneau, F., 2001. An overview of the damage approach of durability modelling at elevated temperature. Fatigue Fract. Engng. Mater. Struct. 24, 405–418.

Coffin, L.F., 1954. A study of the effects of cyclic thermal stresses on a ductile metal. Trans. ASME, 76, 931–950.

Danzer, R., 1987. Eine Methode der Lebensdauerprognose für hochfeste metallische Werkstoffe im Bereich der Kriech-Ermdungs-Wechselwirkung. Z. Metallkd. 78, 19–31.

Ellyn, F., Kujawski, D., 1986. An energy-based fatigue failure criterion. Microstructure and Mechanical Behavior of Materials, Vol II (eds. H. Gu and J. He), EMAS, West Midlands, UK, 541–600.

Henderson, M.B., Martin, J.W., 1996. The influence of crystal orientation on the high temperature fatigue crack growth of a Ni-based single crystal superalloy. Acta Materialia 44 (1). 111–126.

Kanazawa, K., Miller, K.J., Brown, M.W., 1977. Low-Cycle Fatigue Under Out-of-Phase Loading Conditions. J. Engrg. Mater. Technol., 99, 222–228.

Levkovitch, V., Sievert, R., Svendsen, B., 2004. Simulation of low-cycle fatigue failure of fcc single crystals. LCF 5, Proc. Fifth Int. Conf. on Low Cycle Fatigue, P.D. Portella *et al.* (Eds.), Deutscher Verband für Materialforschung und -prüfung (DVM), 415–420.

Levkovitch, V., Sievert, R., Svendsen, B., 2005. Application of extended crystal plasticity to the modeling of glide and kink bands and of crack opening in single crystals, Comp. Mat. Sci., 32, 426–434.

Li, S.X., Smith, D.J., 1995. High temperature fatigue-creep behavior of single crystal SRR99 nickel base superalloys: part II – fatigue-creep life behaviour. Fatigue Fract. Engng. Mater. Struct. 18, 631–643.

MacLachlan, D.W., Knowles D.M., 2001. Fatigue behavior and lifing of two single crystal superalloys. Fatigue Fract. Engng. Mater. Struct. 24, 503–521.

Majumdar, S., Maiya, P.S., 1980. A mechanistic model for time-dependent fatigue. J. Eng. Mater. Technol., Trans. ASME, 102, 159–167

Majumdar, S., 1981. Designing against low-cycle fatigue at elevated temperature. Nuclear Engineering and Design, 63, 121–135.

Manson, S.S., 1954. Behaviour of materials under conditions of thermal stress. NACA TN-2933, National Advisory Committee for Aeronautics.

Meric, L., Poubanne, P., Cailletaud, G., 1991. Single crystal modeling for structural calculations: part 1 - model presentation. J. Engng. Mat. Technology 113, 162–170.

Miller, M.D., Reed, P.A.S., Joyce, M.R., Henderson, M.B., Brooks, J., Wilcock, I.M. and Wu, X., 2004. Effect of temperature and secondary orientation on notch fatigue resistance of CMSX4. Int. Conf. Fatigue Damage of Structural Materials, Hyannis, 2004.

Nouailhas, D., 1989. Unified modelling of cyclic viscoplasticity: application to austenitic stainless steels. Int. J. Plast. 5, 501–520.

Pan, Y., Bischoff-Beiermann, B., Schulenberg, T., 1999. Material testing for fatigue design of heavy-duty gas turbine blading with film cooling. Fatigue Design and Reliability, G. Marquis and J. Solin (Eds), ESIS Publication 23, Elsevier. 155–162.

Remy, L., 2001. Fatigue and thermomechanical fatigue at high temperature. Encyclopedia of Materials: Science and Technology, Elsevier Science Ltd. 2866–2877.

Reuchet, J., Remy, L., 1983. Fatigue oxidation interaction in a superalloy – application to life prediction in high temperature low cycle fatigue. Metall. Mater. Trans. A 14A, 141–149.

Rezai-Aria, F., Remy, L., 1989. An oxidation fatigue interaction damage model for thermal fatigue crack growth. Eng. Fract. Mech. 34, 283-294.

Satoh, M., Krempl, E., 1982. An incremental life prediction law for creep-fatigue interaction. Material Behaviour at Elevated Temperatures and Components Analysis, PVP 10 (eds. Y. Yamada *et al.*), American Society of Mechanical Engineers, New York, 71–79.

Sermage, J.P., Lemaitre, J., Desmorat. R., 2000. Multiaxial creep-fatigue under anisothermal conditions. Fatigue Fract. Engng. Mater. Struct. 23, 241–252.

Sievert, R., Österle, W., Olschewski, J., Ziebs, J., 1997. Physical interpretation of a viscoplastic model applied to high temperature performance of a nickel-base superalloy. Z. Metallkd. 88, 416–424

Suresh, S., 1998. Fatigue of materials. Cambridge University Press.

Yeh, N., Krempl, E., 1993. An incremental life prediction law for multiaxial creep-fatigue interaction and thermomechanical loading. Advances in Multiaxial Fatigue, ASTM STP, 1191, 107–119.

Chapter 2

Extended deformation modeling of single crystals: effect of geometrically necessary dislocations[*]

Abstract– The purpose of this work is the application of continuum thermodynamics to the extension of standard crystal plasticity to account for the effects of the development of geometrically-necessary dislocations (GNDs) on the material behaviour. To this end, following Nye and many others, local deformation incompatibility in the material is adopted as a measure of the density of GNDs. Their development results in additional energy being stored in the material, resulting in additional kinematic-like hardening effects. The current approach generalized previous ones in that the thermodynamic formulation is based on the notion of generalized energy flux. A detailed comparison of the current approach and its results with previous such approaches and their results is given.

2.1 Introduction

The lengthscale- or size-dependence of material behaviour in materials and structures in which characteristic continuum dimensions approach characteristic microstructural lengthscales (*e.g.*, grain size) is by now well-documented (at least in fcc-based systems), having been repeatedly confirmed in different experiments. For example, in torsion tests on thin wires with diameters between 12 to 170 μm, Fleck *et al.* (1994) observed increasing hardening with the decreasing wire-thickness. Stölken and Evans (1998) observed this as well in bending experiments on thin beams as the beam thickness decreases from 50 to 12.5 μm. Microindentation tests on single crystals displayed the same tendency. In the case of indentation tests, Stelmashenko *et al.* (1993) showed that the measured indentation hardness increases as the depth of the indentation decreases from 10 to 1 μm. All these tests show the same tendency, *i.e.*, the smaller the specimen size, the larger the increase in hardening. Since standard plasticity models do not account for such a lengthscale or size-dependent hardening behaviour, they predict flow stresses independent of this. In addition, tests exhibiting size-dependence behaviour have in common the fact that, in contrast to conventional tests (*e.g.*, tensile tests), material anisotropy and the imposed kinematic constraints (*e.g.*, at grain boundaries) lead to instability of the initially-homogeneous deformation field and to the emergence of energetically more-favorable localized inhomogeneous deformation in the form of, *e.g.*, dislocation substructures (*e.g.*, Ortiz *et al.*, 2000).

As has been pointed out in many works, the phenomena of increasing hardening due to increasing deformation inhomogeneity can be explained (*e.g.*, Ashby, 1970) by the fact that such deformation is accommodated locally via the generation of additional, so-called geometrically necessary dislocations (GNDs). These arise via the net build-up of single-sign “polar” or “excess” dislocations at local obstacles to dislocation motion, *e.g.*, precipitates or grain boundaries, facilitating local inhomogeneous and incompatible deformation which would otherwise take the form of energetically less-favorable local lattice deformation. In contrast to the build-up of "non-polar" or "neutral" dislocation dipoles, then, that of "polar" or "charged" GNDs results in a net Burgers vector. Together with the random trapping of dislocation dipoles resulting in so-called statistically-stored dislocations (SSDs), then, the buildup of GNDs leads to a further increase in the total dislocation density. As such, the emergence of GNDs results in both additional hardening in the system and its lengthscale-dependence (Ashby, 1970). In his pioneering work, Nye (1953) introduced the dislocation density tensor whose three diagonal components can be interpreted as excess screw contributions, and the six off-diagonal components as excess edge contributions, to the dislocation density. Since the production of excess dislocations implies local closure failure, they result in Burgers vector production and in local incompatibility in the deformation field. Consequently, such incompatibilty can be taken as a continuum measure of the presence of such dislocations. In the small deformation context, Nye established in addition a relation between the dislocation density and the lattice curvature tensors. In particular, he showed that edge-type GNDs result in the lattice bending, and screw-type GNDs lead to lattice twisting. Exactly this connection between the dislocation density tensor and the lattice curvature has been used in Sun *et al.* (1998) or El-Dasher *et al.* (2003) to determine the GND density with the help of electron back scattering diffraction and (lattice) orientation image microscopy. In addition, the correlation between decrease of specimen size and the increase of local deformation inhomogeneity and so of local deformation incompatibility would imply that the GND density increases with decreasing specimen size, leading to the observed correlation between specimen size and additional hardening.

---

[*] submitted 2005 to *International Journal of Solid and Structures* under the title:
”On the large-deformation- and continuum-based formulation of models for extended crystal plasticity”.

Even in such "simple" tests as microtorsion or microbending, GND development due to local deformation incompatibility results in size-dependent material behaviour. More generally, phenomena such as precipitate hardening of metallic materials (higher yield stresses in the case of smaller particle but unchanged volume-fraction precipitation/matrix: Ashby, 1970) and the Hall-Petch effect (hardening of polycrystals by decreasing the grain size) can be explained using the GND concept. In both cases, local deformation incompatibility results from the contrast in kinematic and/or material properties at phase boundaries (*e.g.*, at the interface between the precipitates and matrix, or at grain boundaries), and is accommodated by GND development. Since a decreasing particle or grain size implies a higher percentage of such interfaces, a fine-precipitate or fine-grained material is generally harder. In addition to their role in hardening, GNDs may also play a significant role in deformation localization in metallic materials. In single crystals, for example, one observes the development of slip bands parallel to the active slip plane, and that of kink bands inclined to the active slip plane (*e.g.*, Flouriot *et al.*, 2003). In contrast to slip-band formation, kink-band formation involves local lattice rotation and bending, resulting in local lattice curvature. To accommodate such local deformation inhomogeneity in the form of lattice curvature, GNDs accumulate at kink-band boundaries. Because kink band formation always involves strong lattice curvature, it is energetically less favorable than slip band formation, which involves none. That is the reason why slip bands are observed much more frequently than kink bands. Because it does not account for the presence of GNDs and their effect on the material behaviour, standard crystal plasticity does not distinguish between the different nature of slip and kink bands. Indeed, it predicts similar resistance against the developing of the both types of shear bands in spite of their different nature (Asaro and Rice, 1979).

The fact that standard crystal plasticity accounts only for the effect of the history of crystallographic slip, *i.e.*, of SSDs, on the hardening behaviour, has motivated a number of workers to propose a number of extensions to standard phenomenological plasticity and crystal plasticity. Prominent among these is the Mindlin-continuum- or strain-gradient-based extension of phenomenological plasticity of Fleck and Hutchinson (*e.g.*, Fleck and Hutchinson, 1993; Fleck *et al.*, 1994; Fleck and Hutchinson, 1997), which has also been applied to crystal plasticity (*e.g.*, Shu and Fleck, 1999). Alternatively, the association of GNDs with local lattice rotation and bending has motivated the use of Cosserat theory for this purpose (*e.g.*, Forest *et al.*, 1997, 2001, 2002). With regard to extensions of crystal plasticity, by far the largest number have been based on continuum dislocation concepts, and in particular on the idea of Nye (1953) that the incompatibility of local inelastic deformation represents a continuum measure of dislocation density (see also Kröner, 1960; Mura, 1987). These include Steinmann (1996); Dai and Parks (1997); Shizawa and Zbib (1999); Acharya and Bassani (2000); Menzel and Steinmann (2000); Svendsen (2000); Cermelli and Gurtin (2001); Gurtin (2002); Svendsen (2002); Evers *et al.* (2004). In addition, the recent work of Ortiz *et al.* (2000) on dislocation substructures in ductile single crystals demonstrates the fundamental connection between the incompatibility of the local inelastic deformation and lengthscale of dislocation microstructures in fcc single crystals. Except for the works of Acharya and Bassani (2000) and Cermelli and Gurtin (2001), which are restricted to kinematics, all of these presume directly or indirectly a particular dependence of the (free) energy and/or other dependent constitutive quantities (*e.g.*, yield stress) on the gradients of inelastic state variables, and in particular on that of the local inelastic deformation, *i.e.*, that determine its incompatibility. In the simplest case (*e.g.*, Dai and Parks, 1997; Acharya and Bassani, 2000; Acharya *et al.*, 2003), one simply introduces the GND density as an additional dislocation density into standard (*i.e.*, SSD-based) hardening models, resulting in an additional increase in the yield stress and no change in the boundary-value problem to be solved. In these approaches, the yield stress increase due to GNDs doesn't depend on the dislocation sign, although simple arguments based on the elastic properties of dislocations reveal that nonhomogeneous distribution of excess dislocation of the same sign lead necessarily to directional internal stresses. This fact was used by Evers *et al.* (2004) in a non-thermodynamic approach including both short-range (nondirectional) and long-range (directional) internal stresses due to GNDs. In particular, they introduced GND densities for each slip system determined by glide-system slip gradients in the sense of Ashby (1970).

If one assumes that GND development and more generally local deformation incompability results in energy storage in the material, then the free energy necessarily depends[1] on the dislocation density tensor. In particular, in the crystal plasticity context, this assumption leads to a generalized, non-local glide-system flow rule representing an evolution field relation for the glide-system slips. In particular, this field relation contains terms depending on the second spatial derivatives of these slips (*e.g.*, Svendsen, 2000, 2002) or their rates (*e.g.*, Gurtin, 2000, 2002). Like the resolved shear stress, these additional terms are signed and influence the effective resolved stress driving glide-system dislocation motion. Consequently, they are of back-stress character. In both the thermodynamic and non-thermodynamic approaches, the standard flow rule for the glide system slip generalizes to an evolution field relation, such that each scalar (active) glide-system slip represents an additional continuum degree of freedom for which additional boundary conditions are required. In this regard, the approach of Gurtin (2002) is based on the concept of a microforce or configurational force balance (*e.g.*, Gurtin, 2000) for each glide-system slip. On the other hand, Svendsen (2000, 2002) showed that exploitation of the invariance of the energy balance and of the dissipation principle results in additional such evolution field relations for the glide-system slips having a generalized Ginzburg-Landau or Cahn-Allen form. As such, the glide-system slips can be interpreted as a type of phase-field in this context (as discussed in detail in Svendsen and Reese, 2003; Svendsen, 2004). Such an approach has been applied in a number of contexts, *e.g.*, to the modeling and simulation of glide- and kink-banding at the crack-tip in single crystals (Levkovitch *et al.*, 2005). In particular, the GND-related hardening is shown there to influence only kink band development (*i.e.*, reduces their intensity).

---

[1] That this isn't "absolutely" necessary in order to account for directional hardening effects is demonstrated both by the crystal plasticity model work of Evers *et al.* (2004) and the very interesting phenomenological approach of Acharya (2004).

In the current work, a non-local thermodynamic single-crystal model is formulated which accounts in particular for additional kinematic hardening due to GNDs. This approach is based on direct exploitation of the dissipation principle to derive all field relations and (sufficient) forms of the constitutive relations as based on the free energy density and dissipation potential. The current formulation falls within the framework of inelastic gradient formulations, which sets it apart from the strain-gradient-based approach to crystal plasticity of Shu and Fleck (1999). Before we begin, a word on notation. If W and Z represent two finite-dimensional linear spaces, let $\mathrm{Lin}(W,Z)$ represent the set of all linear mappings from W to Z. If W and Z are inner product spaces, the inner products on W and Z induce the transpose $\mathcal{A}^{\mathrm{T}} \in \mathrm{Lin}(Z,W)$ of any $\mathcal{A} \in \mathrm{Lin}(W,Z)$, as well as the inner product $\mathcal{A} \cdot \mathcal{B} \;:=\; \mathrm{tr}_W(\mathcal{A}^{\mathrm{T}}\mathcal{B}) = \mathrm{tr}_Z(\mathcal{A}\mathcal{B}^{\mathrm{T}})$ on $\mathrm{Lin}(W,Z)$ for all $\mathcal{A},\mathcal{B} \in \mathrm{Lin}(W,Z)$. In particular, let V represent three-dimensional Euclidean vector space, $\mathrm{Lin}(V,V)$ the set of all linear mappings of V into itself (*i.e.*, second-order Euclidean tensors), and $\mathrm{Lin}^{+}(V,V)$ the subset of all elements of $\mathrm{Lin}(V,V)$ with positive determinant. Elements of V and $\mathrm{Lin}(V,V)$, or mappings taking values these spaces, are denoted here as usual by bold-face, lower-case $\boldsymbol{a}$, . . . and upper-case $\boldsymbol{A}$, . . ., italic letters, respectively. In particular, let $\boldsymbol{I} \in \mathrm{Lin}(V,V)$ represent the second-order identity tensor. As usual, the tensor product $\boldsymbol{a} \otimes \boldsymbol{b}$ of any two $\boldsymbol{a},\boldsymbol{b} \in V$ can be interpreted as an element $\boldsymbol{a} \otimes \boldsymbol{b} \in \mathrm{Lin}(V,V)$ of $\mathrm{Lin}(V,V)$ via $(\boldsymbol{a} \otimes \boldsymbol{b})\boldsymbol{c} := (\boldsymbol{b} \cdot \boldsymbol{c})\boldsymbol{a}$ for all $\boldsymbol{a},\boldsymbol{b},\boldsymbol{c} \in V$. In addition, $\mathrm{sym}(\boldsymbol{A}) := \frac{1}{2}\,(\boldsymbol{A} + \boldsymbol{A}^{\mathrm{T}})$, $\mathrm{skw}(\boldsymbol{A}) := \frac{1}{2}\,(\boldsymbol{A} - \boldsymbol{A}^{\mathrm{T}})$, $\mathrm{sph}(\boldsymbol{A}) := \frac{1}{3}\,\mathrm{tr}(\boldsymbol{A})\,\boldsymbol{I}$, and $\mathrm{dev}(\boldsymbol{A}) := \boldsymbol{A} - \mathrm{sph}(\boldsymbol{A})$ represent the symmetric, skew-symmetric, spherical, and deviatoric, parts, respectively, of any $\boldsymbol{A} \in \mathrm{Lin}(V,V)$. Let $\mathrm{axv}(\boldsymbol{W}) \times \boldsymbol{a} \;:=\; \boldsymbol{W}\boldsymbol{a}$ represent the axial vector of any skew-symmetric tensor $\boldsymbol{W}$, and $\mathrm{axs} := \mathrm{axv} \circ \mathrm{skw}$ the extension of the axial vector mapping to arbitrary second-order tensors.

Third-order tensors are denoted in general in this work by upper-case slanted sans serif letters A, B, . . . and interpreted as elements of $\mathrm{Lin}(V^2,V) \cong \mathrm{Lin}(\mathrm{Lin}(V,V),V) \cong \mathrm{Lin}(V,\mathrm{Lin}(V,V))$. Note that any third-order tensor A induces a third-order tensor A^{S} defined by $(\mathsf{A}^{\mathrm{S}}\boldsymbol{b})\boldsymbol{c} \;:=\; (\mathsf{A}\boldsymbol{c})\boldsymbol{b}$. In particular, this operation induces the split $\mathsf{A} = \mathrm{sym}_{\mathrm{S}}(\mathsf{A}) + \mathrm{skw}_{\mathrm{S}}(\mathsf{A})$ of any third-order tensor A into "symmetric" $\mathrm{sym}_{\mathrm{S}}(\mathsf{A}) \;:=\; \frac{1}{2}(\mathsf{A} + \mathsf{A}^{\mathrm{S}})$ and "skew-symmetric" $\mathrm{skw}_{\mathrm{S}}(\mathsf{A}) \;:=\; \frac{1}{2}(\mathsf{A} - \mathsf{A}^{\mathrm{S}})$ parts. In addition, the latter of these induces the second-order "axial" tensor $\mathrm{axi}_{\mathrm{S}}(\mathsf{A})(\boldsymbol{b} \times \boldsymbol{c}) \;:=\; 2\,(\mathrm{skw}_{\mathrm{S}}(\mathsf{A})\boldsymbol{b})\boldsymbol{c} = (\mathsf{A}\boldsymbol{b})\boldsymbol{c} - (\mathsf{A}\boldsymbol{c})\boldsymbol{b}$ formally analogous to the well-known axial vector. Turning next to field relations, let E Euclidean point space with translation vector space V and $\boldsymbol{u}$ be a differentiable Euclidean vector field. We work with the definition[2] $(\mathrm{curl}\,\boldsymbol{T})^{\mathrm{T}}\boldsymbol{a} \;:=\; \mathrm{curl}(\boldsymbol{T}^{\mathrm{T}}\boldsymbol{a})$ for the curl of a differentiable second-order Euclidean tensor field $\boldsymbol{T}$ as a second-order tensor field. Using this definition, one obtains the identity $(\mathrm{curl}\,\boldsymbol{T})(\boldsymbol{a} \times \boldsymbol{b}) = (\nabla_{\boldsymbol{a}}\boldsymbol{T})\boldsymbol{b} - (\nabla_{\boldsymbol{b}}\boldsymbol{T})\boldsymbol{a}$ for $\mathrm{curl}\,\boldsymbol{T}$ in terms of the Euclidean gradient operator ∇, directional derivative $\nabla_{\boldsymbol{a}}\boldsymbol{T} \;:=\; (\nabla\boldsymbol{T})\boldsymbol{a}$, third-order Euclidean tensor field $\nabla\boldsymbol{T}$. On the basis of these definitions, one obtains in particular the compact form $\mathrm{curl}\,\boldsymbol{T} = \mathrm{axi}_{\mathrm{S}}(\mathrm{skw}_{\mathrm{S}}(\nabla\boldsymbol{T})) = \mathrm{axi}_{\mathrm{S}}(\nabla\boldsymbol{T})$ for the curl of a differentiable second-order tensor field $\boldsymbol{T}$ as a function of its gradient $\nabla\boldsymbol{T}$.

---

[2] This is of course a matter of convention. Indeed, in contrast to this, Cermelli and Gurtin (2001) define $(\mathrm{curl}\,\boldsymbol{T})\boldsymbol{a} := \mathrm{curl}(\boldsymbol{T}^{\mathrm{T}}\boldsymbol{b})$.

2.2 Large-deformation continuum constitutive setting

According to Ashby (1970), dislocations in a crystal can be separated into two different types depending on how they are stored. While statistically-stored dislocation (SSDs) accumulate by trapping each other in a random way, geometrically-necessary dislocations (GNDs) are required to maintain deformation compatibility between all parts of the crystal in the case of non-uniform slip. In this vein, Ashby (1970) derived a relation between the density of GNDs and the gradients of plastic shear. This has been discussed in detail in the context of small deformation in many later works (*e.g.*, Arsenlis and Parks, 1999; Shizawa and Zbib, 1999). The question is, how does this generalize to the large-deformation continuum setting? In the phenomenological large-deformation context, local inelastic deformation is invariably represented by the inelastic part $\boldsymbol{F}_{\mathrm{P}}$ of the usual multiplicative decomposition of the deformation gradient. From this point of view, the extension of crystal plasticity to be considered here should involve the gradient of $\boldsymbol{F}_{\mathrm{P}}$ in some way. In this sense, such extensions of crystal plasticity fall under the continuum rubric of gradient theories. Formulations of crystal plasticity involving a (general) dependence of the free energy on the gradient of the local inelastic deformation can be found in, *e.g.*, Naghdi and Srinivasa (1993, 1994); Le and Stumpf (1996); Gurtin (2000).

To have a first look at the consequences of this for the formulation of constitutive models, consider the simplest case, *i.e.*, ideal isothermal phenomenological gradient inelasticity. To this end, we require some notation and concepts. Let B represent a material body (manifold) and $\boldsymbol{\kappa} : B \to E$ a placement of B into E, *i.e.*, a *global placement*. The image $B_{\boldsymbol{\kappa}} := \boldsymbol{\kappa}[B] \subset E$ of $\boldsymbol{\kappa}$ represents the corresponding configuration of B in E. If $\boldsymbol{\gamma} : B \to E$ is a second such placement, $\boldsymbol{\gamma}_{\boldsymbol{\kappa}} := \boldsymbol{\kappa}_* \boldsymbol{\gamma} = \boldsymbol{\gamma} \circ \boldsymbol{\kappa}^{-1} : B_{\boldsymbol{\kappa}} \to B_{\boldsymbol{\gamma}}$ represents the change of global placement from $\boldsymbol{\kappa}$ to $\boldsymbol{\gamma}$. Alternatively, $\boldsymbol{\gamma}_{\boldsymbol{\kappa}}$ can be interpreted as the *deformation* of $B_{\boldsymbol{\kappa}}$ into $B_{\boldsymbol{\gamma}}$. On this basis, a motion of B with respect to E in some time-interval I can be represented in the form $\boldsymbol{\chi} : I \times B \to E$, where, at each $t \in I$, $\boldsymbol{\chi}_t := \boldsymbol{\chi}(t, \cdot) : B \to B_t$ represents the global placement of B into its current configuration $B_t := \boldsymbol{\chi}_t[B]$ in E. Note that any global placement $\boldsymbol{\kappa}$ induces the representation $\boldsymbol{\zeta}_{\boldsymbol{\kappa}} := \boldsymbol{\kappa}_* \boldsymbol{\zeta} := \boldsymbol{\zeta} \circ \boldsymbol{\kappa}^{-1} : B_{\boldsymbol{\kappa}} \to Z$ of any field $\boldsymbol{\zeta} : B \to Z$ on B taking values in some fixed linear or point space Z. Further, any smooth $\boldsymbol{\kappa}$ induces the form $\nabla^{\boldsymbol{\kappa}} \boldsymbol{\zeta} := \boldsymbol{\kappa}^* \nabla(\boldsymbol{\kappa}_* \boldsymbol{\zeta}) = \nabla(\boldsymbol{\zeta} \circ \boldsymbol{\kappa}^{-1}) \circ \boldsymbol{\kappa}$ of the gradient of $\boldsymbol{\zeta}$ taking values in $\mathrm{Lin}(V, Z)$. For example, $\boldsymbol{\chi}_{\boldsymbol{\kappa}} : I \times B_{\boldsymbol{\kappa}} \to E$ represents the deformation of $B_{\boldsymbol{\kappa}}$ into the current configuration B_t at each $t \in I$. From this, we have in particular the deformation gradient $\boldsymbol{F}_{\boldsymbol{\kappa}}(t, b) := (\nabla^{\boldsymbol{\kappa}} \boldsymbol{\chi})(t, b) \in \mathrm{Lin}^+(V, V)$ relative to $\boldsymbol{\kappa}$.

In this framework, relative to any global placement $\boldsymbol{\kappa}$, the behaviour of a material point $b \in B$ at a given time $t \in I$ is determined in particular by the history of the local deformation represented in terms of the local continuum deformation or deformation gradient $\boldsymbol{F}_{\boldsymbol{\kappa}}(t, b)$, the local inelastic deformation $\boldsymbol{F}_{\mathrm{P}\boldsymbol{\kappa}}(t, b)$, and now $(\nabla^{\boldsymbol{\kappa}} \boldsymbol{F}_{\mathrm{P}\boldsymbol{\kappa}})(t, b)$, all at b relative to $\boldsymbol{\kappa}$. These determine in particular the corresponding extended form

$$\psi = \psi_{\boldsymbol{\kappa}}(\boldsymbol{F}_{\boldsymbol{\kappa}}, \boldsymbol{F}_{\mathrm{P}\boldsymbol{\kappa}}, \nabla^{\boldsymbol{\kappa}} \boldsymbol{F}_{\mathrm{P}\boldsymbol{\kappa}}, b) \tag{2.1}$$

of the free energy density at each $b \in B$, again for arbitrary $\boldsymbol{\kappa}$ determining in particular the first Piola-Kirchhoff stress $\boldsymbol{P}_{\boldsymbol{\kappa}} = \partial_{\boldsymbol{F}_{\boldsymbol{\kappa}}} \psi_{\boldsymbol{\kappa}}$ hyperelastically. Later in this work, we will be considering a number of indirect or direct evolution-field relations for $\boldsymbol{F}_{\mathrm{P}\boldsymbol{\kappa}}$ (which will depend in addition on a dissipation or other potential as well as the free energy, but this is not directly relevant here). In this case, $\boldsymbol{\chi}_{\boldsymbol{\kappa}}$ and this latter field represent the degrees-of-freedom of our continuum.

Consider now the effect of a change of global reference placement on the form of $\psi_{\boldsymbol{\kappa}}$ above. As discussed by Cermelli and Gurtin (2001), this can be alternatively interpreted as the effect of the corresponding compatible (*i.e.*, curl-less) deformation on the form of $\psi_{\boldsymbol{\kappa}}$. Such compatible deformations have been shown (*e.g.*, Davini, 1986; Davini and Parry, 1989) to leave crystallographic dislocation measures unchanged, representing as such "elastic" changes of local reference placement. The idea here is that the form of the free energy and other consitutive relations depending on such measures should then be invariant with respect to such changes of global reference placement, or alternatively, with respect to compatible deformations. One obtains the transformations

$$\begin{aligned} \boldsymbol{F}_{\boldsymbol{\kappa}} &= \boldsymbol{\Lambda}^{*}_{\boldsymbol{\gamma\kappa}} \boldsymbol{F}_{\boldsymbol{\gamma}} \ , \\ \boldsymbol{F}_{\mathrm{P}\boldsymbol{\kappa}} &= \boldsymbol{\Lambda}^{*}_{\boldsymbol{\gamma\kappa}} \boldsymbol{F}_{\mathrm{P}\boldsymbol{\gamma}} \ , \\ \nabla^{\boldsymbol{\kappa}} \boldsymbol{F}_{\mathrm{P}\boldsymbol{\kappa}} &= \boldsymbol{\Lambda}^{*}_{\boldsymbol{\gamma\kappa}} \left[\nabla^{\boldsymbol{\gamma}} \boldsymbol{F}_{\mathrm{P}\boldsymbol{\gamma}} + \boldsymbol{F}_{\mathrm{P}\boldsymbol{\gamma}} \, \boldsymbol{\Lambda}_{\boldsymbol{\gamma\kappa}*} \, (\nabla^{\boldsymbol{\kappa}} \boldsymbol{\Lambda}_{\boldsymbol{\gamma\kappa}}) \right] \ , \\ \psi_{\boldsymbol{\kappa}} &= \det(\boldsymbol{\Lambda}_{\boldsymbol{\gamma\kappa}}) \, \psi_{\boldsymbol{\gamma}} \ , \end{aligned} \tag{2.2}$$

using the above notation, with

$$\boldsymbol{\Lambda}_{\boldsymbol{\gamma\kappa}} := \nabla^{\boldsymbol{\kappa}} \boldsymbol{\gamma} \tag{2.3}$$

and

$$\begin{aligned} \boldsymbol{\Lambda}^{*}_{\boldsymbol{\gamma\kappa}} \boldsymbol{F}_{\boldsymbol{\gamma}} &:= \boldsymbol{F}_{\boldsymbol{\gamma}} \, \boldsymbol{\Lambda}_{\boldsymbol{\gamma\kappa}} \ , \\ ((\boldsymbol{\Lambda}_{\boldsymbol{\gamma\kappa}*}(\nabla^{\boldsymbol{\kappa}} \boldsymbol{\Lambda}_{\boldsymbol{\gamma\kappa}}))\boldsymbol{a})\boldsymbol{b} &:= ((\nabla^{\boldsymbol{\kappa}} \boldsymbol{\Lambda}_{\boldsymbol{\gamma\kappa}}) \boldsymbol{\Lambda}^{-1}_{\boldsymbol{\gamma\kappa}} \boldsymbol{a}) \boldsymbol{\Lambda}^{-1}_{\boldsymbol{\gamma\kappa}} \boldsymbol{b} \ . \end{aligned} \tag{2.4}$$

Substituting these results into (2.1), we obtain

$$\begin{aligned} \psi_{\boldsymbol{\kappa}}(\boldsymbol{F}_{\boldsymbol{\kappa}}, \boldsymbol{F}_{\mathrm{P}\boldsymbol{\kappa}}, \nabla^{\boldsymbol{\kappa}} \boldsymbol{F}_{\mathrm{P}\boldsymbol{\kappa}}, b) &= \det(\boldsymbol{\Lambda}_{\boldsymbol{\gamma\kappa}}) \, \psi_{\boldsymbol{\gamma}}(\boldsymbol{F}_{\boldsymbol{\gamma}}, \boldsymbol{F}_{\mathrm{P}\boldsymbol{\gamma}}, \nabla^{\boldsymbol{\gamma}} \boldsymbol{F}_{\mathrm{P}\boldsymbol{\gamma}} \\ &+ \boldsymbol{F}_{\mathrm{P}\boldsymbol{\gamma}} \, \boldsymbol{\Lambda}_{\boldsymbol{\gamma\kappa}*}(\nabla^{\boldsymbol{\kappa}} \boldsymbol{\Lambda}_{\boldsymbol{\gamma\kappa}}), b) \\ &\neq \det(\boldsymbol{\Lambda}_{\boldsymbol{\gamma\kappa}}) \, \psi_{\boldsymbol{\gamma}}(\boldsymbol{F}_{\boldsymbol{\gamma}}, \boldsymbol{F}_{\mathrm{P}\boldsymbol{\gamma}}, \nabla^{\boldsymbol{\gamma}} \boldsymbol{F}_{\mathrm{P}\boldsymbol{\gamma}}, b) \ . \end{aligned} \tag{2.5}$$

Due to the non-tensorial nature of $\nabla^{\boldsymbol{\kappa}} \boldsymbol{F}_{\mathrm{P}\boldsymbol{\kappa}}$, then, the form (2.1) of $\psi_{\boldsymbol{\kappa}}$ will depend in general on the choice of global reference placement. To examine this result more closely, consider the split

$$\nabla^{\boldsymbol{\kappa}} \boldsymbol{F}_{\mathrm{P}\boldsymbol{\kappa}} = \mathrm{sym}_{\mathrm{S}}(\nabla^{\boldsymbol{\kappa}} \boldsymbol{F}_{\mathrm{P}\boldsymbol{\kappa}}) + \mathrm{skw}_{\mathrm{S}}(\nabla^{\boldsymbol{\kappa}} \boldsymbol{F}_{\mathrm{P}\boldsymbol{\kappa}}) \tag{2.6}$$

of $\nabla^{\boldsymbol{\kappa}} \boldsymbol{F}_{\mathrm{P}\boldsymbol{\kappa}}$ into symmetric and skew-symmetric parts. In particular, the result

$$\mathrm{axi}_{\mathrm{S}}(\nabla^{\boldsymbol{\kappa}} \boldsymbol{F}_{\mathrm{P}\boldsymbol{\kappa}}) = \mathrm{axi}_{\mathrm{S}}(\mathrm{skw}_{\mathrm{S}}(\nabla^{\boldsymbol{\kappa}} \boldsymbol{F}_{\mathrm{P}\boldsymbol{\kappa}})) = \mathrm{curl}^{\boldsymbol{\kappa}} \boldsymbol{F}_{\mathrm{P}\boldsymbol{\kappa}} \tag{2.7}$$

implies that $\mathrm{skw}_{\mathrm{S}}(\nabla^{\boldsymbol{\kappa}} \boldsymbol{F}_{\mathrm{P}\boldsymbol{\kappa}})$ represents the *incompatibility* of $\boldsymbol{F}_{\mathrm{P}\boldsymbol{\kappa}}$ with respect to $\boldsymbol{\kappa}$. Combining $(2.2)_3$ and (2.6), then, one obtains

$$\begin{aligned} \mathrm{sym}_{\mathrm{S}}(\nabla^{\boldsymbol{\kappa}} \boldsymbol{F}_{\mathrm{P}\boldsymbol{\kappa}}) &= \boldsymbol{\Lambda}^{*}_{\boldsymbol{\gamma\kappa}}[\mathrm{sym}_{\mathrm{S}}(\nabla^{\boldsymbol{\gamma}} \boldsymbol{F}_{\mathrm{P}\boldsymbol{\gamma}}) + \boldsymbol{F}_{\mathrm{P}\boldsymbol{\gamma}} \, \boldsymbol{\Lambda}_{\boldsymbol{\gamma\kappa}*}(\nabla^{\boldsymbol{\kappa}} \boldsymbol{\Lambda}_{\boldsymbol{\gamma\kappa}})] \ , \\ \mathrm{skw}_{\mathrm{S}}(\nabla^{\boldsymbol{\kappa}} \boldsymbol{F}_{\mathrm{P}\boldsymbol{\kappa}}) &= \boldsymbol{\Lambda}^{*}_{\boldsymbol{\gamma\kappa}} \, \mathrm{skw}_{\mathrm{S}}(\nabla^{\boldsymbol{\gamma}} \boldsymbol{F}_{\mathrm{P}\boldsymbol{\gamma}}) \ , \end{aligned} \tag{2.8}$$

since $\nabla^{\boldsymbol{\kappa}} \boldsymbol{\Lambda}_{\boldsymbol{\gamma\kappa}} = \nabla^{\boldsymbol{\kappa}}(\nabla^{\boldsymbol{\kappa}} \boldsymbol{\gamma})$ is symmetric. Note that $(2.8)_2$ takes the alternative form

$$\mathrm{curl}^{\boldsymbol{\kappa}} \boldsymbol{F}_{\mathrm{P}\boldsymbol{\kappa}} = \det(\nabla^{\boldsymbol{\kappa}} \boldsymbol{\gamma}) \, (\mathrm{curl}^{\boldsymbol{\gamma}} \boldsymbol{F}_{\mathrm{P}\boldsymbol{\gamma}})(\nabla^{\boldsymbol{\kappa}} \boldsymbol{\gamma})^{-\mathrm{T}} \tag{2.9}$$

in terms of $\mathrm{curl}^{\boldsymbol{\kappa}} \boldsymbol{F}_{\mathrm{P}\boldsymbol{\kappa}}$. So, we see that the dependence of the form of $\psi_{\boldsymbol{\kappa}}$ on the choice of reference placement is due in particular to its dependence on the symmetric part $\mathrm{sym}_{\mathrm{S}}(\nabla^{\boldsymbol{\kappa}} \boldsymbol{F}_{\mathrm{P}\boldsymbol{\kappa}})$ of $\nabla^{\boldsymbol{\kappa}} \boldsymbol{F}_{\mathrm{P}\boldsymbol{\kappa}}$. For special changes of reference placement, *e.g.*, when $\boldsymbol{\gamma}_{\boldsymbol{\kappa}}$ is affine (*i.e.*, $\nabla^{\boldsymbol{\kappa}}(\nabla^{\boldsymbol{\kappa}} \boldsymbol{\gamma})$ vanishes), $\mathrm{sym}_{\mathrm{S}}(\nabla^{\boldsymbol{\kappa}} \boldsymbol{F}_{\mathrm{P}\boldsymbol{\kappa}})$ transforms tensorially as well. More generally, $(2.8)_1$ implies that, if $\boldsymbol{\gamma}$ satisfies the field equation

$$\nabla^{\boldsymbol{\kappa}}(\nabla^{\boldsymbol{\kappa}} \boldsymbol{\gamma}) = \boldsymbol{F}^{-1}_{\mathrm{P}\boldsymbol{\gamma}} \, \mathrm{sym}_{\mathrm{S}}(\nabla^{\boldsymbol{\kappa}} \boldsymbol{F}_{\mathrm{P}\boldsymbol{\kappa}}) \tag{2.10}$$

at each time[3] during the deformation process, $\mathrm{sym}_{\mathrm{S}}(\nabla^{\gamma}\boldsymbol{F}_{\mathrm{P}\gamma})$ vanishes identically, in which case ψ_{γ} as given by (2.1) would depend only on the skew-symmetric part of $\nabla^{\gamma}\boldsymbol{F}_{\mathrm{P}\gamma}$. In general, however, these results shows that, for the form (2.1) of $\psi_{\boldsymbol{\kappa}}$ to be independent of change of global reference placement, or of compatible deformation, in general, it can only depend on the incompatibility $\mathrm{skw}_{\mathrm{S}}(\nabla^{\boldsymbol{\kappa}}\boldsymbol{F}_{\mathrm{P}\boldsymbol{\kappa}})$ of $\boldsymbol{F}_{\mathrm{P}\boldsymbol{\kappa}}$ from the start. This is in agreement with conclusions of Cermelli and Gurtin (2001), who showed in a different fashion that constitutive functions for any $b \in B$ depending on $\nabla^{\boldsymbol{\kappa}}\boldsymbol{F}_{\mathrm{P}\,\boldsymbol{\kappa}}$ must reduce to a dependence on $\mathrm{curl}^{\boldsymbol{\kappa}}\boldsymbol{F}_{\mathrm{P}\boldsymbol{\kappa}}$ alone for their form to be independent of a compatible or “elastic” deformation.

Going now one step further in this context, consider next the generalization of the modeling of $\boldsymbol{F}_{\mathrm{P}\boldsymbol{\kappa}}$ as (deformation-history-dependent) change of *local* reference placement (Svendsen *et al.*, 2001) to gradient inelasticity. In this case, there exists a reduced form $\psi_{\mathrm{i}\boldsymbol{\kappa}}$ of $\psi_{\boldsymbol{\kappa}}$ such that

$$\psi_{\boldsymbol{\kappa}}(\boldsymbol{F}_{\boldsymbol{\kappa}},\boldsymbol{F}_{\mathrm{P}\boldsymbol{\kappa}},\mathrm{skw}_{\mathrm{S}}(\nabla^{\boldsymbol{\kappa}}\boldsymbol{F}_{\mathrm{P}\boldsymbol{\kappa}}),b)=\det(\boldsymbol{F}_{\mathrm{P}\boldsymbol{\kappa}})\,\psi_{\mathrm{i}\boldsymbol{\kappa}}(\boldsymbol{F}_{\mathrm{P}\boldsymbol{\kappa}*}\boldsymbol{F}_{\boldsymbol{\kappa}},\boldsymbol{F}_{\mathrm{P}\boldsymbol{\kappa}*}\,\mathrm{skw}_{\mathrm{S}}(\nabla^{\boldsymbol{\kappa}}\boldsymbol{F}_{\mathrm{P}\boldsymbol{\kappa}}),b) \tag{2.11}$$

holds. Here,

$$\boldsymbol{F}_{\mathrm{P}\boldsymbol{\kappa}*}\boldsymbol{F}_{\boldsymbol{\kappa}}=\boldsymbol{F}_{\boldsymbol{\kappa}}\boldsymbol{F}_{\mathrm{P}\boldsymbol{\kappa}}^{-1}=:\boldsymbol{F}_{\mathrm{E}\boldsymbol{\kappa}} \tag{2.12}$$

represents the local elastic deformation in the material relative to the so-called (local) intermediate (inelastic) configuration, and

$$((\boldsymbol{F}_{\mathrm{P}\boldsymbol{\kappa}*}\nabla^{\boldsymbol{\kappa}}\boldsymbol{F}_{\mathrm{P}\boldsymbol{\kappa}})\boldsymbol{a})\boldsymbol{b}=((\nabla^{\boldsymbol{\kappa}}\boldsymbol{F}_{\mathrm{P}\boldsymbol{\kappa}})\boldsymbol{F}_{\mathrm{P}\boldsymbol{\kappa}}^{-1}\boldsymbol{a})\boldsymbol{F}_{\mathrm{P}\boldsymbol{\kappa}}^{-1}\boldsymbol{b} \tag{2.13}$$

the push-forward of $\nabla^{\boldsymbol{\kappa}}\boldsymbol{F}_{\mathrm{P}\boldsymbol{\kappa}}$ by $\boldsymbol{F}_{\mathrm{P}\boldsymbol{\kappa}}$ to the intermediate configuration. In the standard non-gradient context, such a model for $\boldsymbol{F}_{\mathrm{P}\boldsymbol{\kappa}}$ clearly implies that the usual elastic part $\boldsymbol{F}_{\mathrm{E}}$ of the deformation gradient is the measure of energy storage in the material due to lattice deformation. Noting that $\boldsymbol{F}_{\mathrm{P}\boldsymbol{\kappa}*}\,\mathrm{skw}_{\mathrm{S}}(\nabla^{\boldsymbol{\kappa}}\boldsymbol{F}_{\mathrm{P}\boldsymbol{\kappa}})=\mathrm{skw}_{\mathrm{S}}(\boldsymbol{F}_{\mathrm{P}\boldsymbol{\kappa}*}\,(\nabla^{\boldsymbol{\kappa}}\boldsymbol{F}_{\mathrm{P}\boldsymbol{\kappa}}))$, from (2.2) follows in turn the transformation relations

$$\begin{array}{rcl}\boldsymbol{F}_{\mathrm{E}\boldsymbol{\kappa}} & = & \boldsymbol{F}_{\mathrm{E}\gamma}\;,\\ \mathrm{skw}_{\mathrm{S}}(\boldsymbol{F}_{\mathrm{P}\boldsymbol{\kappa}*}\nabla^{\boldsymbol{\kappa}}\boldsymbol{F}_{\mathrm{P}\boldsymbol{\kappa}}) & = & \mathrm{skw}_{\mathrm{S}}(\boldsymbol{F}_{\mathrm{P}\gamma*}\nabla^{\gamma}\boldsymbol{F}_{\mathrm{P}\gamma})\;.\end{array} \tag{2.14}$$

Substituting these results into (2.11), we obtain analogously $\psi_{\mathrm{i}\boldsymbol{\kappa}}=\psi_{\mathrm{i}\gamma}$, *i.e.*, the form of the free energy density with respect to the intermediated configuration is independent of the choice of global reference placement. In particular, with the help of the result

$$\mathrm{axi}_{\mathrm{S}}(\boldsymbol{F}_{\mathrm{P}\boldsymbol{\kappa}*}\nabla^{\boldsymbol{\kappa}}\boldsymbol{F}_{\mathrm{P}\boldsymbol{\kappa}})=\mathrm{axi}_{\mathrm{S}}(\mathrm{skw}_{\mathrm{S}}(\boldsymbol{F}_{\mathrm{P}\boldsymbol{\kappa}*}\nabla^{\boldsymbol{\kappa}}\boldsymbol{F}_{\mathrm{P}\boldsymbol{\kappa}}))=\det(\boldsymbol{F}_{\mathrm{P}\boldsymbol{\kappa}})^{-1}\,(\mathrm{curl}^{\boldsymbol{\kappa}}\boldsymbol{F}_{\mathrm{P}\boldsymbol{\kappa}})\boldsymbol{F}_{\mathrm{P}\boldsymbol{\kappa}}^{\mathrm{T}}\quad, \tag{2.15}$$

note that the axial form of $\mathrm{skw}_{\mathrm{S}}(\boldsymbol{F}_{\mathrm{P}\boldsymbol{\kappa}*}\nabla^{\boldsymbol{\kappa}}\boldsymbol{F}_{\mathrm{P}\boldsymbol{\kappa}})$ represents the so-called geometric dislocation tensor

$$\boldsymbol{G}_{\mathrm{i}}:=\det(\boldsymbol{F}_{\mathrm{P}\boldsymbol{\kappa}})^{-1}\,(\mathrm{curl}^{\boldsymbol{\kappa}}\boldsymbol{F}_{\mathrm{P}\boldsymbol{\kappa}})\boldsymbol{F}_{\mathrm{P}\boldsymbol{\kappa}}^{\mathrm{T}}=\det(\boldsymbol{F}_{\mathrm{P}\gamma})^{-1}\,(\mathrm{curl}^{\gamma}\boldsymbol{F}_{\mathrm{P}\gamma})\boldsymbol{F}_{\mathrm{P}\gamma}^{\mathrm{T}} \tag{2.16}$$

of Cermelli and Gurtin (2001). As follows from (2.14), and as indicated here, this tensor is independent of the choice of $\boldsymbol{\kappa}$.

In the sequel, attention will be focused on an arbitrary reference configuration $B_{\mathrm{r}}\equiv B_{\boldsymbol{\kappa}}$, the local intermediate one induced by $\boldsymbol{F}_{\mathrm{P}}\equiv\boldsymbol{F}_{\mathrm{P}\boldsymbol{\kappa}}$, and the current one $B_{\mathrm{c}}\equiv B_{t}$. As indicated, for notational simplicity, we now drop the notation $\boldsymbol{\kappa}$ for the reference configuration. Further, use will be made of the notation $\nabla^{\mathrm{r}}\equiv\nabla^{\boldsymbol{\kappa}}$ for the gradient operator relative to the arbitrary reference configuration B_{r}, and that ∇^{c} relative to the current configuration B_{c}, in what follows. Lastly, all forms of the free energy to follow will be consistent with the reduction

$$\begin{array}{rcl}\psi & = & \psi_{\mathrm{r}}(\theta,\boldsymbol{F},\boldsymbol{F}_{\mathrm{P}},\boldsymbol{G}_{\mathrm{r}},\boldsymbol{\epsilon})\\ & = & \det(\boldsymbol{F}_{\mathrm{P}})\,\psi_{\mathrm{i}}(\theta,\boldsymbol{F}_{\mathrm{E}},\boldsymbol{G}_{\mathrm{i}},\boldsymbol{\epsilon})\end{array} \tag{2.17}$$

---

[3] Resulting over the process time interval I in a *time-dependent* or *time-parameterized* change of reference configuration.

independent of compatible deformations and consistent with the modeling of $\boldsymbol{F}_{\text{P}}$ as a material isomorphism as discussed above, with

$$\boldsymbol{G}_{\text{r}} := \text{axi}_{\text{S}}(\text{skw}_{\text{S}}(\nabla^{\text{r}}\boldsymbol{F}_{\text{P}})) = \text{curl}_{\text{r}}\boldsymbol{F}_{\text{P}} \tag{2.18}$$

the referential form of the dislocation density tensor. The class of free energy functions (2.17) considered by Svendsen (2000, 2002), and the isothermal special case of $(2.17)_2$ for plastic incompressibility $\det(\boldsymbol{F}_{\text{P}})$ by Gurtin (2002). Here, we have included a dependence on the temperature θ as well as on a set $\boldsymbol{\epsilon} := (\epsilon_1, \dots, \epsilon_n)$ of *scalar*-valued internal variables (*e.g.*, accumulated inelastic deformation on each glide system) whose development leads to additional energy storage in the material.

2.3 Finite dislocation density and lattice curvature measures

Assuming that the crystalline material in question contains dislocations which can be treated as being "continuously-distributed" in a material point at the continuum or macroscopic level, one can formulate (average) dislocation density and lattice curvature measures with respect to continuum (infinitesimal) line, area and volume elements of the material in question (*e.g.*, Kröner, 1960). This is done here in the context of finite deformation and (later) small elastic strain. As usual, in the phenomenological context, as well as in the case of crystal plasticity, this is based on the multiplicative decomposition

$$\boldsymbol{F} = \boldsymbol{F}_{\text{E}}\boldsymbol{F}_{\text{P}} \tag{2.19}$$

(*e.g.*, Lee, 1969; Mandel, 1971; Rice, 1971) of the deformation gradient into elastic and plastic parts. This is generally completed by the flow rule

$$\dot{\boldsymbol{F}}_{\text{P}} = \boldsymbol{L}_{\text{P}}\boldsymbol{F}_{\text{P}} \quad . \tag{2.20}$$

For example, in the case of single crystals, we have

$$\boldsymbol{L}_{\text{P}} = \sum\nolimits_{\mathfrak{a}} \dot{\gamma}_{\text{a}}\,(\boldsymbol{s}_{\mathfrak{a}} \otimes \boldsymbol{n}_{\mathfrak{a}}) \tag{2.21}$$

the sum being taken over all (active) slip systems as usual. Here, $\boldsymbol{s}_{\mathfrak{a}}$ is the slip direction, $\boldsymbol{n}_{\mathfrak{a}}$ the slip plane normal and $\dot{\gamma}_{\mathfrak{a}}$ the slip rate on the slip system $\mathfrak{a}$. As usual, we interpret $\boldsymbol{F}_{\text{P}}$ as defining the local intermediate configuration which is on average stress-free and as such characterized by zero mean lattice (*i.e.*, elastic) strain. Since $\boldsymbol{F}_{\text{P}}$ is not the gradient of a vector field, the intermediate configuration is in general not compatible. As such, a closed circuit C in the reference configuration is mapped via $\boldsymbol{F}_{\text{P}}$ on one generally open circuit. The closure failure of the circuit, representing the net sum $\boldsymbol{b}(C)$ of the Burgers vectors of all dislocation lines piercing the area S enclosed by the circuit C, is given by

$$\boldsymbol{b}(C) = \oint_C \boldsymbol{F}_{\text{P}}\,d\boldsymbol{x}_{\text{r}} = \int_S (\text{curl}_{\text{r}}\boldsymbol{F}_{\text{P}})\boldsymbol{n}_{\text{r}}\,da_{\text{r}} = \int_S \boldsymbol{G}_{\text{r}}\boldsymbol{n}_{\text{r}}\,da_{\text{r}} \tag{2.22}$$

(Nye, 1953; Bilby *et al.*, 1955; Kröner, 1960; Landau and Lifshitz, 1970) via Stoke's theorem, *i.e.*, assuming no jumps in $\boldsymbol{F}_{\text{P}}$. As such, $\boldsymbol{G}_{\text{r}}\boldsymbol{n}_{\text{r}}$ represents the corresponding vectorial surface density of GND lines piercing the referential surface element $\boldsymbol{n}_{\text{r}}\,da_{\text{r}}$ and $\text{curl}_{\text{r}}\boldsymbol{F}_{\text{P}}$. The vanishing of $\boldsymbol{b}(C)$ implies that there are no excess dislocations around C, such that the material experiences no net bending around this circuit. Noting the analogy of (2.18) with the expression $\boldsymbol{b} = \operatorname{curl} \boldsymbol{a}$ for the magnetic field (or more precisely, flux density) $\boldsymbol{b}$ as the curl of the vector potential $\boldsymbol{a}$, one could perhaps refer to $\boldsymbol{F}_{\mathrm{P}}$ as the potential for the dislocation (density) "field" $\boldsymbol{G}_{\mathrm{r}}$. On this basis, the conservation of dislocation (field) lines in the material is given by

$$\operatorname{div}_{\mathrm{r}} \boldsymbol{G}_{\mathrm{r}} = \boldsymbol{0} \quad , \tag{2.23}$$

a relation formally analogous to Faraday's law for conservation of magnetic flux. Like $\boldsymbol{F}_{\mathrm{P}}$ itself, $\boldsymbol{G}_{\mathrm{r}}$ represents a mixed (*i.e.*, intermediate-referential) second-order tensor field. On the other hand, the related measure

$$\boldsymbol{G}_{\mathrm{i}} := \det(\boldsymbol{F}_{\mathrm{P}}^{-1})\,(\operatorname{curl}_{\mathrm{r}} \boldsymbol{F}_{\mathrm{P}}) \boldsymbol{F}_{\mathrm{P}}^{\mathrm{T}} = \det(\boldsymbol{F}_{\mathrm{P}}^{-1})\, \boldsymbol{G}_{\mathrm{r}} \boldsymbol{F}_{\mathrm{P}}^{\mathrm{T}} \quad , \tag{2.24}$$

representing the dislocation density tensor of Cermelli and Gurtin (2001), is purely intermediate in character. Indeed, with the help of the standard area-element transformation $\boldsymbol{n}_{\mathrm{i}}\, da_{\mathrm{i}} = \det(\boldsymbol{F}_{\mathrm{P}})\, \boldsymbol{F}_{\mathrm{P}}^{-\mathrm{T}}\, \boldsymbol{n}_{\mathrm{r}}\, da_{\mathrm{r}}$ induced by $\boldsymbol{F}_{\mathrm{P}}$, one obtains

$$\boldsymbol{G}_{\mathrm{i}} \boldsymbol{n}_{\mathrm{i}}\, da_{\mathrm{i}} = \boldsymbol{G}_{\mathrm{r}} \boldsymbol{n}_{\mathrm{r}}\, da_{\mathrm{r}} \quad . \tag{2.25}$$

$\boldsymbol{G}_{\mathrm{i}}$ can also be expressed in terms of $\boldsymbol{F}_{\mathrm{E}}$ as

$$\boldsymbol{G}_{\mathrm{i}} = \det(\boldsymbol{F}_{\mathrm{E}})\,(\operatorname{curl}_{\mathrm{c}} \boldsymbol{F}_{\mathrm{E}}^{-1})\, \boldsymbol{F}_{\mathrm{E}}^{-\mathrm{T}} = -\boldsymbol{F}_{\mathrm{E}}^{-1}\,(\operatorname{curl}_{\mathrm{i}} \boldsymbol{F}_{\mathrm{E}}) \tag{2.26}$$

via the compatibility of $\boldsymbol{F}$. Note that the curl operator $\operatorname{curl}_{\mathrm{i}}$ is defined relative to the intermediate configuration via $\nabla^{\mathrm{i}} \boldsymbol{\zeta} := (\nabla^{\mathrm{r}} \boldsymbol{\zeta}) \boldsymbol{F}_{\mathrm{P}}^{-1}$. Lastly,

$$\boldsymbol{G}_{\mathrm{c}} := \operatorname{curl}_{\mathrm{c}} \boldsymbol{F}_{\mathrm{E}}^{-1} = \det(\boldsymbol{F}^{-1})\, \boldsymbol{G}_{\mathrm{r}} \boldsymbol{F}^{\mathrm{T}} = \det(\boldsymbol{F}_{\mathrm{E}}^{-1})\, \boldsymbol{G}_{\mathrm{i}} \boldsymbol{F}_{\mathrm{E}}^{\mathrm{T}} \tag{2.27}$$

represents the dislocation density tensor with respect to the current configuration, with $\operatorname{curl}_{\mathrm{c}}$ the corresponding curl operator based on ∇^{c}. More generally, this last result follows from the symmetry of $\nabla^{\mathrm{r}} \boldsymbol{F}$ as

$$\begin{aligned}
\boldsymbol{G}_{\mathrm{i}}(\boldsymbol{a} \times \boldsymbol{b}) &= (\operatorname{curl}_{\mathrm{r}} \boldsymbol{F}_{\mathrm{P}})(\boldsymbol{F}_{\mathrm{P}}^{-1} \boldsymbol{a} \times \boldsymbol{F}_{\mathrm{P}}^{-1} \boldsymbol{b}) \\
&= (\nabla^{\mathrm{i}}_{\boldsymbol{a}} \boldsymbol{F}_{\mathrm{P}}) \boldsymbol{F}_{\mathrm{P}}^{-1} \boldsymbol{b} - (\nabla^{\mathrm{i}}_{\boldsymbol{b}} \boldsymbol{F}_{\mathrm{P}}) \boldsymbol{F}_{\mathrm{P}}^{-1} \boldsymbol{a} \\
&= (\nabla^{\mathrm{c}}_{\boldsymbol{F}_{\mathrm{E}} \boldsymbol{a}} \boldsymbol{F}_{\mathrm{E}}^{-1}) \boldsymbol{F}_{\mathrm{E}} \boldsymbol{b} - (\nabla^{\mathrm{c}}_{\boldsymbol{F}_{\mathrm{E}} \boldsymbol{b}} \boldsymbol{F}_{\mathrm{E}}^{-1}) \boldsymbol{F}_{\mathrm{E}} \boldsymbol{a} \\
&= \boldsymbol{F}_{\mathrm{E}}^{-1} \{ (\nabla^{\mathrm{i}}_{\boldsymbol{b}} \boldsymbol{F}_{\mathrm{E}}) \boldsymbol{a} - (\nabla^{\mathrm{i}}_{\boldsymbol{a}} \boldsymbol{F}_{\mathrm{E}}) \boldsymbol{b} \}
\end{aligned} \tag{2.28}$$

via the definition of the curl of a second-order tensor field being used here. Analogous to (2.23), we have

$$\operatorname{div}_{\mathrm{c}} \boldsymbol{G}_{\mathrm{c}} = \boldsymbol{0} \tag{2.29}$$

for the conservation of dislocation lines relative to the current configuration.

To take into account the effect of the motion of dislocations on the state of deformation in the material, consider next the evolution relations arising for the dislocation density tensors above on the basis of the relation (2.20) for the (negative of the) "dislocation flux density" $\dot{\boldsymbol{F}}_{\mathrm{P}}$. We have

$$\begin{aligned}
\dot{\boldsymbol{G}}_{\mathrm{r}} &= \operatorname{curl}_{\mathrm{r}}(\boldsymbol{L}_{\mathrm{P}} \boldsymbol{F}_{\mathrm{P}}) \,, \\
\dot{\boldsymbol{G}}_{\mathrm{i}} &= \boldsymbol{G}_{\mathrm{i}} \boldsymbol{L}_{\mathrm{P}}^{\mathrm{T}} - (\boldsymbol{I} \cdot \boldsymbol{L}_{\mathrm{P}}) \boldsymbol{G}_{\mathrm{i}} + \det(\boldsymbol{F}_{\mathrm{P}}^{-1}) \{ \operatorname{curl}_{\mathrm{r}}(\boldsymbol{L}_{\mathrm{P}} \boldsymbol{F}_{\mathrm{P}}) \} \boldsymbol{F}_{\mathrm{P}}^{\mathrm{T}} \,, \\
\dot{\boldsymbol{G}}_{\mathrm{c}} &= \boldsymbol{G}_{\mathrm{c}} \boldsymbol{L}^{\mathrm{T}} - (\boldsymbol{I} \cdot \boldsymbol{L})\, \boldsymbol{G}_{\mathrm{c}} + \operatorname{curl}_{\mathrm{c}}(\boldsymbol{L}_{\mathrm{P}} \boldsymbol{F}_{\mathrm{E}}^{-1}) \,,
\end{aligned} \tag{2.30}$$

from (2.20) and the above definitions. Note that

$$\begin{aligned} \mathrm{curl}_{\mathrm{r}}(\boldsymbol{L}_{\mathrm{P}}\boldsymbol{F}_{\mathrm{P}}) &= \boldsymbol{L}_{\mathrm{P}}\boldsymbol{G}_{\mathrm{r}} + \det(\boldsymbol{F}_{\mathrm{P}})(\mathrm{curl}_{\mathrm{i}}\boldsymbol{L}_{\mathrm{P}})\boldsymbol{F}_{\mathrm{P}}^{-\mathrm{T}} \, , \\ \det(\boldsymbol{F}_{\mathrm{P}}^{-1})\{\mathrm{curl}_{\mathrm{r}}(\boldsymbol{L}_{\mathrm{P}}\boldsymbol{F}_{\mathrm{P}})\}\boldsymbol{F}_{\mathrm{P}}^{\mathrm{T}} &= \boldsymbol{L}_{\mathrm{P}}\boldsymbol{G}_{\mathrm{i}} + \mathrm{curl}_{\mathrm{i}}\boldsymbol{L}_{\mathrm{P}} \, , \\ \mathrm{curl}_{\mathrm{c}}(\boldsymbol{L}_{\mathrm{P}}\boldsymbol{F}_{\mathrm{E}}^{-1}) &= \boldsymbol{L}_{\mathrm{P}}\boldsymbol{G}_{\mathrm{c}} + \det(\boldsymbol{F}_{\mathrm{E}}^{-1})(\mathrm{curl}_{\mathrm{i}}\boldsymbol{L}_{\mathrm{P}})\boldsymbol{F}_{\mathrm{E}}^{\mathrm{T}} \, . \end{aligned} \tag{2.31}$$

In particular, in the case of crystal plasticity, $\boldsymbol{I} \cdot \boldsymbol{L}_{\mathrm{P}} = 0$ and $\det(\boldsymbol{F}_{\mathrm{P}}) = 1$. More generally, in the incremental context, the “non-locality” of these dislocation density measures is expressed in terms of the incompatibility of $\boldsymbol{L}_{\mathrm{P}}$ with respect to the intermediate configuration. In the case of crystal plasticity, for example, we have

$$\begin{aligned} \det(\boldsymbol{F}_{\mathrm{P}})(\mathrm{curl}_{\mathrm{i}}\boldsymbol{L}_{\mathrm{P}})\boldsymbol{F}_{\mathrm{P}}^{-\mathrm{T}} &= \sum\nolimits_{\mathfrak{a}} \boldsymbol{s}_{\mathfrak{a}} \otimes (\nabla^{\mathrm{r}}\dot{\gamma}_{\mathfrak{a}} \times \boldsymbol{F}_{\mathrm{P}}^{\mathrm{T}}\boldsymbol{n}_{\mathfrak{a}}) \, , \\ \mathrm{curl}_{\mathrm{i}}\boldsymbol{L}_{\mathrm{P}} &= \sum\nolimits_{\mathfrak{a}} \boldsymbol{s}_{\mathfrak{a}} \otimes (\nabla^{\mathrm{i}}\dot{\gamma}_{\mathfrak{a}} \times \boldsymbol{n}_{\mathfrak{a}}) \, , \end{aligned} \tag{2.32}$$

via (2.21). This crystal plastic form for the incompatibility of $\boldsymbol{L}_{\mathrm{P}}$ displays clearly the dependence of the evolution of the dislocation density measures on that projection of the inhomogeneity $\nabla^{\mathrm{i}}\dot{\gamma}_{\mathfrak{a}}$ of $\dot{\gamma}_{\mathfrak{a}}$ with respect to the intermediate configuration onto the glide plane. Alternatively, in the crystal-plastic context, $\boldsymbol{G}_{\mathrm{r}}$ can be expressed in the finite form

$$\boldsymbol{G}_{\mathrm{r}} = \boldsymbol{G}_{\mathrm{r}0} + b\sum\nolimits_{\mathfrak{a}} \boldsymbol{s}_{\mathfrak{a}} \otimes \boldsymbol{g}_{\mathrm{r}\mathfrak{a}} \tag{2.33}$$

(Svendsen, 2000, 2002) in terms of its initial value $\boldsymbol{G}_{\mathrm{r}0}$ and the glide-system-based vector-valued GND measure $\boldsymbol{g}_{\mathrm{r}\mathfrak{a}}$ with evolution relation

$$\begin{aligned} \dot{\boldsymbol{g}}_{\mathrm{r}\mathfrak{a}} &= b^{-1}\,\mathrm{curl}_{\mathrm{r}}(\dot{\gamma}_{\mathfrak{a}}\boldsymbol{F}_{\mathrm{P}}^{\mathrm{T}}\boldsymbol{n}_{\mathfrak{a}}) \\ &= b^{-1}\,\nabla^{\mathrm{r}}\dot{\gamma}_{\mathfrak{a}} \times \boldsymbol{F}_{\mathrm{P}}^{\mathrm{T}}\boldsymbol{n}_{\mathfrak{a}} + \dot{\gamma}_{\mathfrak{a}}\left\{\boldsymbol{G}_{\mathrm{r}0} + \sum\nolimits_{\mathfrak{b}\neq\mathfrak{a}} \boldsymbol{s}_{\mathfrak{b}} \otimes \boldsymbol{g}_{\mathrm{r}\mathfrak{b}}\right\}^{\mathrm{T}} \boldsymbol{n}_{\mathfrak{a}} \, . \end{aligned} \tag{2.34}$$

In the hardening context, the first two terms contribute to self-hardening, and the last term to latent hardening. In particular, $\boldsymbol{G}_{\mathrm{r}0}$ is due to orientation mismatch at grain boundaries and results is an initial lengthscale-dependent yield stress (*e.g.*, due to geometric necessary boundaries: Evers *et al.*, 2004). Note that $\mathrm{div}_{\mathrm{r}}\boldsymbol{G}_{\mathrm{r}0} = \boldsymbol{0}$ and $\mathrm{div}_{\mathrm{r}}\boldsymbol{g}_{\mathrm{r}\mathfrak{a}} = 0$ for each $\mathfrak{a}$ follow from (2.23).

As has been discussed in detail in many works (*e.g.*, Ashby, 1970; Arsenlis and Parks, 1999), simple geometrical considerations imply that GNDs of edge and screw type cause lattice bending and warping, respectively. In his pioneering work, Nye (1953) introduced the small-deformation dislocation density tensor

$$\boldsymbol{\alpha} \equiv \mathrm{curl}\,\boldsymbol{H}_{\mathrm{E}} = \mathrm{curl}(\mathrm{sym}(\boldsymbol{H}_{\mathrm{E}})) + \mathrm{curl}(\mathrm{skw}(\boldsymbol{H}_{\mathrm{E}})) \tag{2.35}$$

in terms of the local lattice distortion $\boldsymbol{H}_{\mathrm{E}}$ and linked it to the corresponding small-deformation lattice curvature $\boldsymbol{\kappa} \equiv \nabla\,\mathrm{axs}(\boldsymbol{H}_{\mathrm{E}})$ (see also Kafadar and Eringen, 1971; Forest *et al.*, 1997). More generally, consider the case of small elastic strain, *i.e.*,

$$\begin{aligned} \boldsymbol{U}_{\mathrm{E}} &\approx \boldsymbol{I} + \ln\boldsymbol{U}_{\mathrm{E}} \, , \\ \boldsymbol{F}_{\mathrm{E}} &\approx \boldsymbol{R}_{\mathrm{E}} \, , \end{aligned} \tag{2.36}$$

with $\boldsymbol{R}_{\mathrm{E}}$ the mean rotation of the crystal lattice from the polar decomposition

$$\boldsymbol{F}_{\mathrm{E}} = \boldsymbol{R}_{\mathrm{E}}\boldsymbol{U}_{\mathrm{E}} \tag{2.37}$$

of $\boldsymbol{F}_{\mathrm{E}}$, and $\boldsymbol{U}_{\mathrm{E}}$ the mean stretching of the lattice. In this case, we have the split

$$\boldsymbol{F}_{\mathrm{E}}^{-1}(\nabla_{\boldsymbol{a}}^{\mathrm{i}}\boldsymbol{F}_{\mathrm{E}}) \approx \boldsymbol{R}_{\mathrm{E}}^{\mathrm{T}}(\nabla_{\boldsymbol{a}}^{\mathrm{i}}\boldsymbol{R}_{\mathrm{E}}) + \nabla_{\boldsymbol{a}}^{\mathrm{i}}\ln\boldsymbol{U}_{\mathrm{E}} \tag{2.38}$$

of $\boldsymbol{F}_{\mathrm{E}}^{-1}(\nabla_{\boldsymbol{a}}^{\mathrm{i}}\boldsymbol{F}_{\mathrm{E}})$ into parts determined by the inhomogeneity of the lattice rotation $\boldsymbol{R}_{\mathrm{E}}$ and by that of the lattice distortion $\ln\boldsymbol{U}_{\mathrm{E}}$. In particular, the former is related to the third-order lattice curvature tensor $\mathcal{K}_{\mathrm{i}}$ defined by

$$\mathcal{K}_{\mathrm{i}}\boldsymbol{a} := (\nabla_{\boldsymbol{a}}^{\mathrm{i}}\boldsymbol{R}_{\mathrm{E}}^{\mathrm{T}})\boldsymbol{R}_{\mathrm{E}} = -\boldsymbol{R}_{\mathrm{E}}^{\mathrm{T}}(\nabla_{\boldsymbol{a}}^{\mathrm{i}}\boldsymbol{R}_{\mathrm{E}}) \tag{2.39}$$

for all vectors $\boldsymbol{a}$. Note that, from (2.28) and (2.38), one obtains the expression

$$\begin{aligned}(\mathcal{K}_{\mathrm{i}}\boldsymbol{a})\boldsymbol{b} &= \tfrac{1}{2}\{[(\mathcal{S}_{\mathrm{i}}\boldsymbol{a}) - (\mathcal{S}_{\mathrm{i}}\boldsymbol{a})^{\mathrm{T}}]\boldsymbol{b} - (\mathcal{S}_{\mathrm{i}}\boldsymbol{b})^{\mathrm{T}}\boldsymbol{a}\} \\ &+ \tfrac{1}{2}\{[(\mathcal{A}_{\mathrm{i}}\boldsymbol{a}) - (\mathcal{A}_{\mathrm{i}}\boldsymbol{a})^{\mathrm{T}}]\boldsymbol{b} - (\mathcal{A}_{\mathrm{i}}\boldsymbol{b})^{\mathrm{T}}\boldsymbol{a}\}\end{aligned} \tag{2.40}$$

for this tensor in terms of those

$$\begin{aligned}(\mathcal{S}_{\mathrm{i}}\boldsymbol{a})\boldsymbol{b} &:= \boldsymbol{F}_{\mathrm{E}}^{-1}\{(\nabla_{\boldsymbol{b}}^{\mathrm{i}}\boldsymbol{F}_{\mathrm{E}})\boldsymbol{a} - (\nabla_{\boldsymbol{a}}^{\mathrm{i}}\boldsymbol{F}_{\mathrm{E}})\boldsymbol{b}\} &&= \boldsymbol{G}_{\mathrm{i}}(\boldsymbol{a}\times\boldsymbol{b})\ , \\ (\mathcal{A}_{\mathrm{i}}\boldsymbol{a})\boldsymbol{b} &:= (\nabla_{\boldsymbol{a}}^{\mathrm{i}}\ln\boldsymbol{U}_{\mathrm{E}})\boldsymbol{b} - (\nabla_{\boldsymbol{b}}^{\mathrm{i}}\ln\boldsymbol{U}_{\mathrm{E}})\boldsymbol{a} &&= \mathrm{curl}_{\mathrm{i}}(\ln\boldsymbol{U}_{\mathrm{E}})(\boldsymbol{a}\times\boldsymbol{b})\ ,\end{aligned} \tag{2.41}$$

determined by $\boldsymbol{G}_{\mathrm{i}}$ and the incompatibility $\mathrm{curl}_{\mathrm{i}}(\ln\boldsymbol{U}_{\mathrm{E}})$ of the lattice strain $\ln\boldsymbol{U}_{\mathrm{E}}$ with respect to the intermediate configuration. Consequently, lattice curvature results in general from both this latter incompatibility and GND development. In particular, if $\ln\boldsymbol{U}_{\mathrm{E}}$ is in fact compatible, the lattice curvature is directly related to $\boldsymbol{G}_{\mathrm{i}}$. Since it can be experimentally determined (at least for fcc systems), *e.g.*, with the help of electron back-scattering diffraction and orientation imaging microscopy (*e.g.*, Sun *et al.*, 1998; El-Dasher *et al.*, 2003), lattice curvature offers at least in principle the possibility to compare theoretical predictions of $\boldsymbol{G}_{\mathrm{i}}$ and its development with experimental results via relations such as (2.41).

2.4 Standard-continuum-based extensions of crystal plasticity

Among the proposed approaches on how to incorporate the effects of GNDs into the hardening modeling, the simplest simply accounts for GND density in otherwise "conventional" hardening modeling, resulting in the retention of the standard continuum setting. Consider for example the approach of Dai and Parks (1997), which has been used by, *e.g.*, Busso *et al.* (2000) to model the additional hardening in two-phase nickel super-alloys. In their approach, $\boldsymbol{G}_{\mathrm{r}} = \mathrm{curl}_{\mathrm{r}}\boldsymbol{F}_{\mathrm{P}}$ is considered as the generalization of Nye's dislocation density tensor to large deformation. In particular, Dai and Parks (1997) assumed that a given slip system consists of three dislocation families: a set of screw dislocation with the tangent vector in the direction $\boldsymbol{s}_{\mathfrak{a}}$, a set of edge dislocation with the tangent vector in the direction $\boldsymbol{t}_{\mathfrak{a}} = \boldsymbol{s}_{\mathfrak{a}} \times \boldsymbol{n}_{\mathfrak{a}}$, and a set of edge dislocation with the tangent vector in the direction $\boldsymbol{s}_{\mathfrak{a}}$. The Burgers vector of all 3 types lies in the direction $\boldsymbol{s}_{\mathfrak{a}}$. The corresponding densities $\rho_{\mathfrak{a}}^{G(s)}$, $\rho_{\mathfrak{a}}^{G(e)1}$ and $\rho_{\mathfrak{a}}^{G(e)2}$ are assumed to be fully determined by

$$b(\dot{\rho}_{\mathfrak{a}}^{G(s)}\boldsymbol{s}_{\mathfrak{a}} + \dot{\rho}_{\mathfrak{a}}^{G(e)1}\boldsymbol{t}_{\mathfrak{a}} + \dot{\rho}_{\mathfrak{a}}^{G(e)2}\boldsymbol{n}_{\mathfrak{a}}) \equiv \mathrm{curl}_{\mathrm{r}}(\dot{\gamma}_{\mathfrak{a}}\boldsymbol{F}_{\mathrm{P}}^{\mathrm{T}}\boldsymbol{n}_{\mathfrak{a}}) \tag{2.42}$$

In the context of (2.33) and (2.34), we see that this is equal to $b\,\dot{\boldsymbol{g}}_{\mathrm{r}\mathfrak{a}}$, where again b represents the magnitude of the Burgers vector. The total GND density on slip system $\mathfrak{a}$ is then

$$\rho_{\mathfrak{a}}^{G} = \left|\rho_{\mathfrak{a}}^{G(s)}\right| + \left|\rho_{\mathfrak{a}}^{G(e)1}\right| + \left|\rho_{\mathfrak{a}}^{G(e)2}\right| \quad . \tag{2.43}$$

This field of GNDs can act as obstacles to the motion of any glissile dislocation in the same way as statistically-stored dislocations do, and so produce enhanced hardening. The effective slip-system resistance $s_{\mathfrak{a}}^{G}$ resulting from GNDs is evaluated as

$$s_{\mathfrak{a}}^{G} = c\mu b\sqrt{\sum\nolimits_{\mathfrak{b}} a_{\mathfrak{a}\mathfrak{b}}\rho_{\mathfrak{b}}^{G}} \quad . \tag{2.44}$$

with $a_{\mathfrak{a}\mathfrak{b}}$ characterizing the $\mathfrak{a} - \mathfrak{b}$ dislocation interaction strength (Franciosi and Zaoui, 1982). With the slip system resistance due to SSDs $s_{\mathfrak{a}}^{S}$ the overall glide resistance $s_{\mathfrak{a}}$ on the slip system $\mathfrak{a}$ is taken to depend on both according to

$$s_{\mathfrak{a}} = \left[(s_{\mathfrak{a}}^{G})^{k} + (s_{\mathfrak{a}}^{S})^{k}\right]^{1/k} \quad , \tag{2.45}$$

where k is taken as a positive constant $k = 1$ or $k = 2$. Note the slight formal inconsistency here. On the one hand, the slip system resistance due to SSDs $s_{\mathfrak{a}}^{S}$ is obtained from the slip system shears $\gamma_{\mathfrak{a}}$, which are intermediate-configuration quantities. On the other hand, $s_{\mathfrak{a}}^{G}$ is evaluated using the "slip system GNDs" $\rho_{\mathfrak{a}}^{G}$ from (2.43) as based on $\mathrm{curl}_{\mathrm{r}}(\dot{\gamma}_{\mathfrak{a}}\boldsymbol{F}_{\mathrm{P}}^{\mathrm{T}}\boldsymbol{n}_{\mathfrak{a}})$, which are mixed intermediate-referential quantities.

Let us consider a FCC single crystal with its 12 slip systems. The slip planes are of the type $\{111\}$ and slip directions of $\langle 110\rangle$. We examine now the situation where two slip systems with the same slip directions are loaded symmetrically so that the inelastic shear rates on the both are equal. In this case, the time derivative of the plastic deformation can be written as

$$\dot{\boldsymbol{F}}_{\mathrm{P}} = (\dot{\gamma}\boldsymbol{s}\otimes\boldsymbol{n}_{1} + \dot{\gamma}\boldsymbol{s}\otimes\boldsymbol{n}_{2})\,\boldsymbol{F}_{\mathrm{P}} = \dot{\gamma}(\boldsymbol{s}\otimes\boldsymbol{n})\boldsymbol{F}_{\mathrm{P}} \tag{2.46}$$

with $\boldsymbol{n} = \boldsymbol{n}_{1}+\boldsymbol{n}_{2}$. Since both $\boldsymbol{n}_{1}$ and $\boldsymbol{n}_{1}$ are orthogonal to $\boldsymbol{s}$ the vector $\boldsymbol{n}$ is as well. Furthermore, if we assume that there is no plastic deformation at the beginning, then $\boldsymbol{F}_{\mathrm{P}}$ is initially equal to the identity, and (2.46) can be integrated to yield

$$\boldsymbol{F}_{\mathrm{P}} = \boldsymbol{I} + \gamma\boldsymbol{s}\otimes\boldsymbol{n} \quad . \tag{2.47}$$

From this, one obtains

$$\boldsymbol{G}_{\mathrm{r}} = \mathrm{curl}_{\mathrm{r}}(\gamma\boldsymbol{s}\otimes\boldsymbol{n}) = \boldsymbol{s}\otimes(\nabla^{\mathrm{r}}\gamma\times\boldsymbol{n}) \quad , \tag{2.48}$$

since $\boldsymbol{s}$ and $\boldsymbol{n}$ are constant. Further, (2.23) is satisfied identically. Assuming next that γ varies only in the direction $\boldsymbol{n}$, *i.e.*, that $\nabla^{\mathrm{r}}\gamma \parallel \boldsymbol{n}$, (2.48) implies that $\boldsymbol{G}_{\mathrm{r}}$ vanishes identically, in which case $\boldsymbol{F}_{\mathrm{P}}$ is compatible. This situation arises for example in plane strain, where two symmetrically loaded slip systems with the same slip direction result in a glide band whose slip direction is the same as of the both slip systems and whose normal points into the direction of the bisector of the normals of the both slip systems.

Let us now use the formula (2.42) to determine the GND density on the both active slip systems 1 and 2 in the sense of Dai and Parks (1997). With $\mathfrak{a}$ taking the values 1 or 2, we obtain

$$\mathrm{curl}_{\mathrm{r}}(\dot{\gamma}_{\mathfrak{a}}\boldsymbol{F}_{\mathrm{P}}^{\mathrm{T}}\boldsymbol{n}_{\mathfrak{a}}) = (\nabla^{\mathrm{r}}\dot{\gamma}\cdot\boldsymbol{n})\,\boldsymbol{n}\times\boldsymbol{n}_{\mathfrak{a}} = -(\nabla^{\mathrm{r}}\dot{\gamma}\cdot\boldsymbol{n})(\boldsymbol{n}\cdot\boldsymbol{t}_{\mathfrak{a}})\boldsymbol{s} = (\nabla^{\mathrm{r}}\dot{\gamma}\cdot\boldsymbol{n})\,a_{\mathfrak{a}}\,\boldsymbol{s} \quad , \tag{2.49}$$

where $a_{\mathfrak{a}} := -\boldsymbol{n}\cdot\boldsymbol{t}_{\mathfrak{a}}$. Since $\boldsymbol{n} = \boldsymbol{n}_{1} + \boldsymbol{n}_{2}$, we have $a_{1} = -a_{2} = a$. Comparing then (2.42) and (2.49), we conclude

$$\dot{\rho}_{1}^{G(s)} = -\dot{\rho}_{2}^{G(s)} = \frac{a}{b}\,\nabla^{\mathrm{r}}\dot{\gamma}\cdot\boldsymbol{n} \neq 0 \quad . \tag{2.50}$$

Consequently, in this model, we have the same number of screw dislocations on system 2 as on system 1 with the same Burgers vector but opposite sign. So, this approach results in the presence of GNDs leading via (2.43) and (2.44) to additional slip system resistance although the plastic deformation is compatible! This shortcoming stems from the fact that screw dislocations with the same Burgers vector but gliding on different slip planes are treated here as different dislocations although screw dislocations are characterized by their Burgers vector alone, regardless of the slip plane. Indeed, if such dislocations have the same Burgers vector, they should be combined together in order to evaluate the net resulting polarity.

In the approach of Dai and Parks (1997), only the first spatial derivatives of the plastic deformation enters the constitutive equations via the dependence of the slip resistance on the ”crystallographic GND densities” $\rho_\mathfrak{a}^G$ whose evolution is given by the history of the slips via the equations (2.43) and (2.43). Thus, only the constitutive form of the slip resistance is influenced by the presence of GNDs, other constitutive equations retain their form. This and the fact that no additional boundary conditions are needed in this case makes this approach very attractive for engineering applications. Admittedly, that in this theory, as was shown above, a compatible plastic deformation, which implies no GNDs, can lead to additional hardening. Consequently, the quantities $\rho_\mathfrak{a}^G$ are not solely GND-related, and the nature of this additional hardening is questionable. Analogous approaches in which the standard boundary-value problem and the form of the constitutive equations are retained include Acharya and Bassani (2000) and Acharya *et al.* (2003). This they achieve by introducing additional GND hardening via a dependence of the hardening moduli on a particular GND measure. Like the approach of Dai and Parks (1997), their approach is non-thermodynamic and presumes the GND hardening process is purely dissipative in nature, *i.e.*, leads to no energy storage. In particular, Acharya and Bassani (2000) utilized a frame-invariant GND density measure which is essentially equivalent to the small-elastic-strain form of $\boldsymbol{G}_\mathrm{i}$ and takes into account short-range interactions between GNDs and mobile dislocations which arise when the GNDs intersect the slip plane of the mobile dislocations. Since from (2.22) and (2.25) we know that $\boldsymbol{G}_\mathrm{i}\boldsymbol{n}_\mathrm{i}$ represents the surface density of excess dislocations threading the surface element $\boldsymbol{n}_\mathrm{i}\, da_\mathrm{i}$, the corresponding scalar density for the slip plane $\mathfrak{a}$ is given by

$$\lambda_\mathfrak{a} = |\boldsymbol{G}_\mathrm{i}\boldsymbol{n}_\mathfrak{a}| \tag{2.51}$$

with $\boldsymbol{n}_\mathfrak{a}$ being the plane normal of the slip system $\mathfrak{a}$. These GND forest measures can than be used alongside with the slips in the evolution of the critical shear stress $\tau_\mathfrak{a}^{Cr} = \sum_\mathfrak{b} h_{\mathfrak{a}\mathfrak{b}}\dot{\gamma}_\mathfrak{a}$ via the dependence of the hardening moduli $h_{\mathfrak{a}\mathfrak{b}}(\gamma_\mathfrak{a}, \lambda_\mathfrak{a})$ on their values. In contrast to Dai and Parks (1997), the GND measure $\lambda_\mathfrak{a}$, used in Acharya and Bassani (2000) vanishes in the case of compatible elastic and plastic deformation and so results in no additional hardening.

2.5 Continuum thermodynamic extension of crystal plasticity

The extensions of crystal plasticity discussed in the previous section were all characterized by the retention of the standard continuum setting and boundary-value problem. They reflect the fact that the buildup of excess dislocations in the material results in a dependence of the the material (*i.e.*, hardening) behaviour on the history of the *gradient* of the local inelastic deformation. Otherwise, they treat the local inelastic deformation as a “standard” internal variable whose spatial variability is derived “directly” from the deformation field itself. Such an approach clearly does not account *directly* for the influence of internal boundaries (*e.g.*, grain or phase boundaries) and the microstructure in general on GND development. More general continuum-mechanics-based approaches of this nature for crystal plasticity have been developed in a thermodynamic context for large deformation by, *e.g.*, Menzel and Steinmann (2000); Svendsen (2000); Gurtin (2000); Svendsen (2002); Gurtin (2002) and in a non-thermodynamic setting by Evers *et al.* (2004). In this section, we pursue a generalization of the approach of Svendsen (2000, 2002). As in all other continuum-thermodynamic-based approaches, the essential physical assumption here is that additional GND-based hardening results in additional energy storage in the material. That this aspect of GND-based material behaviour can be accounted for without extending ψ_{r} to depend on measures such as $\boldsymbol{G}_{\mathrm{r}}$ has been shown in the very elegant continuum thermodynamic phenomenological approach of Acharya (2004).

For simplicity, the formulation here is restricted here to the supply-free case. As shown by Šilhavý (1997), under mild additional assumptions (*e.g.*, local solvability), the Coleman-Noll dissipation principle is applicable to the supply-free case. In any case, from a physical point of view, momentum, energy and entropy supplies should be negligible in the curren context of crystal plasticity. On this basis, the local energy balance takes the form

$$\dot{e} = \mathrm{div}_{\mathrm{r}}\boldsymbol{h} \tag{2.52}$$

in referential form. Here, $e = \varepsilon + k$ represents the referential total energy density, ε the corresponding internal energy density, k the corresponding kinetic energy density, and $\boldsymbol{h}$ the corresponding energy-flux density. The analogous form of entropy balance is given by

$$\dot{\eta} = \pi - \mathrm{div}_{\mathrm{r}}\boldsymbol{\phi} \quad , \tag{2.53}$$

with η the entropy density, $\boldsymbol{\phi}$ the entropy flux density, and π the (non-negative) entropy production-rate density. Multiplying (2.53) by the absolute temperature θ and combining the result with the energy balance (2.52), one obtains

$$\delta = \mathrm{div}_{\mathrm{r}}\boldsymbol{f} - \dot{\psi} - \dot{\boldsymbol{m}}\cdot\dot{\boldsymbol{\chi}} - \boldsymbol{\phi}\cdot\nabla^{\mathrm{r}}\theta - \eta\,\dot{\theta} \tag{2.54}$$

for the dissipation rate density $\delta := \theta\pi$ in terms of

$$\begin{array}{rcl} \psi & := & \varepsilon - \theta\eta\,, \\ \boldsymbol{f} & := & \boldsymbol{h} + \theta\boldsymbol{\phi}\,, \\ \dot{k} & := & \dot{\boldsymbol{m}}\cdot\dot{\boldsymbol{\chi}}\,, \end{array} \tag{2.55}$$

with $\boldsymbol{m}$ the momentum density. Since π is restricted to be nonnegative, and θ is by definition, the entropy principle (now in terms of the dissipation) requires δ to be as well. On this basis, consider now the class of thermoelastic, viscoplastic behaviour as based in particular on the form (2.17) of the free energy density depending in particular on the dislocation density tensor $\boldsymbol{G}_{\mathrm{r}}$ from (2.18). From this, one has

$$\begin{array}{rcl} \dot{\psi} & = & \partial_{\theta}\psi_{\mathrm{r}}\,\dot{\theta} + \partial_{\boldsymbol{F}}\psi_{\mathrm{r}}\cdot\dot{\boldsymbol{F}} + \partial_{\boldsymbol{F}_{\mathrm{P}}}\psi_{\mathrm{r}}\cdot\dot{\boldsymbol{F}}_{\mathrm{P}} + \partial_{\boldsymbol{\epsilon}}\psi_{\mathrm{r}}\cdot\dot{\boldsymbol{\epsilon}} + \partial_{\boldsymbol{G}_{\mathrm{r}}}\psi_{\mathrm{r}}\cdot\dot{\boldsymbol{G}}_{\mathrm{r}} \\ & = & (\partial_{\theta}\psi_{\mathrm{r}})\,\dot{\theta} - \mathrm{div}_{\mathrm{r}}(\partial_{\boldsymbol{F}}\psi_{\mathrm{r}})\cdot\dot{\boldsymbol{\chi}} \\ & + & \{\partial_{\boldsymbol{F}_{\mathrm{P}}}\psi_{\mathrm{r}} + \mathrm{curl}_{\mathrm{r}}(\partial_{\boldsymbol{G}_{\mathrm{r}}}\psi_{\mathrm{r}})\}\cdot\dot{\boldsymbol{F}}_{\mathrm{P}} + \partial_{\boldsymbol{\epsilon}}\psi_{\mathrm{r}}\cdot\dot{\boldsymbol{\epsilon}} \\ & + & \mathrm{div}_{\mathrm{r}}\{(\partial_{\boldsymbol{F}}\psi_{\mathrm{r}})^{\mathrm{T}}\dot{\boldsymbol{\chi}} + 2\ \mathrm{axs}[(\partial_{\boldsymbol{G}_{\mathrm{r}}}\psi_{\mathrm{r}})^{\mathrm{T}}\dot{\boldsymbol{F}}_{\mathrm{P}}]\} \end{array} \tag{2.56}$$

for the material time derivative of ψ via the identity $\mathrm{curl}\boldsymbol{A}\cdot\boldsymbol{B} = \boldsymbol{A}\cdot\mathrm{curl}\boldsymbol{B} + \mathrm{div}[2\ \mathrm{axs}(\boldsymbol{A}^{\mathrm{T}}\boldsymbol{B})]$. Substituting (2.56) into (2.54), we obtain

$$\begin{array}{rcl} \delta & = & \{\mathrm{div}_{\mathrm{r}}(\partial_{\boldsymbol{F}}\psi_{\mathrm{r}}) - \dot{\boldsymbol{m}}\}\cdot\dot{\boldsymbol{\chi}} - (\eta + \partial_{\theta}\psi_{\mathrm{r}})\,\dot{\theta} \\ & + & \boldsymbol{\Sigma}_{\mathrm{r}}\cdot\dot{\boldsymbol{F}}_{\mathrm{P}} - \partial_{\boldsymbol{\epsilon}}\psi_{\mathrm{r}}\cdot\dot{\boldsymbol{\epsilon}} - \boldsymbol{\phi}\cdot\nabla^{\mathrm{r}}\theta\,, \end{array} \tag{2.57}$$

via the constitutive assumption

$$\boldsymbol{f} = (\partial_{\boldsymbol{F}}\psi_{\mathrm{r}})^{\mathrm{T}}\dot{\boldsymbol{\chi}} + 2\ \mathrm{axs}\{(\partial_{\boldsymbol{G}_{\mathrm{r}}}\psi_{\mathrm{r}})^{\mathrm{T}}\dot{\boldsymbol{F}}_{\mathrm{P}}\} \tag{2.58}$$

for the energy flux density, with

$$\boldsymbol{\Sigma}_{\mathrm{r}} := -\{\partial_{\boldsymbol{F}_{\mathrm{P}}}\psi_{\mathrm{r}} + \mathrm{curl}_{\mathrm{r}}(\partial_{\boldsymbol{G}_{\mathrm{r}}}\psi_{\mathrm{r}})\} \tag{2.59}$$

the generalized thermodynamic force driving the evolution of $\dot{\boldsymbol{F}}_{\mathrm{P}}$. In what follows, we also work with the form

$$\boldsymbol{\Sigma}_{\mathrm{i}} := \boldsymbol{\Sigma}_{\mathrm{r}}\boldsymbol{F}_{\mathrm{P}}^{\mathrm{T}} \tag{2.60}$$

of $\boldsymbol{\Sigma}_{\mathrm{r}}$ in the intermediate configuration conjugate to $\boldsymbol{L}_{\mathrm{P}}$. In particular, the thermodynamic force $\boldsymbol{\Sigma}_{\mathrm{i}}$ is related to the internal stresses resulting from lattice distortion, bending, and warping, the latter two due to the presence of GNDs.

Consider next the dissipation principle (*e.g.*, Šilhavý, 1997) in the context of (2.57). This requires δ to remain nonnegative for all admissible thermodynamic processes. Assuming in particular that $\boldsymbol{f}$, $\boldsymbol{\phi}$, η, and the evolution relations for the internal variables are independent of $\dot{\boldsymbol{\chi}}$ and $\dot{\theta}$, note that δ is linear in these. Necessary for the fulfillment of $\delta \geqslant 0$ in this case is the vanishing of the corresponding coefficients, yielding the linear momentum balance

$$\dot{\boldsymbol{m}} = \mathrm{div}_{\mathrm{r}}(\partial_{\boldsymbol{F}}\psi_{\mathrm{r}}) \tag{2.61}$$

and the thermoelastic form

$$\eta = -\partial_{\theta}\psi_{\mathrm{r}} \quad , \tag{2.62}$$

for the entropy density. These reduce the dissipation-rate density to its so-called residual form

$$\delta = \boldsymbol{\Sigma}_{\mathrm{r}} \cdot \dot{\boldsymbol{F}}_{\mathrm{P}} - \partial_{\boldsymbol{\epsilon}}\psi_{\mathrm{r}} \cdot \dot{\boldsymbol{\epsilon}} - \boldsymbol{\phi} \cdot \nabla^{\mathrm{r}}\theta = \boldsymbol{\Sigma}_{\mathrm{i}} \cdot \boldsymbol{L}_{\mathrm{P}} - \partial_{\boldsymbol{\epsilon}}\psi_{\mathrm{r}} \cdot \dot{\boldsymbol{\epsilon}} - \boldsymbol{\phi} \cdot \nabla^{\mathrm{r}}\theta \quad . \tag{2.63}$$

In terms of the dissipation potential

$$d = d_{\mathrm{r}}(\theta, \boldsymbol{F}, \boldsymbol{F}_{\mathrm{P}}, \boldsymbol{G}_{\mathrm{r}}, \boldsymbol{\varsigma}, \dot{\boldsymbol{F}}_{\mathrm{P}}, \dot{\boldsymbol{\epsilon}}, \nabla^{\mathrm{r}}\theta) = d_{\mathrm{i}}(\theta, \boldsymbol{F}_{\mathrm{E}}, \boldsymbol{G}_{\mathrm{i}}, \boldsymbol{\varsigma}, \boldsymbol{L}_{\mathrm{P}}, \dot{\boldsymbol{\epsilon}}, \nabla^{\mathrm{i}}\theta) \tag{2.64}$$

and corresponding sufficient constitutive forms[4]

$$\begin{array}{rcl} \boldsymbol{\Sigma}_{\mathrm{r}} & = & \partial_{\dot{\boldsymbol{F}}_{\mathrm{P}}} d_{\mathrm{r}}\ , \\ -\partial_{\boldsymbol{\epsilon}}\psi_{\mathrm{r}} & = & \partial_{\dot{\boldsymbol{\epsilon}}} d_{\mathrm{r}}\ , \\ -\boldsymbol{\phi} & = & \partial_{\nabla^{\mathrm{r}}\theta} d_{\mathrm{r}}\ , \end{array} \tag{2.65}$$

(2.63) reduces further to

$$\delta = (\partial_{\dot{\boldsymbol{F}}_{\mathrm{P}}} d_{\mathrm{r}}) \cdot \dot{\boldsymbol{F}}_{\mathrm{P}} + (\partial_{\dot{\boldsymbol{\epsilon}}} d_{\mathrm{r}}) \cdot \dot{\boldsymbol{\epsilon}} + (\partial_{\nabla^{\mathrm{r}}\theta} d_{\mathrm{r}}) \cdot \nabla^{\mathrm{r}}\theta \geqslant d_{\mathrm{r}} \geqslant 0 \tag{2.66}$$

The latter conditions hold here since χ is by definition non-negative and convex in the "non-equilibrium" quantities $\dot{\boldsymbol{F}}_{\mathrm{P}}$, $\dot{\boldsymbol{\epsilon}}$ and $\nabla^{\mathrm{r}}\theta$. In (2.64), note that $\boldsymbol{\varsigma} = (\varsigma_1, \ldots)$ represents a set of internal variables associated with dynamic, *i.e.*, dissipative, hardening processes. Combination of (2.62) with the entropy balance (2.52) and this last result yields the field relation

$$c\,\dot{\theta} = \varpi + \mathrm{div}_{\mathrm{r}}[\theta\,(\partial_{\nabla^{\mathrm{r}}\theta} d_{\mathrm{r}})] \tag{2.67}$$

---

[4] In case of non-differentiability at zero, the partial derivatives here should be interpreted as subdifferentials.

for the temperature, with $c := -\theta\,(\partial_\theta\partial_\theta\psi_{\rm r})$, and

$$\begin{array}{rcl} \varpi & := & \theta\,(\partial_\theta\partial_{\boldsymbol{F}}\psi_{\rm r})\cdot\dot{\boldsymbol{F}} + \{\partial_{\dot{\boldsymbol{F}}_{\rm P}} d_{\rm r} + \theta\,(\partial_\theta\partial_{\boldsymbol{F}_{\rm P}}\psi_{\rm r})\}\cdot\dot{\boldsymbol{F}}_{\rm P} \\ & + & \{\partial_{\dot{\boldsymbol{\epsilon}}} d_{\rm r} + \theta\,(\partial_\theta\partial_{\boldsymbol{\epsilon}}\psi_{\rm r})\}\cdot\dot{\boldsymbol{\epsilon}} + \theta\,(\partial_\theta\partial_{\boldsymbol{G}_{\rm r}}\psi_{\rm r})\cdot\dot{\boldsymbol{G}}_{\rm r} \end{array} \tag{2.68}$$

the rate of mechanical heating.

In summary, on the basis of the above results, one obtains the momentum balance (2.61) for the deformation field $\boldsymbol{\chi}$, (2.67) for the temperature field θ, as well as that

$$\boldsymbol{0} = \partial_{\dot{\boldsymbol{F}}_{\rm P}} d_{\rm r} + \partial_{\boldsymbol{F}_{\rm P}}\psi_{\rm r} + {\rm curl}_{\rm r}(\partial_{{\rm curl}_{\rm r}\boldsymbol{F}_{\rm P}}\psi_{\rm r}) \tag{2.69}$$

for $\boldsymbol{F}_{\rm P}$ from $(2.65)_1$ via (2.18) and (2.59). All of these are determined by the forms of $\psi_{\rm r}$ and $d_{\rm r}$ as given above. For the formulation of initial-boundary-value problems and numerical implementation, the corresponding weak forms

$$\begin{array}{rcccl} \displaystyle\int_{B_r}\dot{\boldsymbol{m}}\cdot\dot{\boldsymbol{\chi}}_\star & + & \displaystyle\int_{B_r}(\partial_{\boldsymbol{F}}\psi_{\rm r})\cdot\nabla^{\rm r}\boldsymbol{\chi}_\star & = & \displaystyle\int_{\partial B_r}\boldsymbol{t}\cdot\boldsymbol{\chi}_\star\,, \\ \displaystyle\int_{B_r}(c\,\dot{\theta}-\varpi)\,\theta_\star & + & \displaystyle\int_{B_r}\theta\,(\partial_{\nabla^{\rm r}\theta}d_{\rm r})\cdot\nabla^{\rm r}\theta_\star & = & \displaystyle\int_{\partial B_r}q\,\theta_\star\,, \\ \displaystyle\int_{B_r}(\partial_{\dot{\boldsymbol{F}}_{\rm P}}d_{\rm r}+\partial_{\boldsymbol{F}_{\rm P}}\psi_{\rm r})\cdot\boldsymbol{F}_{{\rm P}\star} & + & \displaystyle\int_{B_r}(\partial_{{\rm curl}_{\rm r}\boldsymbol{F}_{\rm P}}\psi_{\rm r})\cdot{\rm curl}_{\rm r}\boldsymbol{F}_{{\rm P}\star} & = & \displaystyle\int_{\partial B_r}\boldsymbol{\Phi}\cdot\boldsymbol{F}_{{\rm P}\star}\,, \end{array} \tag{2.70}$$

with respect to arbitrary test $\boldsymbol{F}_{{\rm P}\star}$ and corresponding flux $\boldsymbol{\Phi}$ fields mutually exclusive on ∂B_r. As discussed in Svendsen (2000, 2002), in applications, $\boldsymbol{F}_{\rm P}$ is "specified" everywhere including ∂B_r (*i.e.*, via solution of the local flow rule on ∂B_r), in which case $\boldsymbol{\Phi}$ vanishes identically. At the phenomenological level, this would be the basic result of the current formulation, leading to a structured continuum characterized by the fields $(\boldsymbol{\chi},\theta,\boldsymbol{F}_{\rm P})$, where $\boldsymbol{F}_{\rm P}$ represents *in general* nine additional inelastic degrees-of-freedom . Analogous to the case of active and passive glide-systems in the case of crystal plasticity, however, in applications, these additional degrees-of-freedom would not necessarily all be active everywhere in the structure at all times.

The dependence of the referential free energy density on $\boldsymbol{G}_{\rm r}$ results in particular in the back-stress-like contribution ${\rm curl}_{\rm r}(\partial_{\boldsymbol{G}_{\rm r}}\psi_{\rm r})$ to $\boldsymbol{\Sigma}_{\rm i}$ from the incompatibility of $\partial_{\boldsymbol{G}_{\rm r}}\psi_{\rm r}$. Note that this stress is in general non-symmetric. The form (2.60) of $\boldsymbol{\Sigma}_{\rm i}$ implies as well that additional contributions from $\boldsymbol{G}_{\rm r}$ to $\boldsymbol{\Sigma}_{\rm i}$ may also be supplied by the other term $\partial_{\boldsymbol{F}_{\rm P}}\psi_{\rm r}$ if $\boldsymbol{F}_{\rm P}$ and $\boldsymbol{G}_{\rm r}$ are coupled in $\psi_{\rm r}$ (which in general will be the case). Consider in particular the form $(2.17)_2$ of $\psi_{\rm r}$ obtained when one models $\boldsymbol{F}_{\rm P}$ phenomenologically as a history-dependent change of local reference placement. Assuming plastic incompressibility $\det(\boldsymbol{F}_{\rm P}) = 1$, this yields the form

$$\boldsymbol{\Sigma}_{\rm i} = \boldsymbol{M} - \boldsymbol{X} \tag{2.71}$$

for $\boldsymbol{\Sigma}_{\rm i}$ from (2.59) and (2.60) in terms of the Mandel stress

$$\boldsymbol{M} := \boldsymbol{F}_{\rm E}^{\rm T}(\partial_{\boldsymbol{F}_{\rm E}}\psi_{\rm i}) \tag{2.72}$$

and the back stress

$$\boldsymbol{X} := 2\ {\rm sym}(\partial_{\boldsymbol{G}_{\rm i}}\psi_{\rm i})\boldsymbol{G}_{\rm i} + {\rm curl}_{\rm i}(\partial_{\boldsymbol{G}_{\rm i}}\psi_{\rm i}) \quad . \tag{2.73}$$

Likewise, one obtains the form

$$\boldsymbol{f} = \boldsymbol{F}_{\rm P}^{-1}(\partial_{\boldsymbol{F}_{\rm E}}\psi_{\rm i})^{\rm T}\dot{\boldsymbol{\chi}} + 2\ {\rm axs}\{\boldsymbol{F}_{\rm P}^{\rm T}(\partial_{\boldsymbol{G}_{\rm i}}\psi_{\rm i})^{\rm T}\dot{\boldsymbol{F}}_{\rm P}\} \tag{2.74}$$

for the energy flux $\boldsymbol{f}$ from (2.58). The form (2.71) for $\boldsymbol{\Sigma}_{\mathrm{i}}$ implies that, even if $\boldsymbol{G}_{\mathrm{i}}$ were compatible *with respect to the intermediate configuration*, a non-trivial dependence of ψ_{i} on $\boldsymbol{G}_{\mathrm{i}}$ will lead to additional hardening in the material. In any case, these example make it clear that, from a phenomenological point of view, in the large-deformation context, the modeling of the effect of GND development on the hardening behaviour is configuration-dependent.

Next, we embed the above formulation into crystal plasticity. In the current large-deformation non-linear continuum thermodynamic framework, perhaps the most "straightforward" approach in this regard is Svendsen (2000, 2002). Rather than proceeding as above, he exploited the Euclidean frame-indifference of the energy balance together with the dissipation principle to derive basic field relations such as (2.61) or (2.69). To begin, consider the evolution relations

$$\begin{aligned} \dot{\boldsymbol{F}}_{\mathrm{P}} &= \sum\nolimits_{\mathfrak{a}} (\boldsymbol{s}_{\mathfrak{a}} \otimes \boldsymbol{F}_{\mathrm{P}}^{\mathrm{T}} \boldsymbol{n}_{\mathfrak{a}})\, \dot{\gamma}_{\mathfrak{a}} \,, \\ \dot{\boldsymbol{G}}_{\mathrm{r}} &= \sum\nolimits_{\mathfrak{a}} (\boldsymbol{s}_{\mathfrak{a}} \otimes \boldsymbol{G}_{\mathrm{r}}^{\mathrm{T}} \boldsymbol{n}_{\mathfrak{a}})\, \dot{\gamma}_{\mathfrak{a}} + \sum\nolimits_{\mathfrak{a}} \{\boldsymbol{s}_{\mathfrak{a}} \otimes (\boldsymbol{I} \times \boldsymbol{F}_{\mathrm{P}}^{\mathrm{T}} \boldsymbol{n}_{\mathfrak{a}})\} \nabla^{\mathrm{r}} \dot{\gamma}_{\mathfrak{a}} \,, \end{aligned} \tag{2.75}$$

from (2.20)–(2.21) and (2.30)–(2.32) for $\boldsymbol{F}_{\mathrm{P}}$ and $\boldsymbol{G}_{\mathrm{r}}$, respectively. For simplicity, to these we add the general crystal-plastic form

$$\dot{\epsilon}_{\mathfrak{a}} = \sum\nolimits_{\mathfrak{b}} k_{\mathfrak{a}\mathfrak{b}}\, |\dot{\gamma}_{\mathfrak{b}}| = \sum\nolimits_{\mathfrak{b}} k_{\mathfrak{a}\mathfrak{b}}\, \mathrm{sgn}(\dot{\gamma}_{\mathfrak{b}})\, \dot{\gamma}_{\mathfrak{b}} \tag{2.76}$$

for the evolution of each non-dimensional SSD-based measure $\dot{\epsilon}_{\mathfrak{a}}$ of hardening, with $k_{\mathfrak{a}\mathfrak{b}}$ the corresponding quasi-static hardening modulus matrix, assumed symmetric. The key observation here is that these last three relations can be expressed in the general form

$$\dot{\boldsymbol{\alpha}} = \mathsf{K}[\dot{\boldsymbol{\gamma}}] + \mathcal{J}[\nabla^{\mathrm{r}} \dot{\boldsymbol{\gamma}}] \tag{2.77}$$

quasi-linear in the glide-system slip rates $\dot{\boldsymbol{\gamma}} = (\dot{\gamma}_1, \ldots,)$ and their gradients $\nabla^{\mathrm{r}} \dot{\boldsymbol{\gamma}}$, with $\boldsymbol{\alpha} := (\boldsymbol{F}_{\mathrm{P}}, \boldsymbol{G}_{\mathrm{r}}, \boldsymbol{\epsilon})$. Here, K and $\mathcal{J}$ represent constitutive quantities which may depend in particular on $\boldsymbol{\alpha}$. In terms of the corresponding form

$$\psi = \psi_{\mathrm{r}}(\theta, \nabla^{\mathrm{r}} \boldsymbol{\chi}, \boldsymbol{F}_{\mathrm{P}}, \boldsymbol{G}_{\mathrm{r}}, \boldsymbol{\epsilon}) \tag{2.78}$$

for ψ_{r} (writing now $\boldsymbol{F} = \nabla^{\mathrm{r}} \boldsymbol{\chi}$), we then have

$$\dot{\psi} = (\partial_{\dot{\theta}} \dot{\psi}_{\mathrm{r}})\, \dot{\theta} + \partial_{\nabla^{\mathrm{r}} \dot{\boldsymbol{\chi}}} \dot{\psi}_{\mathrm{r}} \cdot \nabla^{\mathrm{r}} \dot{\boldsymbol{\chi}} + \sum\nolimits_{\mathfrak{a}} \partial_{\dot{\gamma}_{\mathfrak{a}}} \dot{\psi}_{\mathrm{r}}\, \dot{\boldsymbol{\gamma}} + \sum\nolimits_{\mathfrak{a}} \partial_{\nabla^{\mathrm{r}} \dot{\gamma}_{\mathfrak{a}}} \dot{\psi}_{\mathrm{r}} \cdot \nabla^{\mathrm{r}} \dot{\gamma}_{\mathfrak{a}} \tag{2.79}$$

for the rate of energy storage in the material, with

$$\begin{aligned} \partial_{\dot{\theta}} \dot{\psi}_{\mathrm{r}} &= \partial_{\theta} \psi_{\mathrm{r}} \,, \\ \partial_{\nabla^{\mathrm{r}} \dot{\boldsymbol{\chi}}} \dot{\psi}_{\mathrm{r}} &= \partial_{\nabla^{\mathrm{r}} \boldsymbol{\chi}} \psi_{\mathrm{r}} \,, \\ \partial_{\dot{\gamma}_{\mathfrak{a}}} \dot{\psi}_{\mathrm{r}} &= \boldsymbol{s}_{\mathfrak{a}} \cdot \{(\partial_{\boldsymbol{F}_{\mathrm{P}}} \psi_{\mathrm{r}}) \boldsymbol{F}_{\mathrm{P}}^{\mathrm{T}} + (\partial_{\boldsymbol{G}_{\mathrm{r}}} \psi_{\mathrm{r}}) \boldsymbol{G}_{\mathrm{r}}^{\mathrm{T}}\} \boldsymbol{n}_{\mathfrak{a}} + \sum\nolimits_{\mathfrak{b}} k_{\mathfrak{a}\mathfrak{b}}\, (\partial_{\epsilon_{\mathfrak{b}}} \psi_{\mathrm{r}})\, \mathrm{sgn}(\dot{\gamma}_{\mathfrak{b}}) \,, \\ \partial_{\nabla^{\mathrm{r}} \dot{\gamma}_{\mathfrak{a}}} \dot{\psi}_{\mathrm{r}} &= \boldsymbol{F}_{\mathrm{P}}^{\mathrm{T}} \boldsymbol{n}_{\mathfrak{a}} \times (\partial_{\boldsymbol{G}_{\mathrm{r}}} \psi_{\mathrm{r}})^{\mathrm{T}} \boldsymbol{s}_{\mathfrak{a}} \,, \end{aligned} \tag{2.80}$$

via (2.77) and (2.78). The corresponding form

$$d = d_{\mathrm{r}}(\theta, \nabla^{\mathrm{r}} \boldsymbol{\chi}, \boldsymbol{F}_{\mathrm{P}}, \boldsymbol{G}_{\mathrm{r}}, \varsigma, \dot{\boldsymbol{\gamma}}, \nabla^{\mathrm{r}} \theta) \tag{2.81}$$

of the dissipation potential determines as before the residual form

$$\delta = (\partial_{\dot{\boldsymbol{\gamma}}} d_{\mathrm{r}}) \cdot \dot{\boldsymbol{\gamma}} + (\partial_{\nabla^{\mathrm{r}} \theta} d_{\mathrm{r}}) \cdot \nabla^{\mathrm{r}} \theta \geqslant d_{\mathrm{r}} \geqslant 0 \tag{2.82}$$

analogous to (2.66). Again, by definition, d_{r} is convex in its non-equilibrium arguments and vanishes in equilibrium. Using these results, then, the non-local flow rule (2.69) for $\boldsymbol{F}_{\mathrm{P}}$ is in effect projected onto the glide-system-level Ginzburg-Landau/Cahn-Allen phase-field form

$$\partial_{\dot{\gamma}_{\mathfrak{a}}} d_{\mathrm{r}} = \mathrm{div}_{\mathrm{r}}(\partial_{\nabla^{\mathrm{r}}\dot{\gamma}_{\mathfrak{a}}} \dot{\psi}_{\mathrm{r}}) - \partial_{\dot{\gamma}_{\mathfrak{a}}} \dot{\psi}_{\mathrm{r}} \tag{2.83}$$

for each $\gamma_{\mathfrak{a}}$. Using the result

$$\mathrm{div}_{\mathrm{r}}(\partial_{\nabla^{\mathrm{r}}\dot{\gamma}_{\mathfrak{a}}} \dot{\psi}_{\mathrm{r}}) = \boldsymbol{s}_{\mathfrak{a}} \cdot \{(\partial_{\boldsymbol{G}_{\mathrm{r}}} \psi_{\mathrm{r}}) \boldsymbol{G}_{\mathrm{r}}^{\mathrm{T}} - \mathrm{curl}_{\mathrm{r}}(\partial_{\boldsymbol{G}_{\mathrm{r}}} \psi_{\mathrm{r}}) \boldsymbol{F}_{\mathrm{P}}^{\mathrm{T}}\} \boldsymbol{n}_{\mathfrak{a}} \quad , \tag{2.84}$$

this relation can be expressed in the more familiar form

$$\begin{aligned} \partial_{\dot{\gamma}_{\mathfrak{a}}} d_{\mathrm{r}} &= \mathrm{div}_{\mathrm{r}}(\partial_{\nabla^{\mathrm{r}}\dot{\gamma}_{\mathfrak{a}}} \dot{\psi}_{\mathrm{r}}) - \partial_{\dot{\gamma}_{\mathfrak{a}}} \dot{\psi}_{\mathrm{r}} \ , \\ &= -\boldsymbol{s}_{\mathfrak{a}} \cdot \{\partial_{\boldsymbol{F}_{\mathrm{P}}} \psi_{\mathrm{r}} + \mathrm{curl}_{\mathrm{r}}(\partial_{\boldsymbol{G}_{\mathrm{r}}} \psi_{\mathrm{r}})\} \boldsymbol{F}_{\mathrm{P}}^{\mathrm{T}} \boldsymbol{n}_{\mathfrak{a}} - \sum\nolimits_{\mathfrak{b}} k_{\mathfrak{a}\mathfrak{b}} \, (\partial_{\epsilon_{\mathfrak{b}}} \psi_{\mathrm{r}}) \ \mathrm{sgn}(\dot{\gamma}_{\mathfrak{b}}) \ , \\ &= \tau_{\mathfrak{a}} - x_{\mathfrak{a}} - \sum\nolimits_{\mathfrak{b}} k_{\mathfrak{a}\mathfrak{b}} \, (\partial_{\epsilon_{\mathfrak{b}}} \psi_{\mathrm{r}}) \ \mathrm{sgn}(\dot{\gamma}_{\mathfrak{b}}) \ , \end{aligned} \tag{2.85}$$

from (2.71)–(2.73) in terms of the glide-system Schmid

$$\tau_{\mathfrak{a}} = \boldsymbol{s}_{\mathfrak{a}} \cdot \boldsymbol{M} \boldsymbol{n}_{\mathfrak{a}} = \boldsymbol{s}_{\mathfrak{a}} \cdot \boldsymbol{F}_{\mathrm{E}}^{\mathrm{T}} (\partial_{\boldsymbol{F}_{\mathrm{E}}} \psi_{\mathrm{i}}) \boldsymbol{n}_{\mathfrak{a}} \tag{2.86}$$

and back

$$x_{\mathfrak{a}} := \boldsymbol{s}_{\mathfrak{a}} \cdot \boldsymbol{X} \boldsymbol{n}_{\mathfrak{a}} = \boldsymbol{s}_{\mathfrak{a}} \cdot \{2 \ \mathrm{sym}(\partial_{\boldsymbol{G}_{\mathrm{i}}} \psi_{\mathrm{i}}) \boldsymbol{G}_{\mathrm{i}} + \mathrm{curl}_{\mathrm{i}}(\partial_{\boldsymbol{G}_{\mathrm{i}}} \psi_{\mathrm{i}})\} \boldsymbol{n}_{\mathfrak{a}} \tag{2.87}$$

stresses, respectively. In the context of crystal plasticity, then, the phenomenological system (2.70) is replaced by that

$$\begin{array}{rcrcl} \displaystyle\int_{B_r} \dot{\boldsymbol{m}} \cdot \dot{\boldsymbol{\chi}}_\star & + & \displaystyle\int_{B_r} (\partial_{\boldsymbol{F}} \psi_{\mathrm{r}}) \cdot \nabla^{\mathrm{r}} \boldsymbol{\chi}_\star & = & \displaystyle\int_{\partial B_r} \boldsymbol{t} \cdot \boldsymbol{\chi}_\star \ , \\ \displaystyle\int_{B_r} (c\,\dot{\theta} - \varpi)\, \theta_\star & + & \displaystyle\int_{B_r} \theta \, (\partial_{\nabla^{\mathrm{r}}\theta} d_{\mathrm{r}}) \cdot \nabla^{\mathrm{r}} \theta_\star & = & \displaystyle\int_{\partial B_r} q \ \theta_\star \ , \\ \displaystyle\int_{B_r} \{\partial_{\dot{\boldsymbol{\gamma}}} d_{\mathrm{r}} + \partial_{\dot{\boldsymbol{\gamma}}} \dot{\psi}_{\mathrm{r}}\} \cdot \boldsymbol{\gamma}_\star & + & \displaystyle\int_{B_r} \partial_{\nabla^{\mathrm{r}}\dot{\boldsymbol{\gamma}}} \dot{\psi}_{\mathrm{r}} \cdot \nabla^{\mathrm{r}} \boldsymbol{\gamma}_\star & = & \displaystyle\int_{\partial B_r} \boldsymbol{\varphi} \cdot \boldsymbol{\gamma}_\star \ , \end{array} \tag{2.88}$$

in terms of the test field array $\boldsymbol{\gamma}_\star = (\gamma_{1\star}, \ldots)$ and corresponding normal boundary flux array $\boldsymbol{\varphi} = (\phi_1, \ldots)$. These are coupled to the evolution relations (2.75) for $\boldsymbol{F}_{\mathrm{P}}$ and $\boldsymbol{G}_{\mathrm{r}}$, respectively, as well as that (2.76) for $\dot{\epsilon}_{\mathfrak{a}}$. As such, $\boldsymbol{G}_{\mathrm{r}}$, like $\boldsymbol{F}_{\mathrm{P}}$, is treated as a "standard" internal variable, and each $\gamma_{\mathfrak{a}} \in \boldsymbol{\gamma}$ is treated as a field (*i.e.*, non-local) variable or additional continuum degree-of-freedom. Analogous to the phenomenological case (2.70) in terms of $\boldsymbol{F}_{\mathrm{P}}$ discussed above, each $\dot{\boldsymbol{\gamma}}$ is determined by the local form of the flow rule on ∂B_r, such that $\boldsymbol{\varphi}$ vanishes identically (Svendsen, 2000, 2002). In summary, then, the continuum is characterized by the fields $(\boldsymbol{\chi}, \theta, \boldsymbol{\gamma})$ in the current approach to extended crystal plasticity. As has been shown in the application of such models as this to numerical simulation of additional hardening due to deformation incompatibility (*e.g.*, Svendsen and Reese, 2003; Svendsen, 2004; Evers *et al.*, 2004), in most structural problems, only a few of the additional degrees of freedom $\boldsymbol{\gamma}$ are generally active in only some parts of the structure at any time. Consequently, the use of material model adaptivity techniques in the numerical implementation makes the use of such extended models tractable for structural simulations.

2.6 Comparison with some other extended continuum approaches

Some of the results of the current approach, in particular as based on $\boldsymbol{G}_{\mathrm{i}}$, are formally similar to those derived by Gurtin (2002) using the concept of microforces (*e.g.*, Gurtin, 2000) and the pure mechanical version of dissipation inequality. Gurtin's theory is based on the assumption that the power expended by each independent rate-like kinematical variable can be expressed in term of an associated force system consistent with its own balance. The basic rate-like variables are the material velocity $\dot{\boldsymbol{\chi}}$, describing the macroscopic motion of the body, $\boldsymbol{L}_{\mathrm{E}}$, describing the instantaneous lattice rotation and stretching, and $\dot{\gamma}_{\mathfrak{a}}$, describing the plastic deformation in each glide system due to motion of dislocations. In his approach, each change of state of the material is associated with macroscopic and microscopic force systems. The macroscopic force system is defined by a traction $\boldsymbol{t}$ and a body force density $\boldsymbol{b}$ including external and inertial forces. The microscopic system is defined by a lattice (Kirchhoff) stress $\boldsymbol{K}$ work-conjugate to $\boldsymbol{L}_{\mathrm{E}}$, an internal microforce $\pi_{\mathfrak{a}}$ work conjugate to $\dot{\gamma}_{\mathfrak{a}}$, a microstress $\boldsymbol{\xi}_{\mathrm{r}\mathfrak{a}}$ work-conjugate to $\nabla^{\mathrm{r}}\dot{\gamma}_{\mathfrak{a}}$, and a microtraction $\Xi_{\mathfrak{a}}$ work-conjugate to $\dot{\gamma}_{\mathfrak{a}}$. The main idea of his approach is the assertion that the external power expended on any (referential) subbody P

$$\mathcal{W}_{\mathrm{ext}} = \int_{\partial P} \boldsymbol{t}\cdot\dot{\boldsymbol{\chi}}\,da_{\mathrm{r}} + \int_{P} \boldsymbol{b}\cdot\dot{\boldsymbol{\chi}}\,dv_{\mathrm{r}} + \sum\nolimits_{\mathfrak{a}}\int_{\partial P}\Xi_{\mathfrak{a}}\dot{\gamma}_{\mathfrak{a}}\,da_{\mathrm{r}} \tag{2.89}$$

is equal to internal power expended within the same subbody

$$\mathcal{W}_{\mathrm{int}} = \int_{P} \boldsymbol{K}\cdot\boldsymbol{L}_{\mathrm{E}}\,dv_{\mathrm{r}} + \sum\nolimits_{\mathfrak{a}}\int_{P}(\pi_{\mathfrak{a}} + \boldsymbol{\xi}_{\mathrm{r}\mathfrak{a}}\cdot\nabla^{\mathrm{r}}\dot{\gamma}_{\mathfrak{a}})\,dv_{\mathrm{r}} \quad . \tag{2.90}$$

Here, the kinematic variables $\dot{\boldsymbol{\chi}}$, $\boldsymbol{L}_{\mathrm{E}}$ and $\dot{\gamma}_{\mathfrak{a}}$ have to fulfill the kinematic restriction

$$\boldsymbol{L} = \dot{\boldsymbol{F}}_{\mathrm{E}}\boldsymbol{F}_{\mathrm{E}}^{-1} + \boldsymbol{F}_{\mathrm{E}}\sum\nolimits_{\mathfrak{a}}\dot{\gamma}_{\mathrm{a}}\,(\boldsymbol{s}_{\mathfrak{a}}\otimes\boldsymbol{n}_{\mathfrak{a}})\boldsymbol{F}_{\mathrm{E}}^{-1} =:\, \boldsymbol{L}_{\mathrm{E}} + \sum\nolimits_{\mathfrak{a}}\dot{\gamma}_{\mathfrak{a}}\bar{\boldsymbol{s}}_{\mathfrak{a}}\otimes\bar{\boldsymbol{n}}_{\mathfrak{a}} \tag{2.91}$$

following from (2.19), with $\bar{\boldsymbol{s}}_{\mathfrak{a}} = \boldsymbol{F}_{\mathrm{E}}\,\boldsymbol{s}_{\mathfrak{a}}$ and $\bar{\boldsymbol{n}}_{\mathfrak{a}} = \boldsymbol{F}_{\mathrm{E}}^{-\mathrm{T}}\boldsymbol{n}_{\mathfrak{a}}$.

Consider first the case without slip, *i.e.*, $\dot{\gamma}_{\mathfrak{a}} = 0$. In this case, the equivalence of the external and internal power in combination with integration by parts yields

$$\int_{\partial P}(\boldsymbol{t} - \boldsymbol{P}\boldsymbol{n}_{\mathrm{r}})\cdot\dot{\boldsymbol{\chi}}\,da_{\mathrm{r}} = -\int_{P}(\mathrm{div}_{\mathrm{r}}\boldsymbol{P} + \boldsymbol{b})\cdot\dot{\boldsymbol{\chi}}\,dv_{\mathrm{r}} \quad , \tag{2.92}$$

with $\boldsymbol{P} := \boldsymbol{K}\boldsymbol{F}^{-\mathrm{T}}$ the first Piola-Kirchhoff stress. For this to hold for arbitrary P and $\dot{\boldsymbol{\chi}}$, the usual traction condition $\boldsymbol{t} = \boldsymbol{P}\boldsymbol{n}$ and the classical local momentum balance

$$\mathrm{div}_{\mathrm{r}}\boldsymbol{P} + \boldsymbol{b} = \boldsymbol{0} \tag{2.93}$$

follow. Next, consider a rigid-body motion $\dot{\boldsymbol{\chi}} = \boldsymbol{a} + \boldsymbol{\omega}\times\boldsymbol{x}$, with $\boldsymbol{a}$ and $\boldsymbol{\omega}$ constant. Assuming in this case that there is no internal working, *i.e.*, $\mathcal{W}_{\mathrm{int}} = 0$, one obtains

$$\int_{P}(\boldsymbol{\omega}\times\boldsymbol{I})\cdot\boldsymbol{K}\,dv_{\mathrm{r}} = 0 \quad . \tag{2.94}$$

Since the tensor $\boldsymbol{\omega}\times\boldsymbol{I}$ is skew and $\boldsymbol{\omega}$ arbitrary, $\boldsymbol{K}$ must be symmetric. The microscopic force balance is obtained by setting $\dot{\boldsymbol{\chi}} = \boldsymbol{0}$ and letting $\dot{\gamma}_{\mathfrak{a}}$ be arbitrary. Then from (2.91) follows

$$\sum\nolimits_{\mathfrak{a}}\dot{\gamma}_{\mathfrak{a}}(\bar{\boldsymbol{s}}_{\mathfrak{a}}\otimes\bar{\boldsymbol{n}}_{\mathfrak{a}}) = -\boldsymbol{L}_{\mathrm{E}} \quad , \tag{2.95}$$

and consequently

$$\boldsymbol{K} \cdot \boldsymbol{L}_{\mathrm{E}} = -\sum\nolimits_{\mathfrak{a}} \tau_{\mathfrak{a}} \dot{\gamma}_{\mathfrak{a}} \quad , \tag{2.96}$$

with the resolved shear stress

$$\tau_{\mathfrak{a}} := \bar{\boldsymbol{s}}_{\mathfrak{a}} \cdot \boldsymbol{K} \bar{\boldsymbol{n}}_{\mathfrak{a}} = \boldsymbol{s}_{\mathfrak{a}} \cdot \boldsymbol{F}_{\mathrm{E}}^{\mathrm{T}} \boldsymbol{K} \boldsymbol{F}_{\mathrm{E}}^{-\mathrm{T}} \boldsymbol{n}_{\mathfrak{a}} \quad . \tag{2.97}$$

Using this and integrating by parts one obtains from the the equivalence of the external and internal power

$$\sum\nolimits_{\mathfrak{a}} \int_{\partial P} (\Xi_{\mathfrak{a}} - \boldsymbol{\xi}_{\mathrm{r}\mathfrak{a}} \cdot \boldsymbol{n}) \dot{\gamma}_{\mathfrak{a}} \, da_{\mathrm{r}} = -\sum\nolimits_{\mathfrak{a}} \int_{P} (\mathrm{div}_{\mathrm{r}} \, \boldsymbol{\xi}_{\mathrm{r}\mathfrak{a}} + \tau_{\mathfrak{a}} - \pi_{\mathfrak{a}}) \dot{\gamma}_{\mathfrak{a}} \, dv_{\mathrm{r}} \quad . \tag{2.98}$$

This yields

$$\Xi_{\mathfrak{a}} = \boldsymbol{\xi}_{\mathrm{r}\mathfrak{a}} \cdot \boldsymbol{n}_{\mathrm{r}} \quad , \tag{2.99}$$

representing the microtraction condition on the boundary, as well as

$$\mathrm{div}_{\mathrm{r}} \, \boldsymbol{\xi}_{\mathrm{r}\mathfrak{a}} + \tau_{\mathfrak{a}} - \pi_{\mathfrak{a}} = 0 \quad , \tag{2.100}$$

representing the microforce balance.

To formulate constitutive relations, Gurtin uses the purely mechanical form of the second law in which the temporal increase in free energy of any subbody P is less than or equal to the power expended on P. In terms of the referential free energy density ψ_{r}, the second law takes the form

$$\dot{\overline{\int_{P} \psi_{\mathrm{r}}}} - \mathcal{W}_{\mathrm{ext}} \leqslant 0 \quad . \tag{2.101}$$

Since P is arbitrary, one obtains

$$\dot{\psi}_{\mathrm{r}} - \boldsymbol{K} \cdot \boldsymbol{D}_{\mathrm{E}} - \sum\nolimits_{\mathfrak{a}} (\boldsymbol{\xi}_{\mathrm{r}\mathfrak{a}} \cdot \nabla^{\mathrm{r}} \dot{\gamma}_{\mathfrak{a}} + \pi_{\mathfrak{a}} \gamma_{\mathfrak{a}}) \leqslant 0 \tag{2.102}$$

via the symmetry of $\boldsymbol{K}$, with $\boldsymbol{D}_{\mathrm{E}}$ the symmetric part of $\boldsymbol{L}_{\mathrm{E}}$. In terms of the “true” lattice stress $\boldsymbol{S}_{\mathrm{E}} := \boldsymbol{F}_{\mathrm{E}}^{-1} \boldsymbol{K} \boldsymbol{F}_{\mathrm{E}}^{-\mathrm{T}}$, the above inequality can be rewritten as

$$\dot{\psi}_{\mathrm{r}} - \boldsymbol{S}_{\mathrm{E}} \cdot \dot{\boldsymbol{E}}_{\mathrm{E}} - \sum\nolimits_{\mathfrak{a}} (\boldsymbol{\xi}_{\mathrm{r}\mathfrak{a}} \cdot \nabla^{\mathrm{r}} \dot{\gamma}_{\mathfrak{a}} + \pi_{\mathfrak{a}} \dot{\gamma}_{\mathfrak{a}}) \leqslant 0 \quad , \tag{2.103}$$

where $\boldsymbol{E}_{\mathrm{E}}$ represents the elastic Green deformation tensor. Assuming plastic incompressibility, Gurtin assumes the simple additive form

$$\psi_{\mathrm{i}} = \frac{1}{2} \boldsymbol{E}_{\mathrm{E}} \cdot \mathcal{C}_{\mathrm{E}} \boldsymbol{E}_{\mathrm{E}} + \Psi(\boldsymbol{G}_{\mathrm{i}}) \tag{2.104}$$

for ψ_{i} in terms of the usual elasticity tensor $\mathcal{C}_{\mathrm{E}}$. Substituting this into (2.103), the dissipation inequality reduces to

$$\begin{aligned} &\{\partial_{\boldsymbol{E}_{\mathrm{E}}} \psi_{\mathrm{i}} - \boldsymbol{S}_{\mathrm{E}}\} \cdot \dot{\boldsymbol{E}}_{\mathrm{E}} \\ &+ \sum\nolimits_{\mathfrak{a}} \{\boldsymbol{s}_{\mathfrak{a}} \cdot [(\partial_{\boldsymbol{G}_{\mathrm{i}}} \Psi) \boldsymbol{G}_{\mathrm{i}}^{\mathrm{T}} + (\partial_{\boldsymbol{G}_{\mathrm{i}}} \Psi)^{\mathrm{T}} \boldsymbol{G}_{\mathrm{i}}] \boldsymbol{n}_{\mathfrak{a}} - \pi_{\mathfrak{a}}\} \dot{\gamma}_{\mathfrak{a}} \\ &+ \sum\nolimits_{\mathfrak{a}} \{\boldsymbol{F}_{\mathrm{P}}^{-1} [\boldsymbol{n}_{\mathfrak{a}} \times (\partial_{\boldsymbol{G}_{\mathrm{i}}} \Psi)^{\mathrm{T}} \boldsymbol{s}_{\mathfrak{a}}] - \boldsymbol{\xi}_{\mathrm{r}\mathfrak{a}}\} \cdot \nabla^{\mathrm{r}} \dot{\gamma}_{\mathfrak{a}} \leqslant 0 \end{aligned} \tag{2.105}$$

again with plastic incompressibility. Requiring that (2.105) holds for all choices of $\boldsymbol{E}_{\mathrm{E}}$, $\dot{\gamma}_{\mathfrak{a}}$ and $\nabla^{\mathrm{r}} \dot{\gamma}_{\mathfrak{a}}$, the linearity of the left-hand side of (2.105) in these variables implies the constitutive restrictions (i), the stress-strain relation $\boldsymbol{S}_{\mathrm{E}} = \partial_{\boldsymbol{E}_{\mathrm{E}}} \psi = \mathcal{C}_{\mathrm{E}} \boldsymbol{E}_{\mathrm{E}}$, (ii), the microstress relation

$$\boldsymbol{\xi}_{\mathrm{r}\mathfrak{a}} = \boldsymbol{F}_{\mathrm{P}}^{-1} \boldsymbol{\xi}_{\mathrm{i}\mathfrak{a}} = \boldsymbol{F}_{\mathrm{P}}^{-1} [\boldsymbol{n}_{\mathfrak{a}} \times (\partial_{\boldsymbol{G}_{\mathrm{i}}} \Psi)^{\mathrm{T}} \boldsymbol{s}_{\mathfrak{a}}] \quad , \tag{2.106}$$

and (iii), the residual inequality

$$\sum\nolimits_{\mathfrak{a}}\{\pi_{\mathfrak{a}} - \boldsymbol{s}_{\mathfrak{a}}\cdot[(\partial_{\boldsymbol{G}_{\mathrm{i}}}\Psi)\boldsymbol{G}_{\mathrm{i}}^{\mathrm{T}} + (\partial_{\boldsymbol{G}_{\mathrm{i}}}\Psi)^{\mathrm{T}}\boldsymbol{G}_{\mathrm{i}}]\boldsymbol{n}_{\mathfrak{a}}\}\dot{\gamma}_{\mathfrak{a}} \geqslant 0 \quad . \tag{2.107}$$

A sufficient condition fulfilling this inequality is given by

$$\pi_{\mathfrak{a}} - \boldsymbol{s}_{\mathfrak{a}}\cdot[(\partial_{\boldsymbol{G}_{\mathrm{i}}}\Psi)\boldsymbol{G}_{\mathrm{i}}^{\mathrm{T}} + (\partial_{\boldsymbol{G}_{\mathrm{i}}}\Psi)^{\mathrm{T}}\boldsymbol{G}_{\mathrm{i}}]\boldsymbol{n}_{\mathfrak{a}} = H(\dot{\gamma}_{\mathfrak{a}})\sigma_{\mathfrak{a}} \quad , \tag{2.108}$$

where $H(\dot{\gamma}_{\mathfrak{a}})$ represents a standard, invertible strain-rate-dependent viscosity function, and the hardening variable $\sigma_{\mathfrak{a}}$ is given by the evolution relation

$$\dot{\sigma}_{\mathfrak{a}} = \sum\nolimits_{\mathfrak{b}} h_{\mathfrak{a}\mathfrak{b}}(\boldsymbol{\sigma}, \boldsymbol{G}_{\mathrm{i}})|\dot{\gamma}_{\mathfrak{b}}| \quad . \tag{2.109}$$

Here, the hardening matrix $h_{\mathfrak{a}\mathfrak{b}}$ depends in general on the dislocation density tensor via, *e.g.*, the forest dislocation measures $\lambda_{\mathfrak{a}}$ as given in (2.51) from Acharya and Bassani (2000). Substituting then (2.106) and (2.108) into the microforce balance (2.100) yields

$$\tau_{\mathfrak{a}} = H(\dot{\gamma}_{\mathfrak{a}})\sigma_{\mathfrak{a}} + x_{\mathfrak{a}} \quad , \tag{2.110}$$

with

$$x_{\mathfrak{a}} := \boldsymbol{s}_{\mathfrak{a}}\cdot\{2\,\mathrm{sym}(\partial_{\boldsymbol{G}_{\mathrm{i}}}\Psi)\boldsymbol{G}_{\mathrm{i}} + \mathrm{curl}_{\mathrm{i}}(\partial_{\boldsymbol{G}_{\mathrm{i}}}\Psi)\}\boldsymbol{n}_{\mathfrak{a}} \tag{2.111}$$

the glide-system back stress in Gurtin's formulation formally analogous to (2.87) in the formulation of the previous section. In particular, (2.110) can be derived from (2.85) from the last section when we specialize it to isothermal conditions and work with the special forms $\psi = \psi_{\mathrm{i}}(\boldsymbol{F}_{\mathrm{E}}, \boldsymbol{G}_{\mathrm{i}})$ and $d = d_{\mathrm{i}}(\boldsymbol{\varsigma}, \dot{\boldsymbol{\gamma}})$ of the free energy density and dissipation potential, respectively. Indeed, with the identification $\varsigma_{\mathfrak{a}} \equiv \sigma_{\mathfrak{a}}$, we have that $\partial_{\dot{\gamma}_{\mathfrak{a}}} d_{\mathrm{r}} \equiv H(\dot{\gamma}_{\mathfrak{a}})\sigma_{\mathfrak{a}}$. Solving (2.110) for $\dot{\gamma}_{\mathfrak{a}}$, one obtains the flow rule

$$\dot{\gamma}_{\mathfrak{a}} = H^{-1}\left(\frac{\tau_{\mathfrak{a}} - x_{\mathfrak{a}}}{\sigma_{\mathfrak{a}}}\right) \tag{2.112}$$

with H^{-1} being the inverse function of H. On this form one can see that accounting for the presence of GNDs leads to additional hardening with two different mechanisms. The hardening which arises from the energy storage is represented by the GND-based back stress $\boldsymbol{s}_{\mathfrak{a}} \otimes \boldsymbol{n}_{\mathfrak{a}} \cdot \{(\partial_{\boldsymbol{G}_{\mathrm{i}}}\Psi)^{\mathrm{T}}\boldsymbol{G}_{\mathrm{i}} + \mathrm{curl}_{\mathrm{i}}(\partial_{\boldsymbol{G}_{\mathrm{i}}}\Psi)\}$ having as such a long-range character. It is ascribed to the elastic interaction between dislocations. The other mechanism which influences the hardening rate via (2.109) is purely dissipative and nondirectional, and so has a short-range character.

A non-thermodynamic approach to the formulation of extended crystal plasticity models for FCC systems taking into account as well both short-range and long-range GND-based hardening effects was developed by Evers *et al.* (2004). In their approach, which relies on a mixture of phenomenology and dislocation dynamics, the viscoplastic flow rule is given by the relation

$$\dot{\gamma}_{\mathfrak{a}} = \dot{\gamma}_{\mathfrak{a}0}\left(\frac{|\tau_{\mathfrak{a}} - b_{\mathfrak{a}}|}{s_{\mathfrak{a}}}\right)^{1/m}\mathrm{sgn}(\tau_{\mathfrak{a}} - b_{\mathfrak{a}}) \quad . \tag{2.113}$$

Here, $\tau_{\mathfrak{a}}$ is the resolved shear stress of the elastic second Piola-Kirchhoff stress tensor $\boldsymbol{T}_{\mathrm{E}} = \boldsymbol{\mathcal{C}}\boldsymbol{E}_{\mathrm{E}}$, $b_{\mathfrak{a}}$ is the resolved back stress, assumed to arise from GNDs, and $s_{\mathfrak{a}}$ is the slip resistance, assumed to depend in contrast to classical models also on GND density. In (2.113), note that the effective stress is given by the difference between the the resolved shear stress calculated in the intermediate configuration and the back stress calculated in the reference configuration. This is possible due to the non-thermodynamical developing of the theory. In a thermodynamically developed theory only combination of variables defined in the same configuration are possible. This notwithstanding, their flow rule is otherwise analogous to Gurtin's flow rule (2.112), or to that of the current work. In contrast to the current approach, Evers *et al.* (2004) formulated their constitutive relation for the back stress by considering the elastic stress around a dislocation. The short-range interactions between dislocations including both SSDs and GNDs are taken into account by the slip resistance $s_\mathfrak{a}$. The type and number of short-range interactions can be described by a set of interaction coefficients forming the interaction matrix $a_{\mathfrak{a}\mathfrak{a}}$ (Franciosi and Zaoui, 1982) that was already mentioned in the context of the Dai and Parks (1997) model. The slip resistance of the system $\mathfrak{a}$ is then given as the square root of the effective obstacle density according to Ashby (1970)

$$s_\mathfrak{a} = c\mu b\sqrt{\sum\nolimits_\mathfrak{a} a_{\mathfrak{a}\mathfrak{a}}\rho^S_\mathfrak{a} + a_{\mathfrak{a}\mathfrak{a}}\rho^G_\mathfrak{a}} \quad . \tag{2.114}$$

The total back stress tensor is then defined in their model in the reference configuration as the sum of the resulting long-range shear stress contributions ($\tau^e_\mathfrak{a}$ and $\tau^s_\mathfrak{a}$ from the edge and screw GND density fields, respectively) on the corresponding slip system $\mathfrak{a}$, *i.e.*,

$$\boldsymbol{X} = \sum\nolimits_\mathfrak{a} (\tau^e_\mathfrak{a} + \tau^s_\mathfrak{a})(\boldsymbol{s}_\mathfrak{a} \otimes \boldsymbol{n}_\mathfrak{a} + \boldsymbol{n}_\mathfrak{a} \otimes \boldsymbol{s}_\mathfrak{a}) \tag{2.115}$$

The determination of the resolved long-range shear contributions $\tau^e_\mathfrak{a}$ and $\tau^s_\mathfrak{a}$ in the undeformed configuration stems from the equation for the stress concentration near individual edge and screw dislocations. In order to quantify that effect, the resulting long-range stress on the slip system $\mathfrak{a}$ is computed by an analytical integration procedure of the equation for individual dislocations over a circular domain with radius R assuming that GND density varies linearly in space, yielding

$$\tau^e_\mathfrak{a} = -\frac{\mu b R^2}{8(1-\nu)}\, \boldsymbol{s}_\mathfrak{a} \cdot \nabla^{\mathrm{r}} \rho^{G(e)}_\mathfrak{a} \tag{2.116}$$

and

$$\tau^e_\mathfrak{a} = -\frac{\mu b R^2}{4}\, \boldsymbol{l}_\mathfrak{a} \cdot \nabla^{\mathrm{r}} \rho^{G(s)}_\mathfrak{a} \quad . \tag{2.117}$$

Here, $\rho^{G(e)}_\mathfrak{a}$ represents a GND density of edge type having Burgers vector parallel to $\boldsymbol{s}_\mathfrak{a}$ and a line vector parallel to $\boldsymbol{l}_\mathfrak{a} = \boldsymbol{s}_\mathfrak{a} \times \boldsymbol{n}_\mathfrak{a}$. Further, $\rho^{G(s)}_\mathfrak{a}$ is a GND density of screw type with both Burgers and line vector in $\boldsymbol{s}_\mathfrak{a}$ direction. In turn, crystallographic GND densities (12 of edge type and 6 of screw type for FCC single crystalls) are extracted from the gradients of the crystallographic slips

$$\rho^{G(e)}_\mathfrak{a} = \frac{1}{b}\, \boldsymbol{s}_\mathfrak{a} \cdot \nabla^{\mathrm{r}} \gamma_\mathfrak{a} \tag{2.118}$$

$$\rho^{G(s)}_\mathfrak{a} = \frac{1}{b}\left(\boldsymbol{s}_\mathfrak{a} \times \boldsymbol{n}_1 \cdot \nabla^{\mathrm{r}} \gamma_\mathfrak{a} + \boldsymbol{s}_\mathfrak{a} \times \boldsymbol{n}_2 \cdot \nabla^{\mathrm{r}} \gamma_\mathfrak{a}\right) \quad . \tag{2.119}$$

Since a screw dislocation can glide in a FCC single crystal on two slip planes, the equation (2.119) contains two parts, the one from the incompatible slip on the plane $\boldsymbol{n}_1$ the other on the plane $\boldsymbol{n}_2$, whereby these two slip planes intersect each other on the line tangent to the screw dislocation of type $\mathfrak{a}$. In contrast to the Dai and Parks approach, Evers *et al.* (2004) do not consider screw dislocations with the same Burgers vector but gliding on different systems to be distinct. Note that (2.118) and (2.119) yield non-vanishing results if the overall deformation is compatible $\mathrm{curl}_{\mathrm{r}} \boldsymbol{F}_{\mathrm{P}} = \boldsymbol{0}$.

2.7 Discussion

Although the general formulation in this work has been a continuum thermodynamic one, little has been said about the possible role of non-mechanical processes related to the temperature or to heat conduction in all this. Starting with the latter, note that the reduced form (2.58) for the total energy flux can be compared with the standard form

$$\boldsymbol{h}_{\mathrm{S}} = \boldsymbol{P}^{\mathrm{T}}\dot{\boldsymbol{\chi}} - \boldsymbol{q} \tag{2.120}$$

of this flux involving the first Piola-Kirchhoff stress $\boldsymbol{P}$ and heat flux $\boldsymbol{q}$. As has been discussed in Svendsen (2000, 2002), we have conceptually here two choices. Taking the approach of Maugin (1990), for example, the constitutive assumption

$$\boldsymbol{\phi} \equiv \boldsymbol{q}/\theta + 2\ \mathrm{axs}\{(\partial_{\boldsymbol{G}_{\mathrm{r}}}\psi_{\mathrm{r}})^{\mathrm{T}}\dot{\boldsymbol{F}}_{\mathrm{P}}\}/\theta \tag{2.121}$$

for the entropy flux yields $\boldsymbol{h} = \boldsymbol{h}_{\mathrm{S}}$. On the other hand, the Clausius-Duhem constitutive form

$$\boldsymbol{\phi} \equiv \boldsymbol{q}/\theta \tag{2.122}$$

for the entropy flux implies that $\boldsymbol{h}$ from (2.58) is non-standard, *i.e.*, $\boldsymbol{h} \neq \boldsymbol{h}_{\mathrm{S}}$. As pointed out by Svendsen (2000, 2002), this dichotomy is an old one, going back in essence to the modeling of diffusion, classical mixture theory, the interpretation of "entropy flux" and "heat flux" in phenomenology and the relation between these two (Gurtin, 1971, Footnote 1). There, the issue was one of whether diffusion flux is to be interpreted as a flux of energy (*e.g.*, Eckhart, 1940; Gurtin, 1971) or a flux of entropy (*e.g.*, Meixner and Reik, 1959; DeGroot and Mazur, 1962; Müller, 1968). In the current context, the flux (density) of interest is $2\ \mathrm{axs}\{(\partial_{\boldsymbol{G}_{\mathrm{r}}}\psi_{\mathrm{r}})^{\mathrm{T}}\dot{\boldsymbol{F}}_{\mathrm{P}}\}$ related to energy storage due to GND development. In the context of (2.121), this flux (*i.e.*, divided by θ) is being interpreted as an entropy flux. On the other hand, in the context of (2.122), it is being interpreted as an energy flux (analogous formally to the abstract idea of "interstitial work" from Dunn and Serrin (1985)). Returning to the current context of metal plasticity, generally this latter interpretation is followed by (*e.g.*, Gurtin, 2000; Svendsen, 2000; Gurtin, 2002; Svendsen, 2002). In this vein, note that, in some earlier works (*e.g.*, Steinmann, 1996), terms analogous to $2\ \mathrm{axs}\{(\partial_{\boldsymbol{G}_{\mathrm{r}}}\psi_{\mathrm{r}})^{\mathrm{T}}\dot{\boldsymbol{F}}_{\mathrm{P}}\}$ were treated as part of a non-negative boundary dissipation. Since the dissipation inequality must hold for every subdomain of the body, however, and no boundary conditions can be formulated which could ensure the nonnegativity of such surface dissipation in general, contributions such as $2\ \mathrm{axs}\{(\partial_{\boldsymbol{G}_{\mathrm{r}}}\psi_{\mathrm{r}})^{\mathrm{T}}\dot{\boldsymbol{F}}_{\mathrm{P}}\}$ should be treated as part of the energy flux as done in (2.58).

All of the extensions to crystal plasticity discussed in this work including the current one are based on continuum and phenomenological considerations in the context of crystal plasticity and continuum dislocation theory extended to include the effects of deformation inhomogeneity. One basic shortcoming of such a "purely" phenomenological approach is the lack of specific, derived forms for the constitutive relations. For example, this leads in applications to the assumption that characteristic material lengthscales are constant. More fundamental considerations show, however, that this is not the case. In the small-deformation continuum dislocation context, for example, Mesarovic (2005) recently showed that such lengthscales depend in particular on "non-local" dislocation-dislocation interactions. Alternatively, dislocation dynamics treated with the help of statistical mechanics leads to such results. For example, by using a statistical-mechanics description of the collective behavior of pure edge dislocations, Groma (1997); Groma *et al.* (2003) obtained in the small-deformation context a back stress based on a non-constant lengthscale arising from the nonhomogeneous distribution of GNDs. Such an approach has also been pursued by Malygin (1999) and El-Azab (2000). Restricting attention to the glide-system level, the theory is the over-damped motion of an ensemble of parallel edge dislocations moving in the glide plane. With the help of statistical mechanics and results from discrete dislocation simulations (*e.g.*, Zaiser *et al.*, 2001), in particular the observation that systems with different densities become "self-similar" when the spatial scaling is given by the dislocation spacing, *i.e.*, $1/\sqrt{\rho}$, Groma *et al.* (2003) showed that the characteristic material lengthscale is not constant but depends on the total dislocation density ρ. When combined with small deformation crystal plasticity (*e.g.*, Yefimov *et al.*, 2004), one can show that the structure of the resulting flow rule is similar to that of models based on the premise that GND development results in additional energy storage (*e.g.*, Gurtin, 2002; Svendsen, 2002) as well to that of micromechanical models such as Evers *et al.* (2004). Again, the main difference is the internal length which determines the nonlocal behavior. The investigation of this and many other issues, together with the generalization of such statistical-mechanics-based and transport-theory-based approaches to large deformation, is the focus of ongoing research, and will be reported on in future work.

References

Acharya, A., 2004. Constitutive analysis of finite deformation field dislocation mechanics, J. Mech. Phys. Solics, 52, 301-316.

Acharya, A., Bassani, J.L., 2000. Lattice incompatibility and a gradient theory of crystal plasticity. J. Mech. Phys. Solids, 48, 1565-1595.

Acharya, A., Bassani, J.L., Beaudoin, A., 2003. Geometrically necessary dislocations, hardening, and a simple gradient theory of crystal plasticity. Scripta mater., 48, 167-172.

Arsenlis, A., Parks, D. M., 1999. Crystallographic aspects of geometrically-necessary and statistically-stored dislocation density. Acta Mater., 47, 1–115.

Asaro, R. J., Rice, J. R., 1979. Strain localization in ductile single crystals. J. Mech. Phys. Solids, 25, 309–338.

Ashby, M. F., 1970. The deformation of plastically non-homogeneous materials. Phil. Mag., 21, 399–424.

Bilby, B. A., Bullough, R. & Smith, E., 1955. Continuous distributions of dislocations: a new application of the methods of non-Riemannian geometry, Proc. Roy. Soc. A 231, 263–273.

Busso, E. F., Meissonnier, F. T., O'Dowd, N. P., 2000. gradient-dependent deformation of two-phase single crystals. J. Mech. Phys. Solids, 48, 2333–2361.

Cermelli, P., Gurtin, M. E., 2001. On the characterization of the gemetrically necessary dislocations in finite plasticity. J. Mech. Phys. Solids, 49, 1539–1568.

Dai, H., Parks, D. M., 1997. Geometrically-necessary dislocation density and scale-dependent crystal plasticity. Proceedings of Plasticity'97, A. S. Khan, editor, pp. 17–18.

Davini, C., 1986. A proposal for a continuum theory of defective crystals, Arch. Rat. Mech. Anal., 96, 295–317.

Davini, C., Parry, G. P., 1989. On defect-preserving deformations in crystals, Int. J. Plast., 5, 337–369.

DeGroot, S. R., Mazur, P., 1962. Non-Equlibrium Thermodynamics, Wiley-Interscience.

Dunn, J.E., Serrin, J., 1985. On the thermomechanics of interstitial working. Arch. Rat. Mech. Anal., 88, 95–133.

Eckhart, C., 1940. The thermodynamics of irreversible processes, II. Fluid mixtures, Phys. Rev., 58, 269–275.

El-Azab, A., 2000. Statistical mechanics treatment of the evolution of dislocation distributions in single crystals, Phys. Rev. B, 61, 11956-11966.

El-Dasher, B.S., Adams, B.L., Rollett, A.D., 2003. Viewpoint: experimental recovery of geometrically-necessary dislocation density in polycrystals, Scripta Mater., 48, 141–145.

Evers, L.P., Brekelmanns, W.A.M., Geers, M.G.D., 2004. Non-local crystal plasticity model with intrinsic SSD and GND effects. J. Mech. Phys. Solids, 52, 2379–2401.

Fleck, N. A., Hutchinson, J. W., 1993. A phenomenological theory for strain gradient effects in plasticity, J. Mech. Phys. Solids, 41, 1825–1857.

Fleck, N. A., Muller, G. M., Ashby, M. F., Hutchinson, J. W., 1994. Strain gradient plasticity: theory and experiment. Acta Metal. Mater., 42, 475–487.

Fleck, N. A., Hutchinson, J. W., 1997. Strain gradient plasticity, Adv. Appl. Mech., 33, 295–361.

Flouriot, S., Forest, S., Cailletaud, G., Koster, A., Remy, L., Burgardt, B., Gros, V., Mosset, S., Delautre, J., 2003. Strain localization at the crack tip in single crystal CT specimens under monotonous loading: 3D Finite Element analyses and application to nickel-base superalloys, Int. J. Fracture, 124, 43–77.

Forest, S., Cailletaud, G., Sievert, R., 1997. A Cosserat theory for elastoviscoplastic single crystals at finite deformation. Arch. Mech., 49, 705–736.

Forest, S., Boubidi, P., Sievert, R., 2001. Strain localization patterns at a crack tip in generalized single crystal plasticity. Scripta mater., 44, 953–958.

Forest, S., Sievert, R., Aifantis, E. C., 2002. Strain gradient crystal plasticity: thermomechanical formulations and applications. J. Mech. Beh. Mat., 13, 219-232.

Franciosi, P., Zaoui, A., 1982. Multislip in f.c.c. crystals a theoretical approach compared with experimental data. Acta Metal., 30, 1627–1637.

Groma, I., 1997. Link between microscopic and mesoscopic length-scale description of the collective behaviour of dislocations. Phys. Rev., B 56, 5807–5813.

Groma, I., Csizor, F.F., Zaiser. M., 2003. Spatial correlation and higher-order gradient terms in a continuum description of dislocation dynamics. Acta Mater., 51, 1271–1281.

Gurtin, M. E., 1971. On the thermodynamics of chemically reacting fluid mixtures, Arch. Rat. Mech. Anal., 43, 198–212.

Gurtin, M. E., 2000. On the plasticity of single crystals: free energy, microforces, plastic-strain gradients. J. Mech. Phys. Solids, 48, 989–1036.

Gurtin, M. E., 2002. A theory of viscoplasticity that accounts for geometrically necessary dislocations. J. Mech. Phys. Solids, 50, 5–32.

Kafadar, C.B., Eringen, A.C., 1971. Micropolar media: I the classical theory. Int. J. Engng. Sci., 9, 271–305.

Kröner, E., 1960. Allgemeine Kontinuumstheorie der Versetzungen und Eigenspannungen, Arch. Rat. Mech. Anal., 4, 273–334.

Landau, L. D., Lifshitz, E. M., 1970. Theory of elasticity, Second edition, Pergamon Press.

Le, K. C., Stumpf, H., 1996. Non-linear continuum theory of dislocations Int. J. Engng. Sci., 34, 339–358.

Lee, E. H., 1969. Elastic-plastic deformation at finite strains. J. Appl. Mech. 36, 1–6.

Levkovitch, V., Sievert, R., Svendsen, B., 2005. Application of extended crystal plasticity to the modeling of glide and kink bands and of crack opening in single crystals, Comp. Mat. Sci., 32, 426–434.

Malygin, G. A., 1999. Dislocation self-organization processes and crystal plasticity, Physics Uspekhi, 42, 887-916.

Mandel, J., 1971. Plasticité classique et viscoplasticité. CISM Courses and Lectures, Volume 97, Springer-Verlag.

Maugin, G., 1990. On internal variables and dissipative structures. Int. J. Non-equil. Thermo., 15, 173–192.

Meixner, J., Reik, H. G., 1959. Thermodynamik der irreversiblen Prozesse, in: Handbuch der Physik, III/2, S. Flügge, editor, Springer-Verlag.

Menzel, A., Steinmann, P., 2000. On the continuum formulation of higher gradient plasticity for single and polycrystals, J. Mech. Phys. Solids, 48, 1777–1796.

Mesarovic, S. D., 2005. Energy, configurational forces and characteristic lengths associated with the continuum description of geometrically necessary dislocations, Int. J. Plast., 21, 1855-1889.

Müller, I., 1968. A thermodynamic theory of mixtures of fluids, Arch. Rat. Mech. Anal., 28, 1–39.

Müller, I., 1985. Thermodynamics, Pitman.

Mura, T., 1987. Micromechanics of defects in solids, Kluwer Publishers.

Naghdi, P., Srinivasa, A. R., 1993. A dynamical theory of structured solids. I. Basic developments, Phil. Trans. Roy. Soc., 345A, 424–458.

Naghdi, P., Srinivasa, A. R., 2004. Characterisation of dislocations and their influence on plastic deformation in single crystals, Int. J. Solids Structs., 7, 1157–1182.

Noll, W., 1967. Material uniform inhomogeneous material bodies, Arch. Rat. Mech. Anal., 27, 1–32.

Nye, J. F., 1953. Some geometric relations in dislocated crystals. Acta Metall., 1, 153–162.

Ortiz, M., Repetto, E. A., Stainier, L., 2000. A theory of dislocation structures. J. Mech. Phys. Solids, 48, 2077–2114.

Rice, J., 1971. Inelastic constitutive relations for solids: an internal-variable theory and its application to metal plasticity. J. Mech. Phys. Solids, 19, 433–455.

Shizawa, K., Zbib, H. M., A thermodynamical theory of gradient elastoplasticity with dislocation density tensor, I. Fundamentals, Int. J. Plast., 15, 899–938.

Shu, J. Y., Fleck, N. A., 1999. Strain gradient crystal plasticity: size-dependent deformation of bicrystals, J. Mech. Phys. Solids, 47, 297–324.

Šilhavý, M., 1997. The Mechanics and Thermodynamics of Continuous Media, Springer Verlag.

Steinmann, P., 1996. Views on multiplicative elastoplasticity and the continuum theory on dislocations. Int. J. Engng. Sci., 34, 1717–1735.

Stelmashenko, N.A., Walls, M.G., Brown, L.M., and Milman Y.V., 1993. Microindentations on W and Mo oriented single crystals: an STM study. Acta Metall. Mater., 41, 2855–2865.

Stölken, J.S., Evans, A.G., 1998. A microbend test method for measuring the plasticity length scale, Acta Mater., 46, 5109–5115.

Sun, S., Adams, B.L., Shet, C., Saigal, S., King, W., 1998. Mesoscale investigation of the deformation field of an aluminum bicrystal. Scripta Mater., 39, 501–508.

Svendsen, B., 1999. On the thermodynamics of isotropic thermoelastic materials with scalar internal degrees of freedom, Cont. Mech. Thermodyn., 11, 247–262.

Svendsen, B., 2000. Continuum thermodynamic extensions of crystal plasticity to include the effects of geometrically-necessary dislocations on the material behaviour. Rend. Sem. Mat. Univ. Pol. Torino, 58, 209–235.

Svendsen, B., 2001. On the modeling of anisotropic elastic and inelastic material behaviour at large deformation, Int. J. Solids Structs., 38, 9579–9599.

Svendsen, B., 2002. Continuum thermodynamic models for crystal plasticity including the effects of geometrically-necessary dislocations, J. Mech. Phys. Solids, 50, 1297-1329.

Svendsen, B., Reese, S., 2003. Continuum thermodynamic modeling and simulation of additional hardening due to deformation incompatibility, in Computational Mechanics of Solid Materials at Large Strains, C. Miehe, editor, pp. 141-150, Kluwer Series on Solids Mechanics and Its Application, Volume 108, Kluwer.

Svendsen, B., 2004. Phase-field extension of crystal plasticity with application to hardening modeling, in Continuum Scale Simulation of Engineering Materials: Fundamentals - Microstructures - Process Applications, D. Raabe, L.-Q. Chen, F. Barlat, F. Roters, L.-Q. Chen, (Editors), pp. 501-511, Wiley-VCH Verlag.

Yefimov S, Groma, I., Van der Giessen, E., 2004. A comparison of a statistical-mechanics based plasticity model with discrete dislocation plasticity calculations, J. Mech. Phys. Solids, 52 279–300.

Zaiser, M., Miguel, M.C., Groma, I., 2001. Statistical dynamics of dislocation systems: the influence of dislocation-dislocation correlation. Phys. Rev., 64, 224102–224111.

Chapter 3

Application to crack tip*

Abstract– In this work, the influence of the development of geometrically-necessary dislocations (GNDs) at a crack tip in single crystals on the hardening and crack propagation behaviour is investigated. In particular, we are interested in examining the effect of such additional hardening on the development of glide and kink bands at the crack tip as well as on the process of crack opening. To this end, following Nye and many others, local deformation incompatibility in the material is adopted as a measure of the density of GNDs. Their development results in additional energy being stored in the material, leading to additional kinematic-like hardening. A thermodynamic formulation of the model in the context of the dissipation principle facilitates the derivation of the corresponding hardening relation. Results suggest that this additional hardening retards kink-band development, but has little or no influence on glide-band development. It also influences the crack tip opening displacement (CTOD). It turns out that the simulated CTOD correlates well with experimentally-determined crack-propagation rates for different crack growth directions in the crystal.

3.1 Introduction

Standard micromechanical modeling of the inelastic material behaviour of metallic single crystals and polycrystals (*e.g.*, Hill and Rice, 1972; Asaro, 1983; Cuitino and Ortiz, 1992) is commonly based on the premise that resistance to glide is due mainly to the random trapping of mobile dislocations during locally homogeneous deformation. Such dislocations are generally known as statistically stored dislocations (SSDs), and act as obstacles to further dislocation motion, resulting in hardening. As anticipated in the work of Nye (1953) and Kröner (1960), and discussed by Ashby (1970), an additional contribution to the density of immobile dislocations and so to hardening can arise when the continuum lengthscale (*e.g.*, grain size) approaches that of the dominant microstructural features (*e.g.*, mean spacing between precipitates relative to the precipitate size, or mean spacing between glide planes). Indeed, in this case, the resulting deformation incompatibility between, *e.g.*, “hard” inclusions and a “soft” matrix, is accomodated by the development of so-called geometrically-necessary dislocations (GNDs). Experimentally observed effects in a large class of materials such as increasing material hardening with decreasing (grain) size (*i.e.*, the Hall-Petch effect) are commonly associated with the development of such GNDs.

These and other experimental results have motivated a number of workers over the last few years to formulate various extensions to existing local models for phenomenological plasticity, some of which have been applied to crystal plasticity (see reviews in Forest *et al.* (2002) or in Svendsen (2002)). In the current work, we pursue one application of such modeling pertaining

---

[1] published 2005 in *Computational Material Science* under the title:
”Application of extended crystal plasticity to the modeling of glide and kink bands and of crack opening in single crystals”.

to kink and glide band development at a crack tip in single crystals. In particular, the modeling of such bands using a micropolar Cosserat model Forest *et al.* (2001) for lattice rotation as additional continuum degree or freedom implies that lattice curvature develops at kink band boundaries but not at slip bands. As such, additional hardening due to GNDs retards kink, but not slip, band development at a crack tip. The purpose of this work is to study such kink and glide band development at a crack tip in single crystals using a continuum thermodynamic extension of crystal plasticity (*e.g.*, Svendsen, 2002; Levkovitch *et al.*, 2005) to include the effects of lengthscale-dependendent inelastic processes such as GNDs (and more generally dislocation substructure) development on the macroscopic material behaviour and crack development. In addition, the approach is used to model crack propagation for different crystal orientation using the crack tip opening displacement (CTOD) as the correlation parameter. As it turns out, the corresponding simulation results agree well with experiment.

3.2 Model formulation

As usual, in the context of phenomenological crystal plasticity, any material element of a material body is endowed with a set of s glide systems. The geometry and orientation of each such glide system is described as usual by an orthonormal basis $(\boldsymbol{s}_\mathfrak{a}, \boldsymbol{n}_\mathfrak{a}, \boldsymbol{t}_\mathfrak{a})$ ($\mathfrak{a} = 1, \ldots, s$). Here, $\boldsymbol{s}_\mathfrak{a}$ represents the direction of glide in the plane, $\boldsymbol{n}_\mathfrak{a}$ the glide-plane normal, and $\boldsymbol{t}_\mathfrak{a} = \boldsymbol{s}_\mathfrak{a} \times \boldsymbol{n}_\mathfrak{a}$ the direction transverse to $\boldsymbol{s}_\mathfrak{a}$ in the glide plane. Since we neglect in this work the effects of any processes involving a change in or evolution of either the glide direction $\boldsymbol{s}_\mathfrak{a}$ or the glide system orientation $\boldsymbol{n}_\mathfrak{a}$ (*e.g.*, texture development), these referential unit vectors, and so $\boldsymbol{t}_\mathfrak{a}$ as well, are assumed constant with respect to the reference configuration. With respect to the glide-system geometry, then, the (local) deformation of each glide system takes the form of a simple shear. From a phenomenological point of view, the basic local inelastic deformation at each material point in the material body in question is represented by an invertible second-order tensor field $\boldsymbol{F}_\mathrm{P}$. As usual, the evolution of this field is given by

$$\dot{\boldsymbol{F}}_\mathrm{P} = \sum\nolimits_\mathfrak{a} \dot{\gamma}_\mathfrak{a} (\boldsymbol{s}_\mathfrak{a} \otimes \boldsymbol{n}_\mathfrak{a}) \boldsymbol{F}_\mathrm{P} \tag{3.1}$$

in the context of crystal plasticity. On the basis of $\boldsymbol{F}_\mathrm{P}$, the continuum theory of dislocations (*e.g.*, Nye, 1953; Kröner, 1960) works with the effective Burgers-vector-like measure

$$\boldsymbol{l}_\mathrm{G}(C) := \oint_C \boldsymbol{F}_\mathrm{P}\, \boldsymbol{t}_C \;=\; \int_S (\mathrm{curl}\, \boldsymbol{F}_\mathrm{P}) \boldsymbol{n}_S \tag{3.2}$$

whose magnitude is interpreted as of the net length of GNDs in the material around any material curve C enclosing the material surface S in a body without singular surface. This measure involves the incompatibility $\mathrm{curl}\, \boldsymbol{F}_\mathrm{P}$ of the local inelastic deformation $\boldsymbol{F}_\mathrm{P}$ or Nye dislocation tensor. In particular, the phenomenological GND model of Dai and Parks (1997), utilized by them to model grain-size effects in polycrystalline metals, applied as well recently in Busso *et al.* (2000) to model size effects in nickel-based superalloys, is of this type. In a different context, the incompatibility of $\boldsymbol{F}_\mathrm{P}$ has also been used recently in Ortiz *et al.* (2000) to model in an effective fashion the contribution of the dislocation self- or core energy to the total free energy of ductile single crystals. Note that the evolution relation (3.1) for $\boldsymbol{F}_\mathrm{P}$ induces the glide-system decomposition

$$\boldsymbol{l}_\mathrm{G}(C) = \sum\nolimits_\mathfrak{a} l_{\mathrm{G}\mathfrak{a}}(C)\, \boldsymbol{s}_\mathfrak{a} \tag{3.3}$$

of $\boldsymbol{l}_{\mathrm{G}}(C)$ in terms of the set $l_{\mathrm{G}1}(C)$, . . ., of glide-system GND lengths with respect to C, where

$$\dot{l}_{\mathrm{G}\mathfrak{a}}(C) = \oint_C \dot{\gamma}_{\mathfrak{a}} \boldsymbol{F}_{\mathrm{P}}^{\mathrm{T}} \boldsymbol{n}_{\mathfrak{a}} \cdot \boldsymbol{t}_C \quad . \tag{3.4}$$

Alternatively, the evolution of $\boldsymbol{l}_{\mathrm{G}}(C)$ can be expressed at the glide-system level with respect to the measure

$$\dot{\boldsymbol{g}}_{\mathrm{G}\mathfrak{a}} = b^{-1}\,\nabla\dot{\gamma}_{\mathfrak{a}} \times \boldsymbol{F}_{\mathrm{P}}^{\mathrm{T}} \boldsymbol{n}_{\mathfrak{a}} + b^{-1}\,(\mathrm{curl}\,\boldsymbol{F}_{\mathrm{P}})^{\mathrm{T}} \boldsymbol{n}_{\mathfrak{a}}\,\dot{\gamma}_{\mathfrak{a}} \tag{3.5}$$

of surface GND density in the context of (3.2), such that

$$\overline{\mathrm{curl}\,\boldsymbol{F}_{\mathrm{P}}}^{\,\cdot} = b \sum\nolimits_{\mathfrak{a}} \boldsymbol{s}_{\mathfrak{a}} \otimes \dot{\boldsymbol{g}}_{\mathrm{G}\mathfrak{a}} \quad . \tag{3.6}$$

Ignoring for example grain-boundary contributions to local inelastic incompatibility, such that $\boldsymbol{F}_{\mathrm{P}}$ is initially homogeneous, taking the curl of (3.1) and integrating the result in time yields the expression

$$\mathrm{curl}\,\boldsymbol{F}_{\mathrm{P}} = \sum\nolimits_{\mathfrak{a}} b\boldsymbol{s}_{\mathfrak{a}} \otimes \boldsymbol{g}_{\mathrm{G}\mathfrak{a}} \tag{3.7}$$

for the incompatibility of $\boldsymbol{F}_{\mathrm{P}}$ in terms of the characteristic Burgers' vector magnitude b and the set $(\boldsymbol{g}_{\mathrm{G}1},\ldots,)$ of vector-valued GND surface (number) densities determined by the evolution relation

$$\dot{\boldsymbol{g}}_{\mathrm{G}\mathfrak{a}} = b^{-1}\,\nabla\dot{\gamma}_{\mathfrak{a}} \times \boldsymbol{F}_{\mathrm{P}}^{\mathrm{T}} \boldsymbol{n}_{\mathfrak{a}} + \sum\nolimits_{\mathfrak{b}\neq\mathfrak{a}} (\boldsymbol{n}_{\mathfrak{a}} \cdot \boldsymbol{s}_{\mathfrak{b}})\,\boldsymbol{g}_{\mathrm{G}\mathfrak{b}}\,\dot{\gamma}_{\mathfrak{a}} \tag{3.8}$$

(Svendsen, 2002), with $\boldsymbol{n}_{\mathfrak{a}} \cdot \boldsymbol{s}_{\mathfrak{a}} = 0$ and $\sum_{\mathfrak{b}\neq\mathfrak{a}} := \sum_{\mathfrak{b}=1,\mathfrak{b}\neq\mathfrak{a}}$. On this basis, inhomogeneity in $\dot{\gamma}_{\mathfrak{a}}$ results in a contribution to glide-system self-hardening, *i.e.*, from the first term in (3.8). Resulting from interaction with other glide systems, the second term in this last expression represents a contribution to glide-system latent hardening. As implied by (3.2) and (3.7), the projection $\boldsymbol{g}_{\mathrm{G}\mathfrak{a}} \cdot \boldsymbol{n}_S$ of $\boldsymbol{g}_{\mathrm{G}\mathfrak{a}}$ onto any material surface S with unit normal $\boldsymbol{n}_S$ gives the (scalar) surface (number) density of such GNDs piercing S. As it turns out, one can use $\boldsymbol{g}_{\mathrm{G}\mathfrak{a}}$ to define the measure

$$g_{\mathrm{G}\mathfrak{a}} := |\boldsymbol{s}_{\mathfrak{a}} \cdot \boldsymbol{g}_{\mathrm{G}\mathfrak{a}}| + |\boldsymbol{t}_{\mathfrak{a}} \cdot \boldsymbol{g}_{\mathrm{G}\mathfrak{a}}| + |\boldsymbol{n}_{\mathfrak{a}} \cdot \boldsymbol{g}_{\mathrm{G}\mathfrak{a}}| \tag{3.9}$$

employed in essence by Dai and Parks (1997) to represent the total surface number density of GNDs associated with glide system $\mathfrak{a}$. In this context, the GNDs on a slip-system fall into one of three categories: the set of screw dislocations with tangent in the $\boldsymbol{s}_{\mathfrak{a}}$ direction, the set of edge dislocations with tangent in the $\boldsymbol{t}_{\mathfrak{a}}$ direction, and the set of edge dislocations with tangent in the $\boldsymbol{n}_{\mathfrak{a}}$ direction, whereby the Burgers vectors of all 3 are in the $\boldsymbol{s}_{\mathfrak{a}}$ direction.

The above local deformation and dislocation measures have been used in Svendsen *et al.* (2001) and Levkovitch *et al.* (2005) to extend the Cailletaud model Meric *et al.* (1991) for crystal plasticity to the case of additional hardening due to GNDs. In particular, this extension is based on the form

$$\begin{aligned} \psi &= \tfrac{1}{2}\,\boldsymbol{E}_{\mathrm{E}} \cdot \mathsf{C}_{\mathrm{E}}\,\boldsymbol{E}_{\mathrm{E}} \\ &+ \tfrac{1}{2}\sum\nolimits_{\mathfrak{a}} \mu\,\epsilon_{\mathfrak{a}}^2 + \tfrac{1}{2}\sum\nolimits_{\mathfrak{a}} c_{\mathfrak{a}}\,\alpha_{\mathfrak{a}}^2 \\ &+ \tfrac{1}{2}\,\mu\,\ell^2\,|\mathrm{curl}\,\boldsymbol{F}_{\mathrm{P}}|^2 \end{aligned} \tag{3.10}$$

for the free energy density ψ. Here, C_{E} represents the referential elasticity tensor, $\boldsymbol{E}_{\mathrm{E}} := \frac{1}{2}(\boldsymbol{C}_{\mathrm{E}} - \boldsymbol{I})$ the elastic Green strain determined by the corresponding right Cauchy-Green tensor $\boldsymbol{C}_{\mathrm{E}} := \boldsymbol{F}_{\mathrm{P}}^{-\mathrm{T}} \boldsymbol{C}\,\boldsymbol{F}_{\mathrm{P}}^{-1}$, with $\boldsymbol{C} = \boldsymbol{F}^{\mathrm{T}}\boldsymbol{F}$ the right Cauchy-Green deformation, and $\boldsymbol{F}$ the deformation gradient. Further, $r_{\mathfrak{a}0}$ represents the initial glide-system yield stress, μ the shear modulus, and

$\epsilon_{\mathfrak{a}} := b\sqrt{n_{\mathfrak{a}}}$ a non-dimensional effective dislocation density associated with isotropic hardening. In particular, in the Dai and Parks case, we have

$$n_{\mathfrak{a}} \equiv \rho_{\mathrm{S}\mathfrak{a}} + g_{\mathrm{G}\mathfrak{a}} \quad , \tag{3.11}$$

and otherwise

$$n_{\mathfrak{a}} \equiv \rho_{\mathrm{S}\mathfrak{a}} \quad , \tag{3.12}$$

$\rho_{\mathrm{S}\mathfrak{a}}$ being the standard SSD density. Further, $c_{\mathfrak{a}}$ is the linear hardening modulus for constitutive glide-system kinematic hardening, and $\alpha_{\mathfrak{a}}$ the corresponding equivalent back strain. Lastly, ℓ represents a characteristic lengthscale for deformation incompatibility in the material. Beyond the stress, the free energy density ψ determines the quantities

$$\begin{aligned} x_{\mathfrak{a}} &= \psi_{,\alpha_{\mathfrak{a}}} &= c_{\mathfrak{a}}\,\alpha_{\mathfrak{a}}\,, \\ r_{\mathfrak{a}} &= \psi_{,\epsilon_{\mathfrak{a}}} &= \mu\,\epsilon_{\mathfrak{a}}\,, \end{aligned} \tag{3.13}$$

representing contributions to the glide-system back- and yield stresses, respectively.

The model is completed by the evolution relations for the remaining internal variables. In particular, the evolution of the glide-system effective SSD dislocation density $\epsilon_{\mathrm{S}\mathfrak{a}} := b\sqrt{\rho_{\mathrm{S}\mathfrak{a}}}$ is given by

$$\dot{\epsilon}_{\mathrm{S}\mathfrak{a}} = \beta_{\mathfrak{a}} \left\{ \frac{r_{\mathfrak{a}0} + q_{\mathfrak{a}}}{\mu} - \epsilon_{\mathrm{S}\mathfrak{a}} \right\} \dot{\nu}_{\mathfrak{a}} \tag{3.14}$$

in the context of the Cailletaud model. Here, $q_{\mathfrak{a}}$ and $\beta_{\mathfrak{a}}$ represent material parameters for isotropic self-hardening, and $\nu_{\mathfrak{a}}$ represents the accumulated glide-system slip, *i.e.*,

$$\dot{\nu}_{\mathfrak{a}} := |\dot{\gamma}_{\mathfrak{a}}| \quad . \tag{3.15}$$

The evolution relation for the back strain $\alpha_{\mathfrak{a}}$ is given by the Armstrong-Frederick form

$$\dot{\alpha}_{\mathfrak{a}} = \dot{\gamma}_{\mathfrak{a}} - d_{\mathfrak{a}}\,\alpha_{\mathfrak{a}}\,\dot{\nu}_{\mathfrak{a}} \quad , \tag{3.16}$$

again in the context of the Cailletaud model. Here, the saturation parameter $d_{\mathfrak{a}}$ mediates dynamic recovery.

On the basis of the above relations, the formulation of the generalized flow rule follows via the approach described in Svendsen (2000) leading to a field relation for the glide-system slips having a generalized Ginzburg-Landau or Cahn-Allen form. In the current context, this relation simplifies to that

$$\dot{\gamma}_{\mathfrak{a}} = \left\langle \frac{|\sigma_{\mathfrak{a}}| - r_{\mathfrak{a}}}{k_{\mathfrak{a}}} \right\rangle^{n_{\mathfrak{a}}} \operatorname{sgn}(\sigma_{\mathfrak{a}}) \tag{3.17}$$

for the glide-system flow rule and evolution of $\gamma_{\mathfrak{a}}$. Here, $\langle x \rangle \ := \ \frac{1}{2}\,(x + |x|)$ represents the ramp function, and $\sigma_{\mathfrak{a}}$ the effective driving stress for dislocation motion in the glide systems. In particular, we have

$$\sigma_{\mathfrak{a}} \equiv -\boldsymbol{s}_{\mathfrak{a}} \otimes \boldsymbol{n}_{\mathfrak{a}} \cdot \psi_{,\boldsymbol{F}_{\mathrm{P}}} \boldsymbol{F}_{\mathrm{P}}^{\mathrm{T}} - x_{\mathfrak{a}} \tag{3.18}$$

for $\sigma_{\mathfrak{a}}$ in the standard case, with the first term here representing the Schmid stress. Analogously, one obtains the result

$$\sigma_{\mathfrak{a}} \equiv = -\boldsymbol{s}_{\mathfrak{a}} \otimes \boldsymbol{n}_{\mathfrak{a}} \cdot (\psi_{,\boldsymbol{F}_{\mathrm{P}}} + \operatorname{curl}\psi_{,\operatorname{curl}\boldsymbol{F}_{\mathrm{P}}}) \boldsymbol{F}_{\mathrm{P}}^{\mathrm{T}} - x_{\mathfrak{a}} \tag{3.19}$$

for this stress in the extended thermodynamic formulation in which there is an additional contribution $\boldsymbol{s}_{\mathfrak{a}} \cdot \operatorname{curl} \psi_{,\operatorname{curl} \boldsymbol{F}_{\mathrm{P}}} \boldsymbol{F}_{\mathrm{P}}^{\mathrm{T}} \boldsymbol{n}_{\mathfrak{a}}$ to glide-system back stress from energy storage due to deformation incompatibility. This completes the model formulation.

In summary, in the Dai and Parks approach, the effect of GNDs on hardening is assumed to be isotropic in nature via (3.11), with the thermodynamic driving force for dislocation motion being given by (3.18). On the other hand, in the current extended thermodynamic approach, isotropic hardening as based on (3.12) is due solely to SSDs. Indeed, the GND contribution via (3.19) is here kinematic in nature and leads to a reduction in the effective thermodynamic driving force for dislocation motion. Beyond the hardening modeling itself, a major distinction between the two approaches is the fact that the Dai and Parks measure $g_{\mathrm{G}\mathfrak{a}}$ takes in a sense only a single glide-system into account, whereas $|\operatorname{curl} \boldsymbol{F}_{\mathrm{P}}|$ includes contributions from all such systems.

The above model has been implemented in the commercial finite-element code ABAQUS via the user-material (UMAT) and user-element (UEL) interfaces. This implementation involves in particular the numerical evaluation of the first and second spatial derivatives of the glide-system slip $\gamma_{\mathfrak{a}}$. Indeed, in the context of the Dai and Parks approach, the flow stress $r_{\mathfrak{a}}$ given by $(3.13)_2$ depends implicitly on the first spatial derivatives of $\gamma_{\mathfrak{a}}$ via (3.9), (3.11) and the flow rule (3.17). Analogously, the effective stress measure $\sigma_{\mathfrak{a}}$ in the form (3.19) depends implicitly on the second spatial derivatives of $\gamma_{\mathfrak{a}}$ via its dependence on $\operatorname{curl}(\operatorname{curl} \boldsymbol{F}_{\mathrm{P}})$. In the context of continuum crystal plasticity, both of these cases lead in general to the treatment of the glide-system slips $\gamma_{\mathfrak{a}}$ as additional continuum degrees-of-freedom (*e.g.*, Svendsen, 1999; Gurtin, 2000; Svendsen, 2000; Gurtin, 2002; Svendsen, 2002). Since we are interested here solely in the additional hardening effects, however, these spatial derivatives are evaluated numerically. In particular, using bilinear elements in the Dai and Parks case, and biquadratic elements for the general case, the spatial derivatives of the glide-system slips can be approximated within an element using the values at the Gauss points. With the values for the deformation incompatibility and so the non-local back stress determined in such a manner, the flow rule can be evaluated. On this basis, we now turn to a comparison of these two approaches in the context of the applications.

3.3 Glide- and kink-banding at a crack tip

Two types of strain localization bands are observed to develop in single crystals: slip bands parallel to the active slip plane and kink bands nearly perpendicular to the active slip plane (Figure 3.1).

In particular, kink bands form gradually by a progressive rotation of the lattice within a narrow region with respect to the rest of the crystal about an axis lying in the operative slip plane and perpendicular to the slip direction leading to the evolution of two well-defined kink planes AB and CD of severe lattice curvature which separate the kinked region from the unkinked rest of the crystal (Figure 3.2). To accommodate such local deformation inhomogeneity as lattice curvature, GNDs accumulate at kink-band boundaries. Because kink bands always require a strong lattice curvature and, thus, imply a high concentration of GNDs, formation of such bands is energetically less favorable than that of slip bands. That's, why slip bands are observed much more frequently than kink bands. In this regard, standard crystal plasticity does not distinguish between the different nature of slip and kink bands. Asaro and Rice (1979) performed a bifurcation analysis at large strains for elastoplastic single crystals undergoing single slip and found out that the both localization modes, corresponding to slip and kink banding, become possible for similar values of the critical hardening modulus. Thus, the classical crystal plastic-

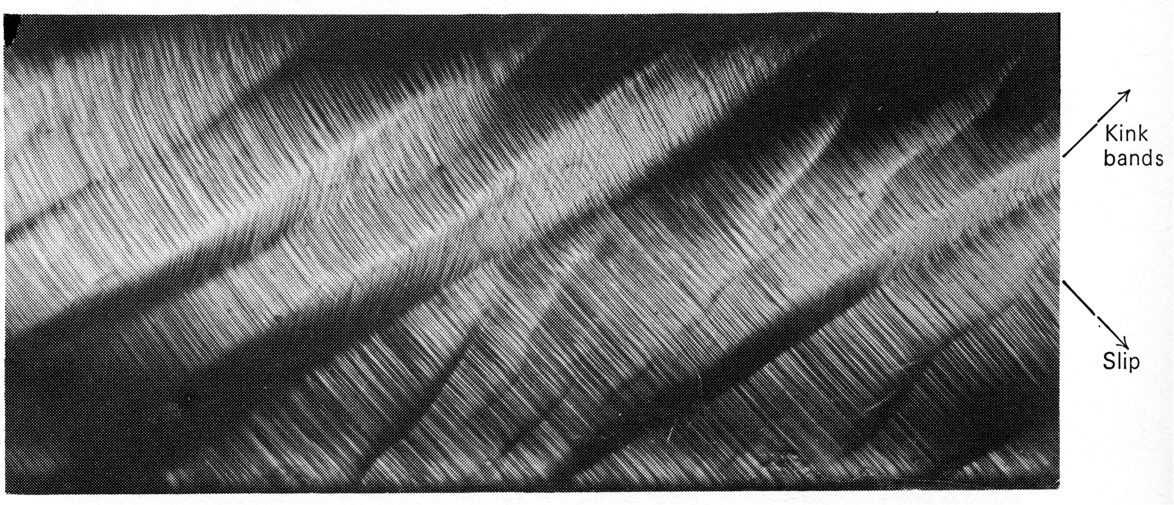

Figure 3.1: Kink bands in an aluminum crystal deformed 17.5 % in tension (after Honeycomge, 1968)

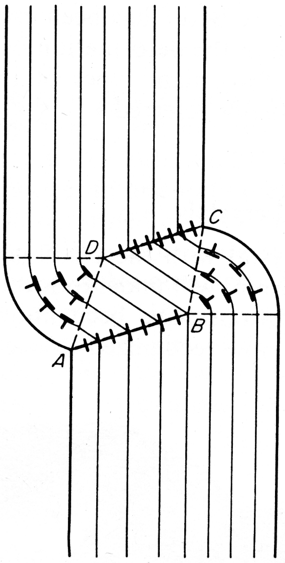

Figure 3.2: Dislocation distribution in a kinked crystal (after Honeycomge, 1968)

ity predicts similar resistance against the developing of the both types of shear bands in spite of their different nature.

Given the fact, that, while slip bands are associated with no lattice distortion, the development of kink bands requires strong lattice curvature, which is tantamount to high concentration of GNDs, it seems to be essential to incorporate an additional hardening either directly by virtue of lattice curvature or due to an appropriate measure of GNDs, into the material description, in order to account for different energetic statuses of slip and kink bands. So, it has been shown in Forest *et al.* (2001) that, using the Cosserat model with the lattice rotation as an additional degree of freedom, the development of kink bands can be made more difficult without affecting slip bands. Our goal is to investigate what measure of GNDs will have a similar effect (reducing the intensity of kink bands without influencing slip bands). To this end we compare simulation

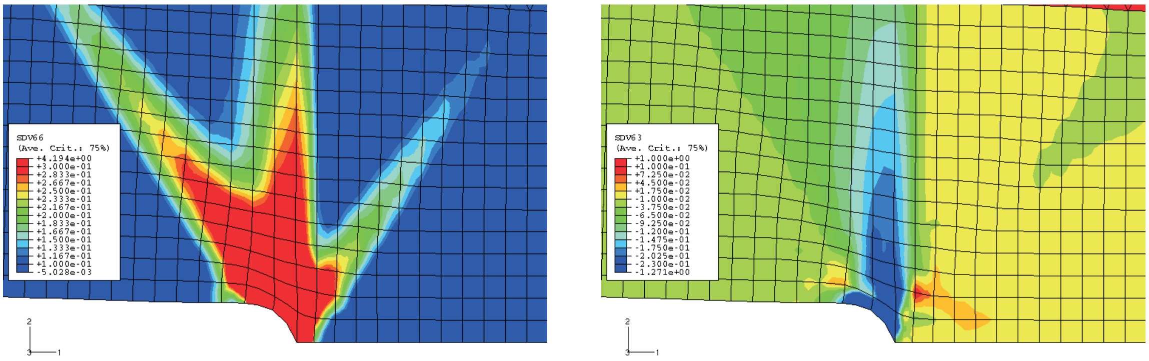

Figure 3.3: Results for (001)[110], local model: a) total accumulated slip $\sum \nu_\alpha$ (left), b) lattice rotation (right)

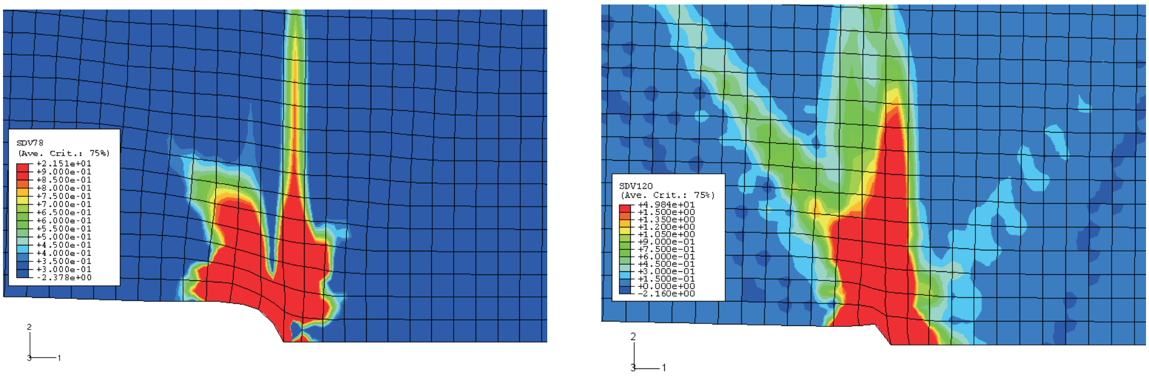

Figure 3.4: Results for (001)[110], local model: a) $|\mathrm{Curl}\, \boldsymbol{F}_{\mathrm{P}}|$ (left), b) Dai and Park's GND measure (right)

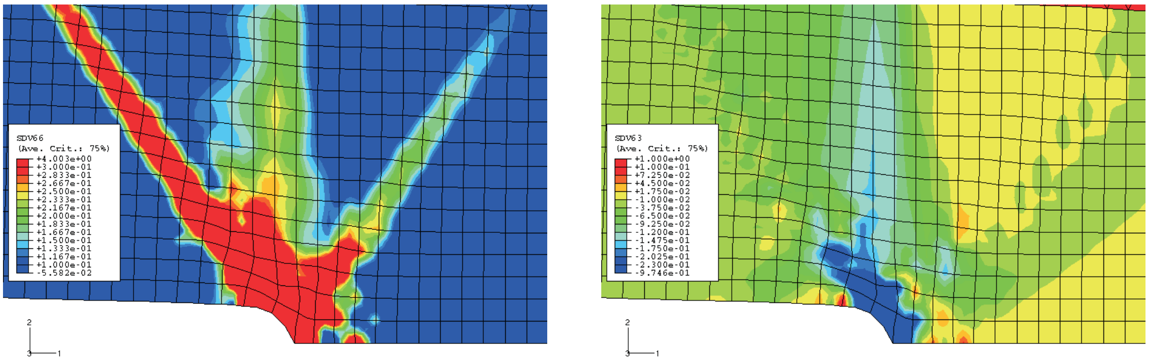

Figure 3.5: Results for (001)[110], extended model: a) total accumulated slip $\sum \nu_\alpha$ (left), b) lattice rotation (right)

results from the continuum thermodynamic extension of crystal plasticity discussed in the previous section with those from the approach of Dai and Parks (1997), which has been applied in a number of works (*e.g.* Busso *et al.*, 2000) to the modeling of additional hardening due to GNDs.

More specifically, we examine in this section patterns of localized deformation arising at the

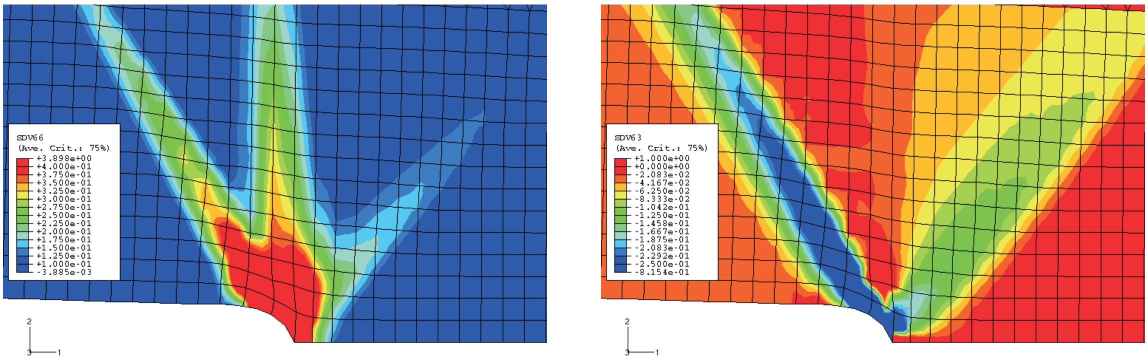

Figure 3.6: Results for (011)[100], local model: a) total accumulated slip $\sum \nu_\alpha$ (left), b) lattice rotation (right)

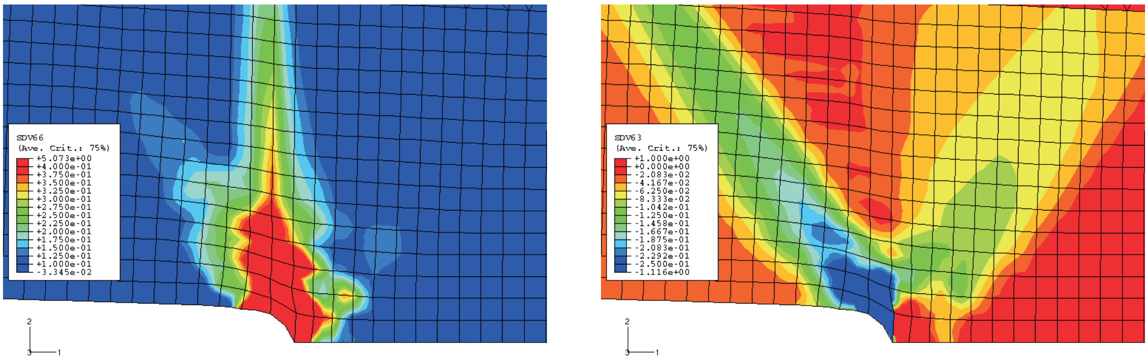

Figure 3.7: Results for (011)[100], extended model: a) total accumulated slip $\sum \nu_\alpha$ (left), b) lattice rotation (right)

tip of differently oriented cracks in C(T) (compact-tension) specimens of an fcc single crystal under plain strain conditions for loading mode I. Two different crystal orientations $(001)[110]$ and $(011)[100]$ in the CT specimen are considered. Here, the parentheses denote both the crack plane orientation and the loading direction because of mode I loading conditions, and brackets denote the initial crack growth direction. For the simulation, 12 octahedral slip systems are taken into account. The following material parameter values were chosen: $c_{11} = 182900$, $c_{22} = 125000$, $c_{44} = 91850$, $r_{\mathfrak{a}0} = 500$, $q_\mathfrak{a} = -30$, $c_\mathfrak{a} = 0$, $k_\mathfrak{a} = 100$ (all in MPa), as well as $\beta_\mathfrak{a} = 200$, $n_\mathfrak{a} = 5$, and $d_\mathfrak{a} = 0$. Lastly, $\mu\ell^2 = 20$ MPa mm^2 was assumed for the extended case. In particular, to trigger glide band development more quickly, slight isotropic softening is assumed here, as reflected in the negative value ($q_\mathfrak{a} = -30$) of $q_\mathfrak{a}$. Further, for simplicity, kinematic hardening beyond that associated with GND development is ignored here (*i.e.*, by assuming $c_\mathfrak{a} = 0$ and $d_\mathfrak{a} = 0$). As such, kinematic hardening is accounted for only in the extended case (*i.e.*, due to GND development).

The simulation results for crystal orientation $(001)[110]$ in the C(T)-specimen are represented in Figures 3.3 to 3.5. In what follows, the total accumulated slip is that for all glide systems, and the lattice rotation represents the rotation angle obtained from the elastic rotation $\boldsymbol{R}_\mathrm{E}$. In Figure 3.3, three glide bands are evident. The two bands lying at an angle are slip bands exhibiting little spatial variation in lattice rotation, whereas the vertical band is a kink band because of its strong lattice rotation (Figure 3.3). Consider next the GND density development. In the Dai and Parks case, these are represented by the ’crystallographic’ GND densities $g_{\mathrm{G}\mathfrak{a}}$ given by (3.9). In the current extended approach, the GND density is given by $|\mathrm{curl}\, \boldsymbol{F}_{\mathrm{P}}|$. As shown in Figure 3.4, $|\mathrm{curl}\, \boldsymbol{F}_{\mathrm{P}}|$ is larger in the kink band than in both slip bands, where it is practically zero. On the other hand, $g_{\mathrm{G}\mathfrak{a}}$ (Figure 3.4) is non-zero in all three bands. As such, the use of $g_{\mathrm{G}\mathfrak{a}}$ as a measure of additional hardening is expected to lead to the same degree of such hardening in both the kink and slip bands. The simulation results confirm this.

On the other hand, the extended thermodynamic model based on $\mathrm{curl}\, \boldsymbol{F}_{\mathrm{P}}$ as a measure of additional energy storage due to GND development predicts that these develop only in kink bands and so do not affect the hardening behaviour in slip bands. In particular, additional hardening due to increasing GND density in the kink bands then leads to significant reduction in the amount of plastic deformation developing in these, which must be then taken up by the slip bands (compare Figures 3.3 and 3.5). Note also that lattice rotation in the kink band in the extended case is reduced (Figure 3.5), implying less distortion of the crystal lattice.

The application of the local model to the crack orientation $(011)[100]$ results again in the development of three shear bands (Figure 3.6a). However, in this case the vertical one is a slip band (no lattice rotation) and the both inclined are kink bands due to strong lattice rotation (Figure 3.6b). And again the application of the extended model leads to a reduction in the intensity of the kink bands while letting the slip band unaffected (Figure 3.7).

It is interesting to note that the same glide band formation and lattice rotation development (Figure 3.5) is also predicted using the above-mentioned Cosserat model for single crystals in Forest *et al.* (2001), which assumes the lattice rotation directly as additional degree of freedom in the material.

3.4 Ductile crack propagation

Crack tip opening displacement (CTOD) is widely used in fracture mechanics as a correlation parameter for crack propagation. In anisotropic systems such as single crystals, CTOD is also expected to be sensitive to crack orientation with respect to the crystal. On the other hand, the standard viscoplastic modeling of strain-controlled cyclically-loaded round bar specimens of particle-reinforced fcc single-crystal SRR99 at 980°C carried out in Bauer *et al.* (2001) (Figure 3.8) showed no correlation between CTOD and the rate of crack propagation for (001)[100] and (001)[110] crack orientations. Indeed, in contrast to the experimental results, the simulated CTOD implied a larger CTOD for, and so faster crack propagation in, the (001) [110] direction. Similar experimental observations for crack propagation have been made in Ziebs and Frenz (1997) on the nickel superalloy SC16 at 650°C (Figure 3.9).

As shown by the results of the previous section, additional hardening due to deformation incompatibility can have a significant effect on glide-band formation, something that may influence such crack propagation as well. And indeed, it turns out that the extended model brings CTOD into agreement with experiment for sufficiently large values of the internal material lengthscale ℓ.

To look into this in more detail, simulations were carried out taking both the 12 octahedral as well as 6 cubic systems into account. From Bauer *et al.* (2001), the elastic constants are given by $c_{11} = 180000$, $c_{22} = 120000$ and $c_{44} = 93000$ (all in MPa). Further, for the octahedral systems, parameter values of $r_{\mathfrak{a}0} = 0$, $q_{\mathfrak{a}} = 0$, $c_{\mathfrak{a}} = 306510.9$ and $k_{\mathfrak{a}} = 527.4$ (all in MPa), as well as $\beta_{\mathfrak{a}} = 0$, $n_{\mathfrak{a}} = 7.6$, and $d_{\mathfrak{a}} = 2571.4$, were determined. Likewise, for the cubic systems, values of $r_{\mathfrak{a}0} = 0$, $k_{\mathfrak{a}} = 636.9$, $q_{\mathfrak{a}} = 0$, $c_{\mathfrak{a}} = 231658.2$ (all in MPa), as well as $\beta_{\mathfrak{a}} = 0$, $n_{\mathfrak{a}} = 3.41$, and

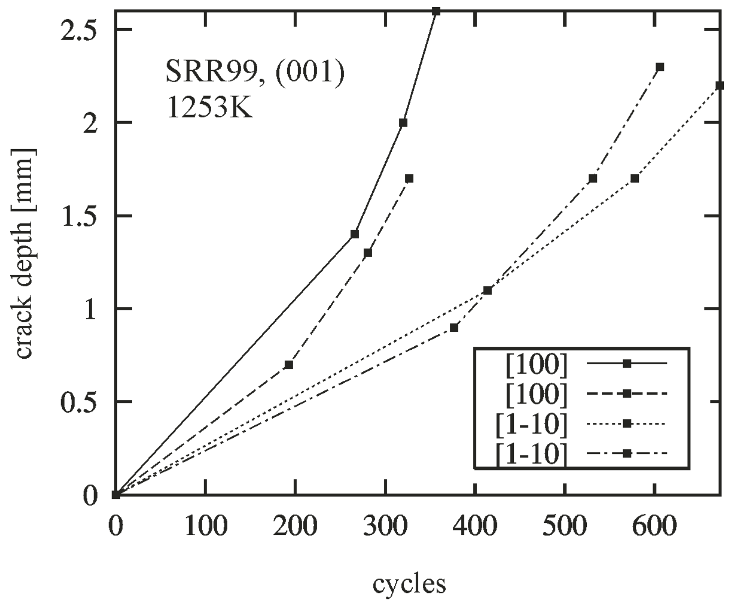

Figure 3.8: Crack length over number of cycles for two different crack orientations for a cyclically loaded specimen of single-crystal superalloy SRR99 at 980°C (after Bauer *et al.*, 2001)

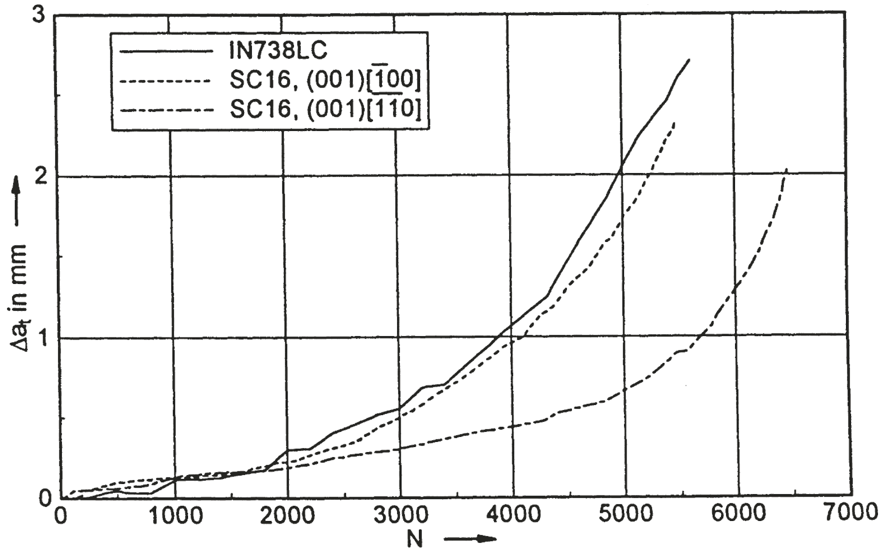

Figure 3.9: Crack length over number of cycles for two different crack orientations for a cyclically loaded specimen of single-crystal superalloy SC16 at 650°C (after Ziebs and Frenz, 1997)

$d_{\mathfrak{a}} = 1569.5$, were determined. Lastly, the extended simulations were carried out for $\mu\ell^2 = 40$ MPa mm^2.

The simulation results for the CTOD obtained with the standard Cailletaud model (Figure 3.10) as based on (3.11) and (3.18) show more vertical displacement of the nodes at the crack tip in the (001)[110] direction than in the (001)[100], implying a higher growth rate. This is in contrast to the experimental results, where the growth rate is larger in the latter direction. On the other hand, in the extended Cailletaud case (Figure 3.12) as based on (3.12) and (3.19), the CTOD (and so the growth rate) is larger in the (001)[100] direction, in agreement with experi-

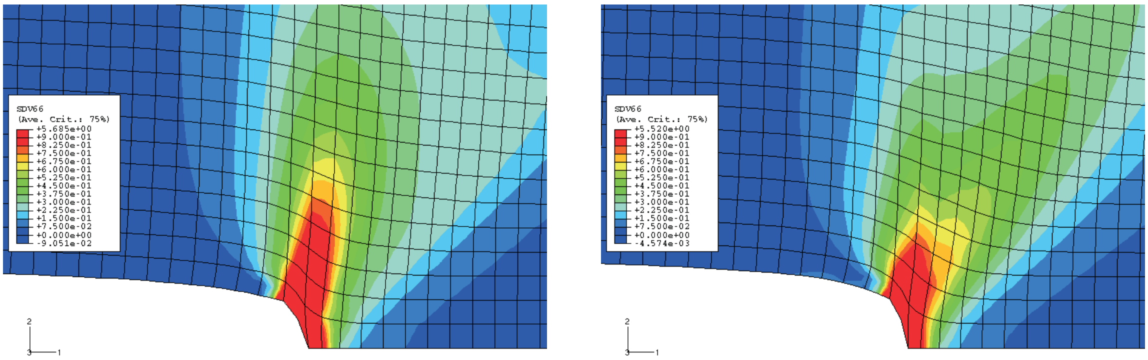

Figure 3.10: Results for total accumulated slip, local model: a) for (001)[100] (left), b) for (001)[110] (right)

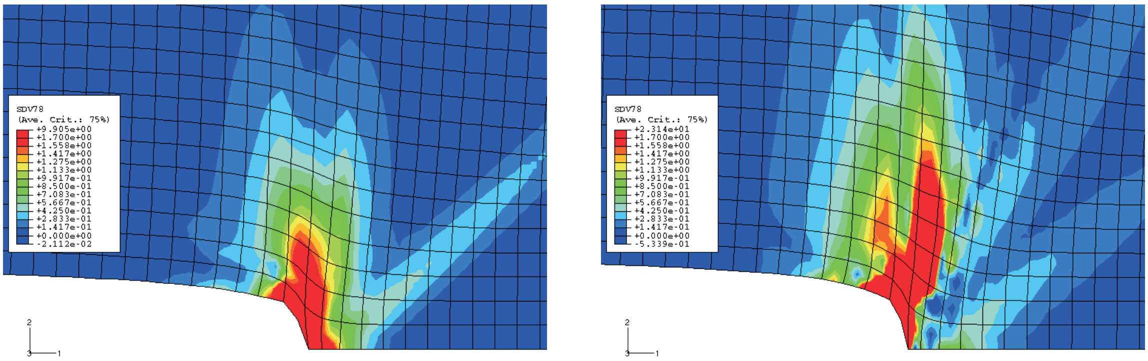

Figure 3.11: Results for $|\mathrm{Curl}\,\boldsymbol{F}_{\mathrm{P}}|$, local model: a) for (001)[100] (left), b) for (001)[110] (right)

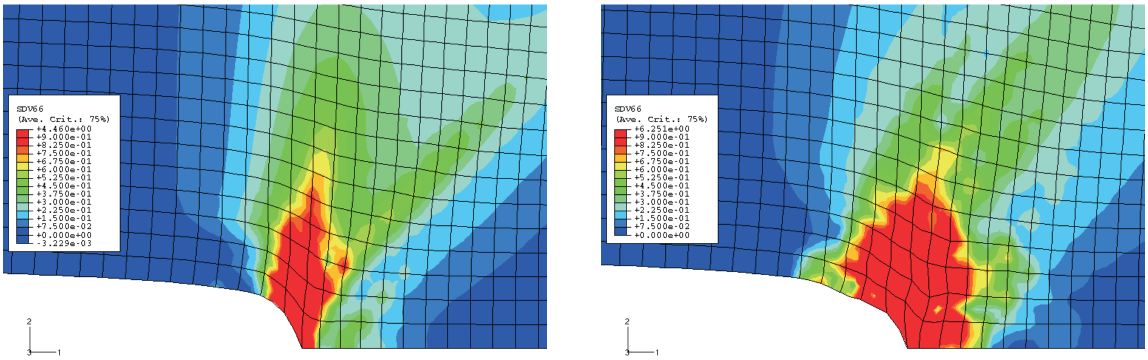

Figure 3.12: Total accumulated slip, extended model: a) for (001)[100] (left), b) for (001)[110] (right)

ment (Ziebs and Frenz, 1997; Bauer *et al.*, 2001). These results are corroborated by those for the crack-tip GND density, which is higher in the (001)[110] direction (Figure 3.11), implying that stronger additional hardening occurs in this orientation, resulting in reduced inelastic deformation and a corresponding reduction in the CTOD.

3.5 Acknowledgment

We thank a reviewer of the first version of this work for helpful comments leading to its improvement. Thanks also go to Bernard Federlich for the initial impetus to apply the extended crystal plasticity approach to crack propagation in single crystals and for useful discussions.

References

Asaro, R. J., Rice, J. R., 1979. Strain localization in ductile single crystals. J. Mech. Phys. Solids 25, 309–338.

Asaro, R. J., 1983. Micromechanics of crystals and polycrystals. Adv. Appl. Mech. 23, 1–115.

Ashby, M. F., 1970. The deformation of plastically non-homogeneous materials. Phil. Mag. 21, 399–424.

Bauer, G., Bogel, B., Fedelich, B., Klingelhöffer, H., Olschewski, J., Österle, W., Schmidt, B., 2001. Development of microcracks in single-crystal alloys during LCF-loading at high temperature (in german). Report BAM-V.2 01/7, Federal Institute for Materials Research and Testing (BAM), Berlin, Germany.

Busso, E. F., Meissonnier, F. T., O'Dowd, N. P., 2000. Gradient-dependent deformation of two-phase single crystals. J. Mech. Phys. Solids 48 (2000), 2333–2361.

Cuitiño, A. M., Ortiz, M., 1992. Computational modeling of single crystals. Modelling Simul. Mater. Sci. Eng. 1, 225–263.

Dai, H., Parks, D. M., 1997. Geometrically-necessary dislocation density and scale-dependent crystal plasticity. Proceedings of Plasticity'97, A. S. Khan, editor, pp. 17-18.

Forest, S., Boubidi, P., Sievert, R., 2001 Strain localization patterns at a crack tip in generalized single crystal plasticity. Scripta mater. 44, 953–958.

Forest, S., Sievert, R., Aifantis, E. C., 2002. Strain gradient crystal plasticity: thermodynamical formulations and applications. J. Mech. Beh. Mat. 13, 219-232.

Gurtin, M. E., 2000. On the plasticity of single crystals: free energy, microforces, plastic-strain gradients. J. Mech. Phys. Solids 48, 989–1036.

Gurtin, M. E., 2002. A theory of viscoplasticity that accounts for geometrically necessary dislocations. J. Mech. Phys. Solids 50, 5–32.

Hill, R., Rice, J. R., 1972. Constitutive analysis of elastic-plastic crystals at arbitrary strain, J. Mech. Phys. Solids 20, 401–413.

Honeycombe, R.W.K., 1968. The plastic deformation of metals. Edward Arnol (Publishers) Ltd., London.

Kröner, E., 1960. Allgemeine Kontinuumstheorie der Versetzungen und Eigenspannungen, Arch. Rat. Mech. Anal. 4, 273–334.

Levkovitch, V., Sievert, R., Svendsen, B., 2005. On the large-deformation- and continuum-based formulation of models for extended crystal plasticity. Sumbitted to Int. J. Solids Struct.

Meric, L., Poubanne, P., Cailletaud, G., 1991. Single crystal modeling for structural calculations: part 1 - model presentation. J. Engng. Mat. Technology 113, 162-170.

Nye, J. F., 1953. Some geometric relations in dislocated crystals. Acta Metall. 1, 153–162.

Ortiz, M., Repetto, E. A., Stainier, L., 2000. A theory of dislocation structures. J. Mech. Phys. Solids 48, 2077–2114.

Svendsen, B., 1999. On the thermodynamics of isotropic thermoelastic materials with scalar internal degrees of freedom. Cont. Mech. Thermodyn. 11, 247–262.

Svendsen, B., 2000. Continuum thermodynamic extensions of crystal plasticity to include the effects of geometrically-necessary dislocations on the material behaviour. Rend. Sem. Mat. Univ. Pol. Torino 58, 209–235.

Svendsen, B., 2002. Continuum thermodynamic models for crystal plasticity including the effects of geometrically-necessary dislocations. J. Mech. Phys. Solids 50, 1297-1329.

Svendsen, B., Olschewski, J., Sievert, R., 2001. Crystal-plasticity-based modeling and simulation of geometrically-necessary dislocations at a crack front in ductile single crystals, J. Phys. IV France 11, 171–177.

Ziebs, J., Frenz, H., 1997. Influence of polished surface properties on the fatigue crack propagation in IN 738 LC and SC 16 at 650°C. Final report of the Cooperative Research Center 339 on Turbine Blades and Disks, Technical University of Berlin, pp. D1 IV.

Chapter 4

Microscopic modeling of fatigue crack propagation*

Abstract– Laird and Smith (1962) proposed a plastic sliding-off mechanism for the stage II fatigue crack growth via striation formation. In their view, the fatigue crack extension results solely from the changing character of deformation at the crack tip during loading and unloading. In particular, the crack tip blunts during the loading stage and folds into a double notch during the unloading stage, resulting in striation formation. In order to verify Laird's plastic blunting mechanism for ductile polycrystals as well as for ductile fcc single crystals, FE calculations were performed for a rectangular plate with an initially sharp crack under plane strain conditions. The plate was subjected to a fully reversed tension-to-pressure cyclic load perpendicular to the crack plane (Mode 1). In the single crystal case the crack propagation simulations were carried out for cracks with crack plane (001) for two different crack growth orientations [110] and [100]. The shape of the crack tip followed from an initially sharp crack by repeated remeshing. To model the constitutive behavior typical for polycrystalline ductile metals, J_2 hypo-elasto-plasticity model with Armstrong-Frederick kinematic hardening was used. To model the constitutive behavior typical for ductile fcc single crystals, a geometrically nonlinear version of Cailletaud's model based on the multiplicative elasto-plastic decomposition of the deformation gradient was implemented into the FE program ABAQUS. Deformation patterns in the sense of Laird's mechanism for fatigue crack propagation with striation formation were obtained in the case of the polycrystal simulation as well as in the case of the single crystal simulation for [110] crack growth direction. The simulation for [100] crack growth direction with the same stress level as for [110] direction also yielded crack extension by progressive large deformations but without striation formation. The dependence of the fatigue striation formation on the crack growth direction as predicted by the simulation of crack propagation in single crystals is verified by the experimental results of Neumann (1974) on pure copper single crystals.

4.1 Introduction

In the case of cyclic loading, subcritical crack growth can occur if the stress intensity factor K is much lower than the fracture toughness K_c. For most engineering alloys, the total crack resistance curve (*i.e.*, plot of the crack growth rate da/dN versus the stress intensity factor range $\Delta K = K_\mathrm{max} - K_\mathrm{min}$ on the logarithmic scale) exhibits a sigmoidal shape in which three regimes can be distinguished. In regime A, the average crack growth per cycle is smaller than a lattice spacing. Further, there exists a threshold stress intensity factor range K_0 below which cracks remain dormant, and above which the crack growth rate increases with ΔK. Regime B, known as the Paris regime, shows a linear variation of $\log da/dN$ with $\log \Delta K$. Regime C pertains to the range of high ΔK values where the crack growth rate increases rapidly, causing

---

* accepted 2006 in *International Journal of Fracture* under the title:
"Simulation of fatigue crack propagation in ductile metals by blunting and re-sharpening".

catastrophic failure.

In ductile metals, regime B crack growth is controlled for the most part by a plastic sliding-off process at the tip of the advancing crack (Ritchie, 1999). The sliding-off mechanism associates crack extension with blunting of the crack tip during loading followed by re-sharpening upon unloading. The fatigue crack extension results solely from the changing nature of deformation at the crack tip during loading and unloading. This approach, which is usually used to explain fatigue crack growth via striation formation (ripples on the fracture surface), was first proposed by Laird and Smith (1962) for smooth blunting, and later by Neumann (1974) and Pelloux (1970) for blunting via alternating shear. For cyclic loads in the Paris regime, it has been found that the spacing between adjacent striations correlates with the experimentally measured average crack growth rate per cycle. Since plastic blunting implies crack growth due to the crack tip opening, the crack growth rate can be related to the cyclic crack tip opening displacement $da/dN \propto \Delta\mathrm{CTOD}$. Using a simple model for striation formation, McClintock (1967) obtained the following relation between CTOD and the stress intensity factor range

$$\frac{da}{dN} \propto \Delta\mathrm{CTOD} = \beta\frac{\Delta K^2}{2\sigma_0 E} \ ,$$

where σ_0 and E are the appropriate flow stress and Young's modulus, respectively, and β is a proportionality factor of order $0.1 - 0.5$, reflecting the efficiency of crack tip blunting and reversibility of slip. This approach provides a first-order description of crack growth rate behavior in the Paris regime (regime B) although it is an insufficient description at high growth rates and in the near-threshold regime. At high growth rates (Regime C) the above equation underestimates measured growth rates due to occurrence of monotonic fracture (static modes) mechanisms which replace or are additional to plastic sliding-off process. Such mechanisms include cleavage, intergranular cracking and microvoid coalescence.

To simulate crack growth by means of FE, different techniques have been proposed. The propagation of a crack in a structure leads to a displacement discontinuity. This can be dealt with using, *e.g.*, node release schemes (Bouchard *et al.*, 2003) or cohesive zone elements (Nguyen *et al.*, 2001). In the case of node release, the criterion for the crack propagation rate and direction are needed. Usually the crack extension per cycle is described in terms of the cyclic stress intensity factor range ΔK for small scale yielding or of the cyclic crack tip opening displacement $\Delta\mathrm{CTOD}$ for the case of large-scale yielding. To determine the crack growth direction, so called kinking criteria can be used (Bouchard *et al.*, 2003). These can be local criterion, that are based on local fields at the crack tip (*e.g.*, maximum strain criterion), or global criterion, that are based on the energy distribution throughout the cracked part (*e.g.*, maximum strain energy release rate). In the case of cohesive zone, special interface elements are introduced whose constitutive behavior is described by a special traction-separation law for cyclic loading (*e.g.*, Nguyen *et al.*, 2001). In this case, no criterion for the crack growth direction are needed because the failure behaviour is described now by a kind of local damage criterion. The most rigorous way to model numerically the crack propagation in ductile metals in Paris regime would be to simulate the plastic sliding-off process on the tip of an advancing crack. FE simulations of the crack propagation via smooth plastic blunting and re-sharpening (Laird and Smith, 1962) under cyclic loading have been described in Gu and Ritchie (1999) as well as in Tvergaard and Hutchinson (2002) for isotropic materials. These simulations were carried out for moderately large deformations at the crack tip for two and three cycles, respectively, in order to avoid severe distortions of the elements at the crack tip. No striations were obtained in these papers. Recently, Tvergaard performed in Tvergaard (2004) calculations for 200 cycles using repeated remeshing and an isotropic material model in order to investigate crack closure behaviour. Although Tvergaard used remeshing he also reports that no striations were obtained. As a possible reason for this, he suggests that the mesh at the crack tip is not fine enough.

In this work, we will investigate the possibility of predicting striation development in ductile poly- and single crystals. To this end, we simulate crack propagation by smooth plastic blunting and re-sharpening mechanism using J_2 elasto-plastic material model with Armstrong-Frederick kinematic hardening for polycrystals as well as Cailletaud's crystal plasticity material model for face centered cubic single crystals and repeated remeshing for severely distorted elements at the advancing crack tip. For single crystal simulations we will consider two different crack orientations [110] and [100] following Neumann (1974) experiments on copper single crystals.

4.2 Models for crack propagation via striation formation

The most frequent feature of the fatigue fracture surface is the presence of striations. These represent ripples on the fracture surface and are a unique characteristic of fatigue. Fatigue striations can be clearly or poorly delineated, and can take several shapes, from almost perfectly straight to very curved. The periodicity of the striations suggests a one-to-one correspondence of striations and loading cycles. This assumption has been verified in some materials by low-frequency cycling at two different stress levels, for a prescribed number of cycles at each level. On the fracture surface, it was then possible to distinguish zones of smaller (lower stress level) and larger striation spacing (higher stress level). The number of striations in zones was equal to the number of cycles at the given stress level, implying that one striation spacing is equal to the crack-length increase in one cycle. It offers means of determining fractographically crack propagation rates and comparing them with macroscopic measurements on the specimen surface. These two methods, *i.e.*, macroscopic and microscopic, have not always been found to yield the same results. The microscopic value of the crack rate is in some cases higher than the macroscopic one. This means that each striation is formed during one cycle, but each cycle does not necessarily result in formation of striations. Indeed, there are ”dead” cycles in which the crack does not propagate. As a rule, fatigue striations can be observed in Stage II crack propagation, when their spacing becomes sufficiently large (of the order of 100 nm or more).

A number of conceptual models have been proposed over the years to explain the formation of fatigue striations and the planar growth of Stage II fatigue cracks. Descriptive models of fatigue striations are based mainly on the micro-relief of the fracture surface and on the direct observation of crack-tip behavior at high strain amplitude, low frequency cycling. The existence of fatigue striations as a common feature of fatigue and of one-to-one correspondence (with some exceptions) between striations and stress cycles means that fatigue crack propagation is a repetitive process. To understand the crack propagation mechanism, it is sufficient to know the processes in one loading cycle.

In order to explain the crack growth via striation formation, Laird and Smith (1962) observed the development of the crack-tip geometry in some ductile metals corresponding to different stages of the stress cycle. The mechanism of crack propagation deduced from these observations is now known as plastic blunting or Laird's model (see Figure 4.1). The initial (zero) load corresponds to a well developed Stage II crack with the fracture surface exhibiting striations (a). As the tensile load is applied, the metal yields plastically due to high stress concentration. This plastic deformation is highly concentrated in the slip zones along the planes of maximum shear stress (b). When the load is further increased, the slip zones at the tip broaden and the crack tip blunts to a semicircular configuration. The crack tip thus is effectively shifted (c). If the

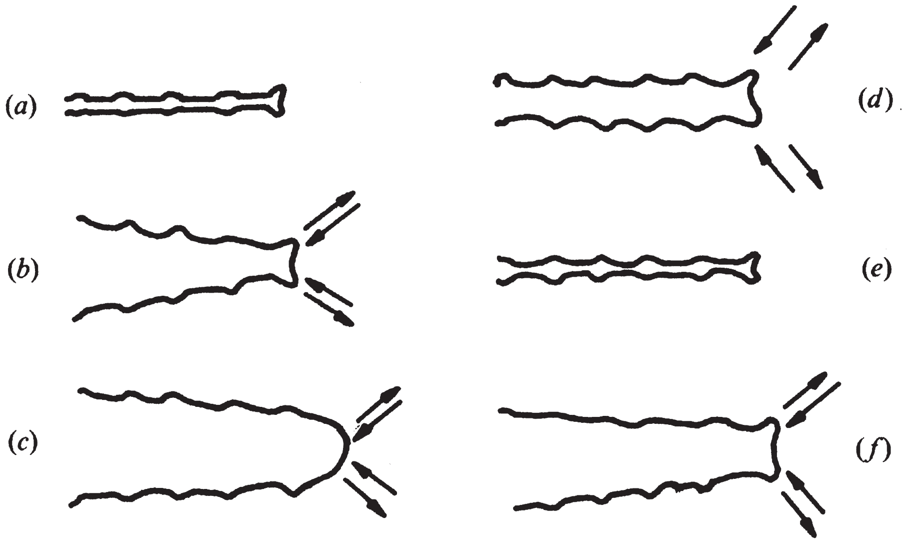

Figure 4.1: Laird's scheme for stage II crack propagation via plastic blunting and re-sharpening (Suresh, 1998).

far-field stress is reversed, the crack tip re-sharpens by buckling and folding of the new created surface into a double notch resulting in a striation formation (d) and (e). Since the closure of the crack during compression cannot fully negate the blunting and the attendant extension of the crack during the preceding tension load, net crack growth occurs during a fatigue cycle, leading to the formation of a striation with the striation spacing equal to the crack length increment.

This mechanism of repeated plastic blunting and resharpening of the crack tip is probably the most general descriptive model of fatigue crack propagation. Laird's mechanism explains in a compact way the formation of fatigue striations on the fracture surface. The model does not make any assumption about the dislocation mechanism at the crack tip, or about the relation between the substructure and the surface relief. This mechanism also works in polymers, where the plastic processes are very different from those in metals. The only prerequisite here is localized plastic (*i.e.*, irreversible) deformation at the crack tip. The lack of any specialized assumptions makes Laird's mechanism very attractive.

On the other hand, in ductile metal single crystals, fatigue crack propagation can be modelled

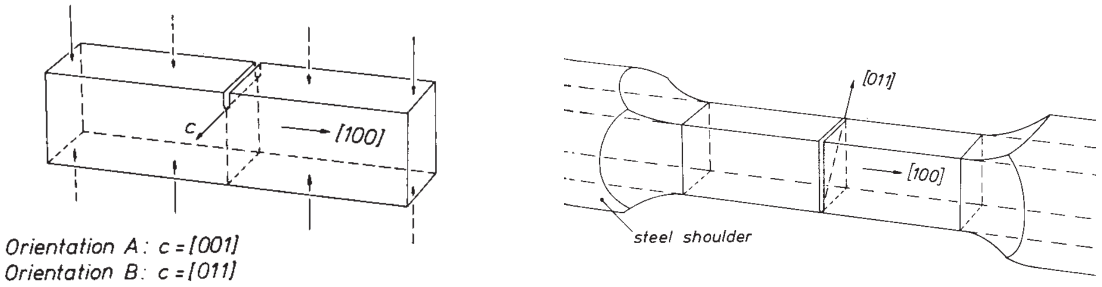

Figure 4.2: Geometry and orientation of the bending specimen (left) and of the push-pull specimen (right) (Neumann, 1974).

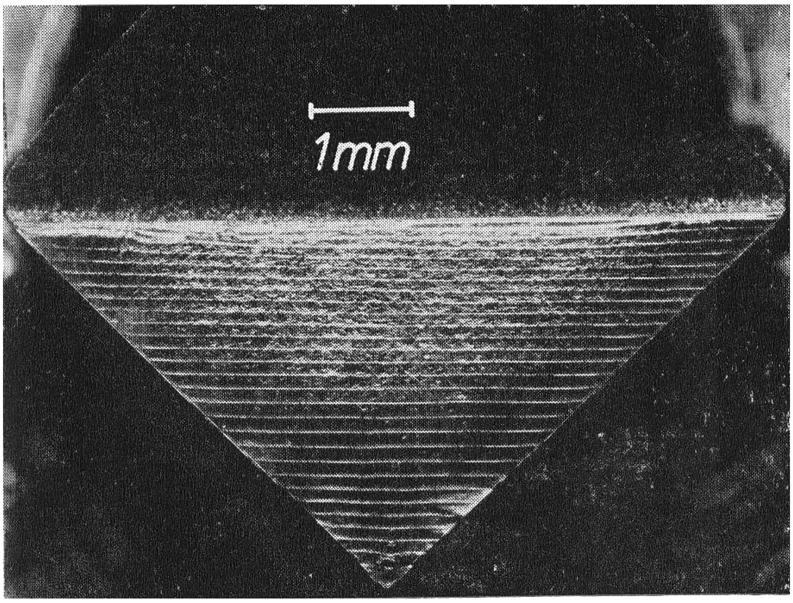

Figure 4.3: Optical micrograph of the fracture surface in the push-pull specimen from Figure 4.2 (Neumann, 1974).

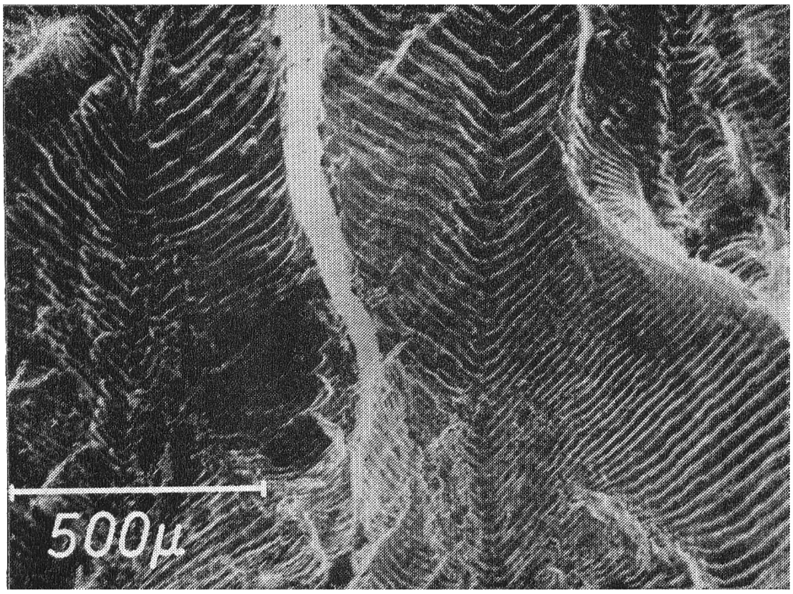

Figure 4.4: SEM micrographs of the fracture surface in the middle of the bending specimen with $[001]$ notch orientation from Figure 4.2 (Neumann, 1974).

as taking place via alternating shear on two slip planes intersecting the crack front (Neumann, 1974; Pelloux, 1970). Neumann made use of copper single crystals subjected to bending or tension-compression. In order to obtain a simple process of fatigue crack growth confined to a single macroscopic plane, specimens with the principal stress direction [100] were used. The bending specimens were notched, with the base of the notch in either the [001] or [011] direction (Figure 4.2). Notched [100] crystals were also used for tension-compression tests with the notch oriented in the [011] direction (Figure 4.2).

Under these conditions, Neumann did the following observations. The crack tip was a V-groove with a constant angle. The blunting process by plastic deformation took place through widening of the ”V” at the constant crack tip angle. The macroscopic plane of crack growth was (100) in the tension-compression test as well as in the bending tests for both notch orientations. In the middle of both bending specimens, the macroscopic crack front orientation coincided with the respective orientation of the notch. In the middle of the bending specimen with notch orientation [011] as well as in the push-pull specimen long and straight striations lying along the [011] direction were found (Figure 4.3). Thus, the microscopic and macroscopic crack front orientations were identical in these tests. In contrast, the fracture surface of the specimen with the notch direction [001] was covered with alternating narrow zones of striations oriented in [011] and [0$\bar{1}$1] directions (Figure 4.4). From these observations, he concluded that the fatigue propagation take place through alternating shear on two $\langle 111 \rangle$ slip planes whose intersection line builds the crack front.

4.3 Material modeling and finite element implementation

FE simulations of crack propagation via blunting and re-sharpening under cyclic loading have been described in Gu and Ritchie (1999) and Tvergaard and Hutchinson (2002) for isotropic materials. These simulations were carried out for moderately large deformations at the crack tip in order to avoid the severe distortions of the elements at the crack tip. No striations were obtained in their simulations. In order to simulate striation formation, much larger deformations at the crack tip need to be considered which is only possible by usage of a repeated remeshing technique.

In order to verify Laird’s plastic blunting mechanism for crack propagation via striation formation for ductile poly- and fcc single crystals, FE calculations were performed for a quadratic plate (Figure 4.5) with an initially sharp edge crack placed in the middle of the left side under plane strain conditions using the FE code ABAQUS. The plate was subjected to a fully reversed tension-to-pressure cyclic load ($R = -1$) perpendicular to the crack plane (Mode I), constantly distributed over the upper and bottom plate edges.

Due to the cyclic nature of the plastic deformations at the crack tip, a plasticity model with kinematic hardening is required. In the polycrystal case, incremental J_2 elasto-plasticity based on the Jaumann rate was used. With the Mises yield function

$$\phi = \sqrt{\frac{3}{2} \left(\boldsymbol{T'} - \boldsymbol{X}\right) \cdot \left(\boldsymbol{T'} - \boldsymbol{X}\right)} - \sigma_0 \tag{4.1}$$

the plastic strain rate is determined by the associative flow rule

$$\boldsymbol{D}_{\mathrm{p}} = \dot{\lambda} \frac{\partial \phi}{\partial \boldsymbol{T}} \quad . \tag{4.2}$$

The kinematic hardening is described by the Armstrong-Frederick rule

$$\overset{\circ}{\boldsymbol{X}} = C_{\mathrm{X}} \left(\frac{2}{3} X_{\mathrm{Sat}} \boldsymbol{D}_{\mathrm{p}} - \dot{\lambda} \boldsymbol{X} \right) \tag{4.3}$$

and the Jaumann rate of the Cauchy stress by the isotropic elastic relation

$$\overset{\circ}{\boldsymbol{T}} = 2\mu \left(\boldsymbol{D} - \boldsymbol{D}_{\mathrm{p}}\right) + \lambda \,\mathrm{tr}\left(\boldsymbol{D} - \boldsymbol{D}_{\mathrm{p}}\right) \boldsymbol{I} \tag{4.4}$$

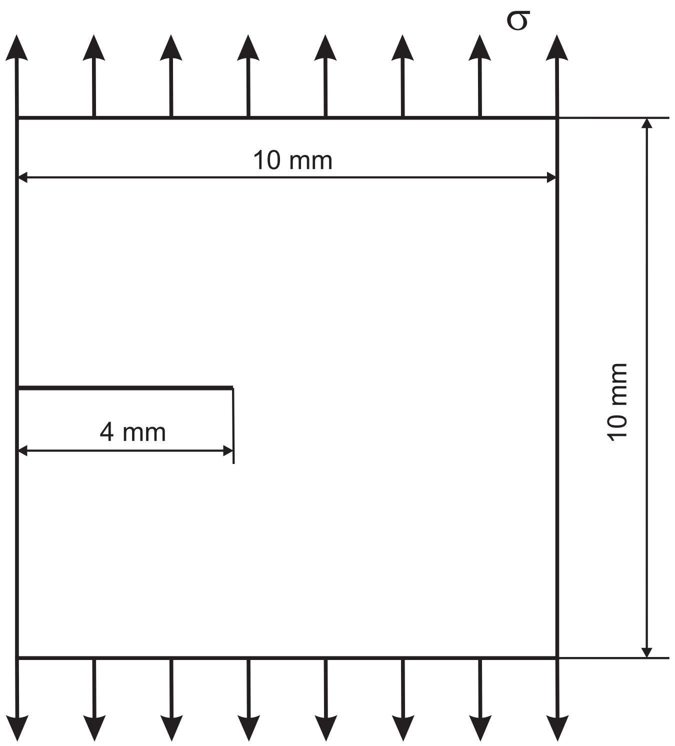

Figure 4.5: Geometry of the model used in the FE analysis.

Here, $\sigma_0 = 500$ MPa is initial yield stress, $X_{\mathrm{Sat}} = 150$ MPa the saturation value and $C_{\mathrm{X}} = 400$ the saturation rate parameter for the back stress as well as $\mu = 57692$ MPa and $\lambda = 86538$ MPa the Lame constants.

In the single crystal case, a geometrically nonlinear version of the crystallographic Cailletaud model (Meric *et al.*, 1991) based on the multiplicative elasto-plastic decomposition of the deformation gradient $\boldsymbol{F} = \boldsymbol{F}_{\mathrm{E}}\boldsymbol{F}_{\mathrm{P}}$ was implemented into the FE program ABAQUS via the user material interface UMAT. For simplicity, only octahedral slip systems were considered. Accordingly, the second Piola-Kirchhoff stress in the intermediate configuration is given as

$$\boldsymbol{S}_{\mathrm{E}} = \mathbb{C}\left[\boldsymbol{E}_{\mathrm{E}}\right] \tag{4.5}$$

with $\boldsymbol{E}_{\mathrm{E}} = \frac{1}{2}(\boldsymbol{U}_{\mathrm{E}}^2 - \boldsymbol{I})$ being the elastic Green tensor, $\boldsymbol{U}_{\mathrm{E}}$ the elastic right stretch obtained from the polar decomposition $\boldsymbol{F}_{\mathrm{E}} = \boldsymbol{R}_{\mathrm{E}}\,\boldsymbol{U}_{\mathrm{E}}$ of $\boldsymbol{F}_{\mathrm{E}}$. The plastic velocity ”gradient” is determined by the crystallographic relation

$$\boldsymbol{L}_{\mathrm{P}} = \dot{\boldsymbol{F}}_{\mathrm{P}}\boldsymbol{F}_{\mathrm{P}}^{-1} = \sum\nolimits_{\alpha} \dot{\gamma}_{\alpha}\boldsymbol{s}_{\alpha} \otimes \boldsymbol{n}_{\alpha} \tag{4.6}$$

with the glide-system slips described by Norton type flow rule

$$\dot{\gamma}_{\alpha} = \left\langle \frac{|\tau_{\alpha} - x_{\alpha}| - r_0}{k} \right\rangle^n \operatorname{sign}\left(\tau_{\alpha} - x_{\alpha}\right) \tag{4.7}$$

and the glide-system back stress by Armstrong-Frederick rule

$$\dot{x}_{\alpha} = c_{\mathrm{X}}\left\{x_{\mathrm{Sat}}\dot{\gamma}_{\alpha} - x_{\alpha}|\dot{\gamma}_{\alpha}|\right\} \quad . \tag{4.8}$$

Here, $\mathbb{C}$ is the cubic elasticity tetrad with $C_{1111} = 200000$ MPa, $C_{1122} = 150000$ MPa and $C_{1212} = 100000$ MPa, $\dot{\gamma}_{\alpha}$ the slip rate, $\boldsymbol{n}_{\alpha}$ the slip plane normal, $\boldsymbol{s}_{\alpha}$ the slip direction, τ_{α} the crystallographic projection of $\boldsymbol{S}_{\mathrm{E}}$ and x_α the back stress for the slip system α. $k = 10$ MPa and $n = 5$ are the viscosity parameters as well as $x_{\mathrm{Sat}} = 200$ MPa the saturation value and $c_{\mathrm{X}} = 100$ the saturation rate parameter for the back stress. Such a low value for the viscosity parameter k was chosen in order to produce quasi rate independent behavior.

During the FE simulations no initial radius for the crack tip was assumed. The actual shape of the crack tip followed from an initially sharp crack by repeated remeshing. The remeshing was performed manually with the help of the commercial program Patran. The region with the critically distorted elements was covered with a new mesh. The assessment of the degree of distortion was purely by eye whereby attention was paid that the distortion of the elements was moderate.

ABAQUS/Standard uses a Lagrangian-based finite-element formulation of the momentum balance. Here, the mesh is attached to and deforms with the material. When the strains become large, the elements may become overly distorted and lead to numerical problems. In this case, one remedy is to remesh the deformed structure, and in particular refine the mesh in those areas where mesh distortion is (too) extreme. To this end, data from the old mesh has to be mapped onto the new one. This is done by first extrapolating the integration point data to each node and averaging the result over all elements attached to a given node. Next, the new mesh and new integration points are generated, the location of the new integration points in the old mesh is determined (assuming that they all lie within the old mesh), and the data are projected from the old nodes onto the new integration points via interpolation. All required data can be interpolated in this way so that the algorithm can proceed using the new mesh.

Since all variables except the displacements are generally not continuous across element boundaries, this interpolation procedure can change the values of interpolated variables significantly. In the case of an overstress model such as the Cailletaud model, in which the crystallographic slip-rate is given by a polynomial (power law) in the difference between the resolved shear and internal stresses, even a moderate change in the overstress can lead to very large changes in the slip rate due to the power-law behavior. To avoid this, we proceed as follows. The resolved shear stress on a given glide plane represents as usual the projection of the second Piola-Kirchhoff stress onto the corresponding glide plane. In the metal plasticity/small elastic-strain context, this stress is a linear function of the elastic Green tensor (4.5). In particular, small elastic strains $\|\boldsymbol{E}_{\mathrm{E}}\| \ll 1$ implies $\boldsymbol{U}_{\mathrm{E}} \approx \boldsymbol{I}$ and $\boldsymbol{F}_{\mathrm{E}} \approx \boldsymbol{R}_{\mathrm{E}}$. In order to preserve this property, as well as the positive-definiteness of $\boldsymbol{U}_{\mathrm{E}}$ and the orthogonality of $\boldsymbol{R}_{\mathrm{E}}$, $\boldsymbol{U}_{\mathrm{E}}$ and $\boldsymbol{R}_{\mathrm{E}}$ are interpolated separately. In particular, the orthogonality of $\boldsymbol{R}_{\mathrm{E}}$ is preserved with the help of its Rodrigues form

$$\boldsymbol{R}_{\mathrm{E}} = \boldsymbol{I} + \sin\varphi_{\mathrm{E}}\,\mathrm{axt}(\boldsymbol{n}_{\mathrm{E}}) + (1-\cos\varphi_{\mathrm{E}})\,\mathrm{axt}(\boldsymbol{n}_{\mathrm{E}})^2 \tag{4.9}$$

in terms of the rotation angle φ_{E} about the rotation axis (unit vector) $\boldsymbol{n}_{\mathrm{E}}$. Here, $\mathrm{axt}(\boldsymbol{v})$ represents the (skew-symmetric) axial tensor of the vector $\boldsymbol{v}$, defined by $\mathrm{axt}(\boldsymbol{v})\boldsymbol{a} := \boldsymbol{v}\times\boldsymbol{a}$. Defining the axial vector of a rotation by $\mathrm{axv}(\boldsymbol{R})\times\boldsymbol{a} := \mathrm{skw}(\boldsymbol{R})\boldsymbol{a}$, we have

$$\varphi_{\mathrm{E}}(\boldsymbol{R}_{\mathrm{E}}) = \arccos\{(\mathrm{tr}(\boldsymbol{R}_{\mathrm{E}})-1)/2\} \tag{4.10}$$

and

$$\boldsymbol{n}_{\mathrm{E}}(\boldsymbol{R}_{\mathrm{E}}) = \frac{1}{\sin(\varphi_{\mathrm{E}}(\boldsymbol{R}_{\mathrm{E}}))}\,\mathrm{axv}(\mathrm{skw}(\boldsymbol{R}_{\mathrm{E}})) \quad . \tag{4.11}$$

On this basis, $\varphi_{\mathrm{E}}(\boldsymbol{R}_{\mathrm{E}})$ and $\boldsymbol{n}_{\mathrm{E}}(\boldsymbol{R}_{\mathrm{E}})$ are used as described above to transfer the values of $\boldsymbol{R}_{\mathrm{E}}$ from the old mesh onto the new mesh.

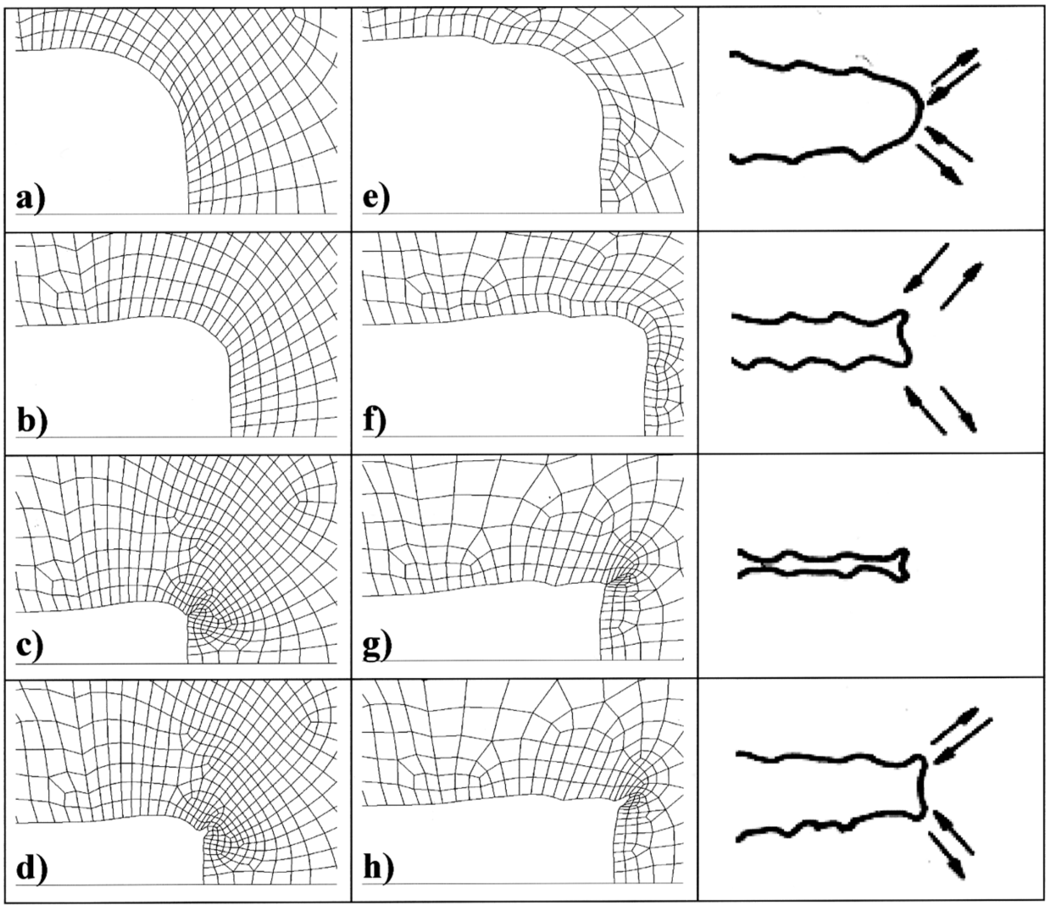

Figure 4.6: Polycrystal simulation results for crack propagation by blunting and re-sharpening. These are for (i), peak tensile loading (first row) followed by (ii), zero loading (second row), (iii), peak compressive loading (third row), and by (iv), zero loading (fourth row).

4.4 Simulation results

Turning now to the simulation results, we start with the polycrystal simulation. For this simulation the applied stress was varying linearly between the minimum and maximum values of ± 260 MPa and, accordingly, the maximum stress intensity factor was $K_{\max} = 29$ MPa$\sqrt{\mathrm{m}}$. Figure 4.6 shows the deformation evolution at the crack tip. Starting from an initially sharp crack, increasing the tensile load results in crack blunting to a semicircular form (a). Due to the changing nature of the deformation in the unloading stage, the crack tip then begins to buckle (b) and folds up in the compressive stage (c). In the simulation, mutual penetration of the material in the folded area at the crack tip is prevented by using a contact algorithm. As the compressive load is removed (d), the folded area at the crack tip opens up, creating an ”ear”. This also results in the crack lengthening. The subsequent load increase results in new blunting. In addition, a fatigue striation, created during the compression in the previous cycle, is now visible (e). The following stages (f), (g), (h) are a cyclically repetition of the re-sharpening process of the previous cycle, which leads to the creation of a new ”ear” and thus to another striation, as well as to a further increase in the crack length. The similarity to Laird’s idea (the last column in Figure 4.6) is remarkable.

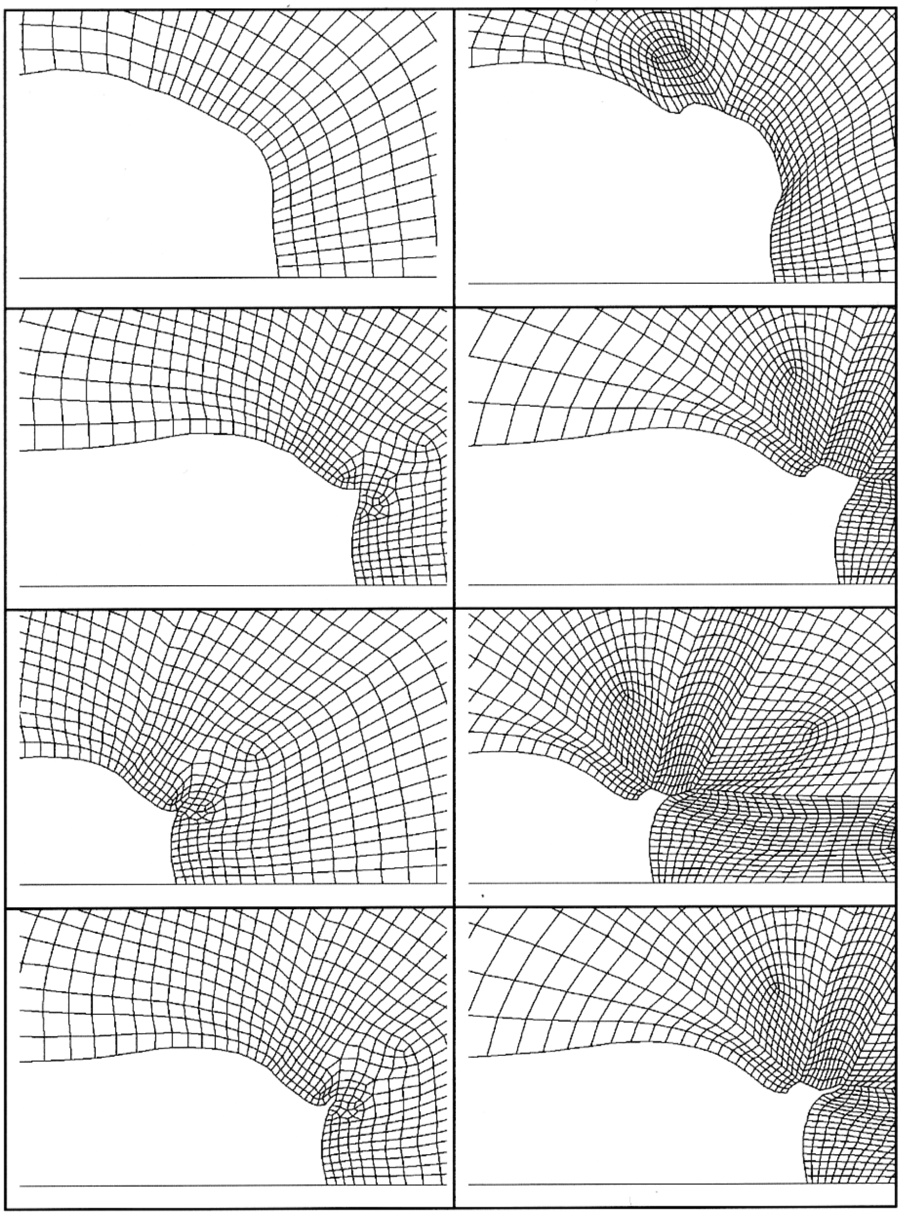

Figure 4.7: Single crystal simulation results for crack propagation by blunting and re-sharpening for crack plane orientation (001) and crack growth direction [110]. These are for (i), peak tensile loading (first row) followed by (ii), zero loading (second row), (iii), peak compressive loading (third row), and by (iv), zero loading (fourth row).

Due to rather complicated deformation state at the crack tip (buckling) the quantitative results might be sensitive to the quality of the mesh. However, due to the complexity of the remeshing procedure no mesh dependence study was carried out. This is also the reason why not more than two cycles were investigated. The authors were interested rather in obtaining a qualitative agreement between FE simulations and Laird's scheme. We expect that the qualitative deformation picture of the crack tip wouldn't change much if considering further cycles or using another mesh with comparable element size.

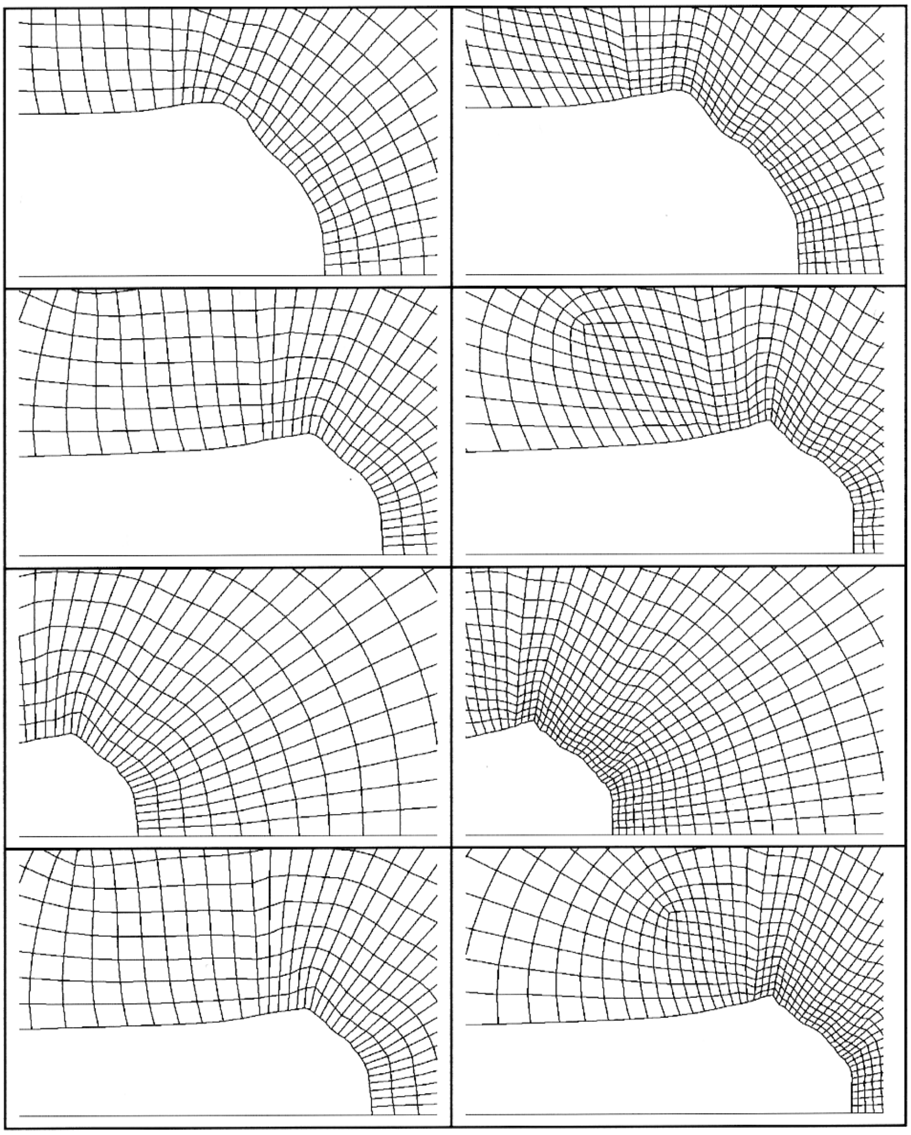

Figure 4.8: Single crystal simulation results for crack propagation by blunting and resharpening for the crack plane orientation (001) and crack growth direction [100]. The displayed sequence of results is the same as in Figure 4.7.

Now, we consider the single crystal simulation results. The crack propagation simulations were carried out for cracks with crack plane (001) for two different crack growth directions with respect to the crystal, *i.e.*, [110] and [100]. These are the same as those used by Neumann (1974) in his crack propagation experiments on single crystalline copper. The external cyclic load was imposed in (001) direction. For both directions the applied stress was varying linearly between the minimum and maximum values of ± 110 MPa and, accordingly, the maximum stress intensity factor was $K_{\max} = 12.3$ MPa$\sqrt{\mathrm{m}}$.

The deformation patterns at the crack tip with the orientation (001)[110] are very similar to those of the polycrystal simulation. Figure 4.7 shows the same qualitative behavior during a loading cycle: blunting in the tensile stage and folding into a double notch in the compressive stage attended by the creation of a fatigue striation and a crack extension.

The crack growth simulation for the crack orientation (001)[100] with the same stress level as for (001)[110] also yields crack extension via large deformation, however now without striation formation. The corresponding results are shown in Figure 4.8.

Comparison of the FE simulations and Neumann's experiments allows us to draw a number of interesting conclusions. For example, in the tests with the notch orientation [011], Neumann observed long straight striations lying parallel to the direction of the notch base. This means that the macroscopic and microscopic crack front orientations are identical, and that the crack growth direction in these tests was $[0\overline{1}1]$. This is the same crack growth direction for which we obtained striations in our FE simulations. As for the growth direction [100], comparison between the plane strain FE simulations and Neumann's bending tests with a macroscopic crack front orientation [100] are non-trivial. This is because the deformation process in the experiment is three-dimensional, such that is not possible to impose the orientation [100] on the microscopic crack front. As we have seen in the previous section, microscopically, the crack tends to propagate in [011] and $[0\overline{1}1]$ directions, and the crack surface is covered with alternating narrow zones of striations oriented in these directions. Also visible in Figure 4.4 are, however, bright areas without any striations. These are transitions zones where the crack front changes direction from [011] to $[0\overline{1}1]$. Accordingly, at some point in these striationless areas, the crack front becomes oriented in the [100] direction. This is in agreement with the FE simulations, which yielded no striations in this direction.

4.5 Conclusion

The purpose of this work was to investigate Laird's plastic blunting and re-sharpening mechanism for crack propagation via striation formation for ductile poly- and fcc single crystals. In Laird's theory, the fatigue crack extension results solely from the variable character of the deformation at the crack tip during loading and unloading. In particular, the crack tip blunts during the loading stage and folds into a double notch during the unloading stage, resulting in striation formation. In order to verify Laird's mechanism, FE calculations were performed for a rectangular plate with an initially sharp crack under plane strain conditions. The plate was subjected to a fully reversed tension-to-pressure cyclic load perpendicular to the crack plane (Mode 1). No initial radius for the crack tip was assumed. The actual shape of the crack tip followed from an initially sharp crack by repeated remeshing. To model the constitutive behavior typical for polycrystalline ductile metals, J_2 hypo-elasto-plasticity with Armstrong-Frederick kinematic hardening was used. To model the constitutive behavior typical for ductile fcc single crystals, a geometrically nonlinear version of Cailletaud's model based on the multiplicative elastic-plastic decomposition of the deformation gradient was implemented into the FE program ABAQUS. Only octahedral slip systems were considered. In the single crystal case crack propagation simulations were carried out for cracks with crack plane (001) for two different crack growth orientations [110] and [100]. The external cyclic load was imposed in the (001) direction. Using repeated remeshing for severely distorted elements at the advancing crack tip, deformation patterns in the sense of Laird's mechanism for fatigue crack propagation with striation formation were obtained for the polycrystal simulation as well as the single crystal simulation with [110] crack growth direction. The simulation for [100] crack growth direction with the same stress level as for [110] direction also yielded crack extension by the progressive large deformations, but without striation formation. The dependence of the fatigue striation formation on the crack growth direction as predicted by the simulation of crack propagation in single crystals is verified by the experimental results of Neumann (1974) on pure copper single crystals.

References

Bouchard, P. O., Bay, F., Chastel, Y. (2003). Numerical modelling of crack propagation: automatic remeshing and comparison of different criteria. Computer Methods in Applied Mechanics and Engineering 192, 3887–3908.

Gu, I., Ritchie, R.O. (1999). On the crack-tip blunting model for fatigue crack propagation in ductile materials. Fatigue and Fracture Mechanics, ASTM STP 1332, 552–564.

Honeycombe, R. W. K. (1968). The plastic deformation of metals. Edward Arnol (Publishers) Ltd., London.

Laird, C., Smith, G.C. (1962). Crack propagation in high stress fatigue. Philosophical Magazine 8, 847–57.

McClintock, F. A. (1967). Discussion to C. Laird's paper ”The influence of metallurgical microstructure on the mechanisms of fatigue crack propagation”. Fatigue Crack Propagation, ASTM STP 415, 170–174.

Meric, L., Poubanne, P., Cailletaud, G. (1991). Single crystal modeling for structural calculations: part 1 - model presentation. Journal of Engineering Materials and Technology 113, 162–170.

Neumann, P. (1974). New experiments concerning the slip process at propagating fatigue cracks. Acta Metallurgica 22, 1155–1165.

Nguyen, O., Repetto, E. A., Ortiz, M., Radovitzky, R. A. (2001). A cohesive model of fatigue crack growth. International Journal of Fracture 110, 351–369.

Pelloux, R.M.N. (1970). Crack extension by alternating shear, Engineering Fracture Mechanics 1, 697–704.

Ritchie, R.O. (1999). Mechanisms of fatigue-crack propagation in ductile and brittle solids. International Journal of Fracture 100, 55–83.

Suresh, S. (1998). Fatigue of materials. Cambridge University Press.

Tvergaard, V., Hutchinson, W. (2002). Crack growth per cycle by blunting and void growth. In: A. F. Blom (ed.), Fatigue'2002, Proceedings of Eighth International Fatigue Congress, Stockholm, Sweden, Vol. 1, EMAS, U.K., 107–116.

Tvergaard, V. (2004). On fatigue crack growth in ductile materials by crack-tip blunting. Journal of Mechanics and Physics of Solids 52, 2149–2166.

Wu, J., Ellyin, F. (1996). A study of fatigue crack closure by elastic-plastic finite element analysis for constant-amplitude loading. International Journal of Fracture 82, 43–65.

Curriculum Vitae

Surname	Levkovitch
Forename	Vladislav
Nationality	German
Date of Birth	05.07.1974, Dushanbe

1981-1991	Middle School, Dushanbe
1991	Emigration to Germany
1991-1992	German Course, Berlin
1992-1993	Preparatory College at the Technical University of Berlin
1994-2000	Physical Engineering, Technical University of Berlin
2000-2003	Research Associate, Federal Institute for Materials Research and Testing, Berlin, Division V.2, Mechanical Behaviour of Materials
since 2003	Research Associate, University of Dortmund, Department of Mechanical Engineering, Chair of Mechanics